

Optical Characterization of Organic Semiconducting Single Crystals

by

Jennifer Weinberg-Wolf

A dissertation submitted to the faculty of the University of North Carolina at Chapel Hill in partial fulfillment of the requirements for the degree of Doctor of Philosophy in the Department of Physics & Astronomy.

Chapel Hill

2006

Approved by:

Dr. Laurie McNeil, Advisor
Dr. John Hernandez, Reader
Dr. John Papanikolas, Reader
Dr. Richard Superfine, Reader
Dr. Otto Zhou, Reader

©2006
Jennifer Weinberg-Wolf
ALL RIGHTS RESERVED

ABSTRACT

JENNIFER WEINBERG-WOLF: Optical Characterization of Organic
Semiconducting Single Crystals
(Under the Direction of Dr. Laurie McNeil)

Over the last decade interest in the possibility of “plastic electronics,” semiconducting organic materials that hold the potential for display devices with improved characteristics, has increased. To date, the majority of research has focused on material development and device design. However, if scientists are able to understand the connection between the structural and electronic properties of molecules, they can tailor new compounds with desired physical characteristics. Optical characterization is the first step to understanding the structural properties of materials.

This work focuses on characterizing single crystals of two specific molecules: α -hexathiophene and 5,6,11,12-tetraphenyl tetracene (rubrene). While there is plenty of information currently available in the literature about α -hexathiophene, the resonant Raman experiments I describe in Chapter 3 have uncovered the lowest experimentally-recorded excited electronic levels. I have tentatively identified these states as either a triplet Frenkel exciton or a bound singlet Frenkel exciton.

Chapter 4 details how I used Raman, infrared and photoluminescence spectroscopy, as well as computer simulations, to characterize rubrene. Studies of tetracene single crystals helped guide the understanding of the structural and electronic properties of rubrene. Although all molecular crystals have low intermolecular coupling, my analysis showed that rubrene has particularly low coupling, even for a molecular crystal. This result goes against commonly held belief that the best molecules for “plastic electronic” devices should have strong π -electron overlap. The temperature dependent photoluminescence spectrum

clearly reveals emission from free carriers as well as free charge transfer excitons, free Frenkel excitons and deep impurity and defect levels.

ACKNOWLEDGMENTS

There are many people who helped make this document and the research behind it possible. First, I have to thank my advisor, Laurie McNeil, without whose guidance, support, and equipment this project would not have been possible. She has been a wonderful mentor, knowing when to give much needed direction and when to let me work out problems on my own. I would also like to thank the other members of my committee, John Hernandez, John Papanikolas, Richard Superfine, Ed Samulski and Otto Zhou for their time, attention, and helpful suggestions and comments throughout this entire project.

Incredibly important collaborators who I must mention, praise and thank are Christian Kloc at Lucent Technologies, who supplied all of my materials; and Shubin Liu of the High Performance Computing Group at UNC, who ran the different theoretical calculations. Although not directly working on the same scientific questions, my class-mates and lab-mates over the last seven years have been a crucial component of my success. They served as sounding boards for discussion, extra sets of hands for countless alignment procedures, great sources of information, good company and all around good friends. Thank you to Jim Crooks, Kris Capella, Jessica Owens, Chris Lawyer, Russell Walker, Kris McGuire, Zhongqiao Ren and especially Eric Harley.

There is no question in my mind that I would not have achieved what I have today without the support of many individuals: friends, teachers and family throughout my life. I am fortunate enough to have too many people to thank individually, but special recognition must be given to some outstanding individuals. My college blockmates who never seem to get tired of listening to me vent,

my in-laws who always ask what I am currently working on, fantastic physics teachers who inspired me to continue studying a subject I have learned to love and my sisters for bragging about their big sister, the physicist. My parents, Margot and Alan, always encouraged me to take the hardest science classes I could and not be discouraged by obstacles. They taught me it was ok to be different, to love to learn and to be excited rather than intimidated when I was the only girl in the classroom. I would not have accomplished this work without their support.

Last, but definitely not least, I must thank my wonderful husband, Jonathan Miller, who put up with me for so many years through the entire graduate school process. Without him I would have spent many lonely, hungry nights in lab. Instead he would keep me company through seemingly endless numbers of scans and bring picnic meals to lab when I couldn't leave. He also served as my personal system administrator, making sure my computers worked, debugging my code and helping me to implement (sometimes just actually writing) data analysis and molecular visualization scripts. But most important was his unwavering support and love for which I cannot thank him enough.

Jennifer Weinberg-Wolf

April 6, 2006

CONTENTS

	Page
LIST OF TABLES	x
LIST OF FIGURES	xi
Chapter	
I. Introduction	1
1.1 Overview	1
1.2 Molecular Crystals	3
1.2.1 Oligothiophenes: Alpha-hexathiophene	4
1.2.2 Oligoacenes: Tetracene and Rubrene	7
II. Experimental Techniques	12
2.1 Crystal Growth	12
2.2 Raman Spectroscopy	13
2.2.1 Classical Theory	14
2.2.2 Quantum Theory	16
2.2.3 Temperature Effects	19
2.2.4 Resonant Raman Effect	20
2.2.5 Experimental Setup	21
2.3 Infrared Spectroscopy	23
2.4 Photoluminescence Spectroscopy	24
2.4.1 Photoluminescence Theory	25
2.4.2 Temperature Effects	30
2.4.3 Experimental Setup	30
2.5 Computer Calculations	31

III.	Raman Spectroscopy of Alpha-Hexathiophene	33
3.1	Alpha-Hexathiophene Crystals	33
3.2	Room Temperature Experiments	37
3.3	Temperature Dependent Raman	42
3.4	Resonant Raman Spectroscopy	44
3.4.1	Results	47
3.4.2	Frenkel Excitons	49
3.4.3	Temperature Dependence of Resonances	51
3.5	Conclusion	54
IV.	Optical Characterization of Rubrene and Tetracene	55
4.1	Raman Measurements	55
4.1.1	Rubrene and Tetracene Crystals	55
4.1.2	Experimental Conditions	58
4.1.3	Computer Simulations	60
4.1.4	Rubrene Single Crystal Raman Results	60
4.1.5	Comparison to Theory	62
4.1.6	Tetracene Single Crystal Spectrum	68
4.1.7	Comparison of Rubrene and Tetracene Spectra	72
4.1.8	Temperature Dependence of Rubrene Spectra	75
4.1.9	Intermolecular Coupling in Rubrene Single Crystals	76
4.2	Infrared Spectrum of Rubrene	80
4.3	Photoluminescence of Rubrene	86
4.3.1	Crystals and Experimental Setup	86
4.3.2	Low Temperature Photoluminescence Results	86
4.3.3	Comparison to Theory	89
4.3.4	Temperature Dependence of Rubrene PL Spectra	91
4.3.5	Rubrene PL Dependence on Photoexcitation Energy	95
4.4	Conclusion	98
V.	Conclusions	100

VI.	REFERENCES	103
-----	----------------------	-----

LIST OF TABLES

3.1	Comparison of Experimental and Theoretical Structure of α -hexathiophene	34
3.2	Experimentally-Measured and Theoretically-Predicted Intramolecular Raman Modes for α -hexathiophene	39
3.3	Highlights From Table 3.2	43
3.4	Additional Intramolecular Raman Modes	47
3.5	Intermolecular Resonant Raman Modes of α -hexathiophene	47
4.1	Atomic Positions in Rubrene and Tetracene	57
4.2	Allowed Raman Modes for Backscattering Geometry	62
4.3	Irreducible Representation for the Isolated Rubrene Molecule	66
4.4	Character Table for the C_{2h} Point Group	66
4.5	Peak Positions for Measured and Calculated Raman Spectra of Rubrene	67
4.6	Frequency of Experimental and Theoretical Intramolecular Modes for Tetracene	72
4.7	Temperature Dependence of Rubrene Intramolecular Modes	75
4.8	Densities and Mobilities of Oligoacenes	79
4.9	Predicted and Measured Infrared Peak Positions and Intensities	81
4.10	Peak Positions from Low Temperature PL Measurements of Rubrene	89
4.11	PL Peak Energy vs. Temperature for Rubrene Single Crystals	93

LIST OF FIGURES

1.1	Oligothiophene Molecules	4
1.2	Oligoacene Molecules	7
1.3	Diagram of a Rubrene Molecule	9
2.1	Light Scattering Schematic	13
2.2	Feynman Diagrams for Stokes Scattering	16
2.3	Raman Spectrometer Schematic	21
2.4	Photoluminescence Schematic	25
2.5	Photoluminescence Spectrometer Schematic	32
3.1	Alpha-hexathiophene ($C_{20}H_{14}S_6$) Molecule	34
3.2	Molecular Stacking in α -hexathiophene Unit Cell	35
3.3	Room Temperature Raman Spectrum of α -hexathiophene	38
3.4	Changes in the α -hexathiophene Spectra with Temperature	44
3.5	Temperature Dependence of Raman Modes of α -hexathiophene	45
3.6	On and Off Resonance Raman Spectra of α -hexathiophene	46
3.7	Resonance Profiles for α -hexathiophene	48
3.8	Temperature Dependence of the Resonance Profile of α -hexathiophene	52
4.1	Rubrene ($C_{42}H_{28}$) Molecule.	56
4.2	Three Views of the Packing in the Rubrene Single Crystals	58
4.3	Tetracene ($C_{18}H_{12}$) Molecule	59
4.4	Room Temperature Raman Spectrum of Rubrene Single Crystals	63
4.5	Experimental vs. Theoretical Peak Positions for Rubrene Single Crystals	64
4.6	Experimental vs. Theoretical Peak Positions for Tetracene Single Crystals	69
4.7	Room Temperature Raman Spectrum of Tetracene Single Crystals	70
4.8	Room Temperature Low-Energy Experimental Data and Theoretical Predictions for Rubrene and Tetracene Single Crystals	74

4.9	Temperature Dependence of Low-frequency Raman Modes of Rubrene Single Crystals	76
4.10	Infrared Theoretical and Experimental Spectrum for Rubrene Single Crystals	82
4.11	Experimental vs. Theoretical Peak Positions for Infrared Spectrum of Rubrene Single Crystals	83
4.12	One Low Temperature Photoluminescence Spectrum of Rubrene Single Crystals	87
4.13	Low Temperature Photoluminescence Spectra of Rubrene Single Crystals from Multiple Crystallites	88
4.14	Example Fit of PL Spectrum of Rubrene at 18 K	90
4.15	Temperature Dependence of Rubrene PL Spectra	92
4.16	PL Spectra of Rubrene Single Crystals with 496.5 nm Excitation Source	96
4.17	PL Spectra of Rubrene Single Crystals with Multiple Incident Excitation Sources	97

Chapter 1

Introduction

1.1 Overview

Within the last 50 years, interest has grown in the optical properties of organic molecular crystals. Many books and reviews of interesting optically-active materials are available in the literature [1,2]. When researchers first successfully fabricated an all-organic light-emitting device (OLED) using tris-8-hydroxyquinoline aluminum (Alq_3) in 1987 [3], interest in the applications of thin films of these optically-active organic molecular materials grew. Thus began the development of a new commercial product: all-organic displays based on OLEDs and organic field-effect transistors (OFETs). Horowitz recently published a good review of the work on thin film technology using organic materials [4]. The first single-crystal OFET [5] (which used alpha-hexathiophene) followed soon after the thin-film device work. Compared to liquid crystal display (LCD) technology, organic transistors and discrete LED displays hold the potential for devices with improved characteristics including lower power requirements, better resolution, more mechanical flexibility, and lower production costs (to name just a few benefits).

Research to date has focused on two distinct initiatives: semiconducting polymers and organic small molecules. The former may have the advantage of higher

stability for practical applications, but the latter, due to the feasibility of forming large single crystals, seem to be more suitable for basic science studies. Materials composed of polycyclic aromatic compounds such as the π -conjugated oligothiophenes, oligoacenes, and their derivatives are of particular interest. These small molecules with high levels of conjugation are particularly appealing for display applications, as the highest occupied/lowest unoccupied molecular orbital (HOMO/LUMO) separation is typically in the visible range. In the crystal state, these materials still have optical transitions in the visual range, which is crucial for optical device applications. Chemists can tailor these molecules for specific applications by modifying the molecular structure through chemical substitution and/or the addition of side groups. Consequently, scientists and optical engineers can incorporate the molecules into a host of photonic devices. Some of these molecules are also very stable, another requirement for a successful device. Many different molecules have been studied and numerous devices fabricated [6–9] from these molecular crystals, including FETs [5, 10–22], LEDs [3, 23–27], photovoltaic cells [28–31], a chemical UV actinometer [32], waveguides [33], optical links [34], chemical sensors [35, 36], and organic lasers [26, 37]. It is important to have an understanding of the relationships among crystal structure, optical properties, and transport properties of a material to advance design possibilities. The hope is that, once this connection is well understood, it will be possible to tailor molecules for desired performance in devices.

A perusal of the literature quickly tells the reader that many of the important characteristics of these materials for device manufacturing depend on the microstructure of the thin films and single crystals used. High-quality single crystals that are relatively free of defects and impurities allow studies of the various intrinsic qualities of the materials. Of the different intrinsic properties, optical behavior is particularly interesting because of the materials’ potential use in devices such as LEDs and displays. Information about electron-phonon coupling in resonant states, also derived through optical studies, could have an

impact on design aspects that would affect electrical performance of transistors and other devices. This dissertation focuses on the optical characterization of three different polycyclic aromatic π -conjugated molecules and single crystals: alpha-hexathiophene, 5,6,11,12-tetraphenyl tetracene (rubrene), and tetracene. This analysis was primarily performed with Raman Spectroscopy and photoluminescence spectroscopy, as well as with computer calculations from GAUSSIAN 03 [38].

1.2 Molecular Crystals

Two force regimes: strong covalent bonds within molecules and weak van der Waals forces between molecules distinguish molecular crystals. Because of the weak crystal field forces, such materials maintain many of the same characteristics as in the individual molecular components in the solid state, hence the designation as molecular crystals. The weak van der Waals bonds between molecules means that in the solid state, molecular crystal systems have very low lattice energy. As expected, this low lattice energy causes molecular crystals generally to have low melting and sublimation temperatures, low mechanical strength, and high compressibility. The packing of somewhat large molecules into the solid state leads to molecular crystals that tend to have low symmetry; therefore, anisotropy is not uncommon in many different crystal properties (e.g. optical, electronic, magnetic, and mechanical). Also, since the forces between molecules are very weak, it is possible to have several different lattice arrangements that all have similar ground state energies; thus polymorphism is very common.

Although the vibrational and electronic structures of the individual molecules are similar in the crystal state of molecular crystals, crystal field effects do exist. Most notable is the Davydov splitting of bands in both the electronic and vibrational spectra. The presence of more than one molecule in the unit cell

causes Davydov, or factor group, splitting. The multiple molecules in the unit cell will interact, thereby lifting degeneracies in energy of the original molecular spectrum.

1.2.1 Oligothiophenes: Alpha-hexathiophene

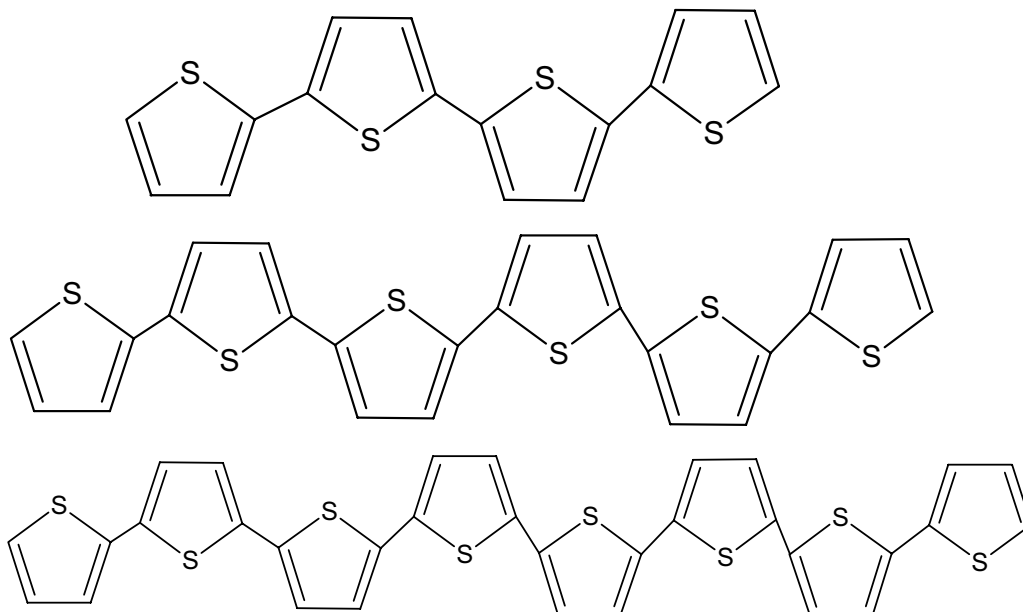


Figure 1.1: A series of α -oligothiophenes or linked thiol rings molecules. In order of increasing number of rings: α -tetrathiophene, α -hexathiophene, and α -octathiophene

Oligothiophenes are compounds comprising five-membered aromatic rings with four carbon atoms and one sulfur atom. In the α -oligothiophenes, the thiol rings bond to one another at an α -carbon (the carbon that bonds directly to the sulfur atom). The majority of research to date has focused on α -hexathiophene, as it has some of the most promising properties for devices. However, scientists have studied the other α -oligothiophenes extensively as well.

Researchers have predicted the theoretical geometric structures and electronic transitions [39] along with the lowest triplet state [40] for oligothiophenes with n , the number of rings, equal to $2 \cdots 8$. Further, they have calculated the ground

state conformation and potential energy curves when $n = 2$ and 3 [41]. Scientists have experimentally measured the thiophenes with $n = 3 \cdots 8$ and found the field-effect mobility to increase up to $n = 6$ (or α -hexathiophene) [42].

The mobility of α -hexathiophene is in the range $0.1\text{-}1\text{ cm}^2/\text{V-s}$ [43,44], which is high for an organic material and is comparable to the value for amorphous hydrogenated silicon ($1\text{ cm}^2/\text{V-s}$). Luminescence and optical absorption studies [45] have found an indirect band gap of approximately 2.2 eV and a polaron binding energy of 0.35 eV . The crystal displays a strong luminescence when optically excited above the band gap, although the spectrum depends largely on the quality of the samples studied. As is typical for molecular crystals, the primary photoexcitations are Frenkel excitons, the lowest singlet to date has energy 2.3 eV [46]. Researchers have observed electroluminescence [47,48] in the range $525\text{ - }625\text{ nm}$ ($2.36\text{ - }1.98\text{ eV}$) and stimulated emission [49–51] in the range $590\text{ - }650\text{ nm}$ ($2.10\text{ - }1.91\text{ eV}$) and at a variety of temperatures [52]. Subsequently, they have produced a variety of devices from amorphous and polycrystalline thin films. Studies of four-, five- and six-ring systems [53] have produced time-resolved absorbance measurements. The energies of the photoexcitations in the different oligomers are approximately inversely proportional to the number of rings in the molecule.

As in all molecular crystals, the intramolecular covalent bonds are much stronger than the intermolecular van der Waals bonds and the crystals retain many of the characteristics of the molecules composing them. However, the way in which the molecules crystalize has a strong influence on the mobility of charge carriers, since the carriers must move among the molecules [54]. Other organic crystals display similar effects which frequently occur in multiple polytypes differing only in the stacking of the molecules within the unit cell. A complete understanding of the influence of the structure on the lattice dynamics of the material of interest is therefore important to the development of devices. Research groups have used Raman spectroscopy, infrared absorption spectroscopy and inelastic

neutron scattering to measure the phonon modes of α -hexathiophene [55–60] and substituted hexathiophene [61–71]. While clearly many optical and electronic studies exist, there has not been a complete study of resonant Raman possibilities in α -hexathiophene. This study would find possible electron-phonon coupling in the crystal as described in Chapter 3 and now available in the literature [72].

Schön Scandal

A discussion about a possible problem with some results in the literature on this particular molecule is advisable. Jan Hendrik Schön, formerly of Lucent Technologies, was one of the initial researchers to focus attention on α -hexathiophene, although others had already measured some very promising properties of the molecule. He was a very prolific scientist and reported great experimental success, making the first single molecule transistor, finding superconductivity in pentacene, and so on. However, after other groups were unable to reproduce his results, Lucent Technologies convened a special panel to investigate many of the publications more carefully. Unfortunately, this panel found multiple papers to have identical graphs purporting to be the outcomes of different experiments, unreasonable experimental accuracy, and results that contradict known physics outright [73]. This scientific misconduct resulted in the withdrawal of over 15 papers from prestigious journals by the co-authors including our collaborator Christian Kloc. The impact of this misconduct, however, is even greater if one stops to consider the number of citations of these fraudulent papers. Therefore, one must be very careful in reading the literature about this material (as well as the literature on pentacene). However, this scandal does not negate the previously-noted interesting qualities of α -hexathiophene and most of the published work on this molecule and crystal system can be trusted as quality science.

1.2.2 Oligoacenes: Tetracene and Rubrene

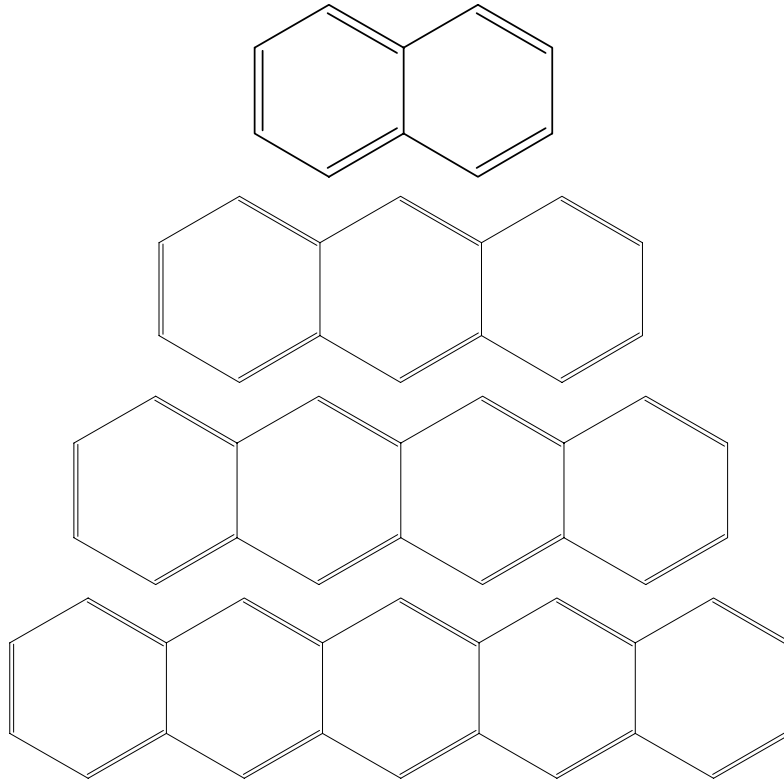


Figure 1.2: A series of oligoacenes or fused benzene ring molecules. In order of increasing number of rings: Naphthalene, Anthracene, Tetracene (also known as Naphthacene) and Pentacene

Oligoacenes are ladder-like hydrocarbon molecules that share many of the useful characteristics of the oligothiophenes. Researchers have focused on the three-ring (anthracene), four-ring (tetracene - also called naphthacene) and five-ring (pentacene) compounds depicted in Figure 1.2. All of the molecules have D_{2h} point group symmetry. The sp^2 hybridization of the valence carbon atoms causes the planarity of the molecules. Because of the difficulty of growing high-quality single crystals and the confusing existence of multiple polymorphs, systematic studies of the optical and vibrational properties have only recently been possible. The presence of defects and grain boundaries strongly influence the measured optical and transport properties of polycrystalline films of these materials,

pentacene’s properties are particularly sensitive to crystal quality [74].

One of the smaller molecules, anthracene, is a chain of three fused benzene rings. The Raman signature of anthracene single crystals [75–77], thin films [78], powder [79], and solutions [80]; at multiple temperatures [81, 82] and various pressures [83, 84]; and by theoretical calculations [85, 86] give a very complete picture of the vibrational structure of the molecule. Using Brillouin scattering [87] and inelastic neutron scattering (INS) [88], researchers have been able to measure the elastic constants of the single crystal. Photoconduction experiments on anthracene [89–91] yield values for the band gap between 3 and 4 eV. Scientists have also conducted experiments to measure the luminescence of single crystals [91, 92] at multiple temperatures [93] and at different pressures [94]. The spectra indicate a very strong coupling of excitons to intramolecular vibrations. Data from reflectivity studies of sublimed films [95] indicate that the \vec{a} and \vec{b} axes of the crystallites tend to lie in the plane of the substrate, a structural geometry similar to that found in other oligoacene thin films and crystallites. The full crystallographic information for the crystal at multiple temperatures (from X-ray diffraction studies [96]) is also available.

Tetracene has a measured band gap of 3-3.5 eV [97, 98]. As with anthracene, researchers have measured the photoluminescence spectrum at a variety of temperatures. The spectrum reveals a variety of free and trapped excitons, the energies of which depend on the structural characteristics and possible defects of the crystal [99]. The crystal field effects (Davidov splitting) are very similar for anthracene and tetracene [100]. Researchers have measured the exciton-phonon coupling constant g to be 0.77 [101, 102], where $g = \frac{E_{LR}}{B}$ and E_{LR} is the lattice relaxation energy while B is the exciton band halfwidth. For $g < 1$, excitons are not self-trapped. Tetracene has a very high hole mobility; values between 0.8 cm²/V-s [97] and 1.3 cm²/V-s [103] in high quality crystals approach and even exceed the mobility of amorphous silicon. The vibrational modes for the gas phase of both tetracene and pentacene molecules from experiments [104]

and theoretical calculations [105] are available in the literature. Early Raman measurements of tetracene crystals [106–109] have been of lower quality crystals or on older instruments incapable of high resolution, high signal-to-noise measurements. A more recent comprehensive study that collected data about the vibrational structure as a function of temperature and pressure for two polymorphs of the crystal [110] has improved the general structural understanding of this molecule.

Pentacene has a measured band gap of approximately 1.8 eV [111,112]. Crystallographic data are available for some of its polymorphs [113]. Researchers have measured the single crystal mobility of pentacene to be $1.4 \text{ cm}^2/\text{V-s}$ [103] while scientists predict a value as high as $75 \text{ cm}^2/\text{V-s}$ for very pure single crystals [114]. As with tetracene, however, the transport properties vary greatly depending on materials preparation and the structural defects in the resulting crystals and thin films [115,116]. Measurements exist for reflection spectra [117], photoluminescence spectra [118] and Raman spectra [106,119,120].

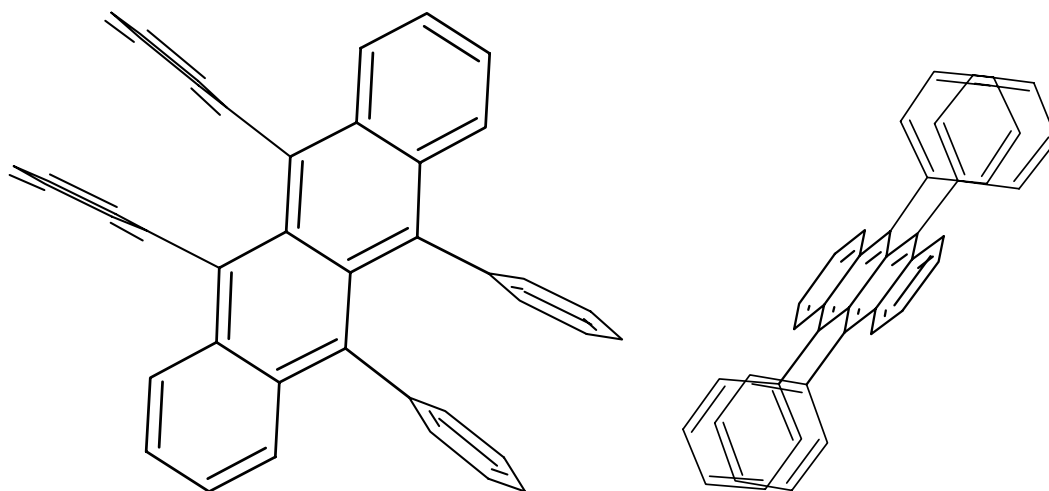


Figure 1.3: Diagram of a Rubrene Molecule

Slightly more complicated is the substituted oligoacene 5,6,11,12 - tetraphenyl tetracene, commonly known as rubrene. Rubrene is a relatively small aromatic hydrocarbon consisting of a backbone of four fused benzene rings (tetracene)

with four substituted phenyl groups (two on each internal ring) as shown in Figure 1.3. Steric hindrance dictates that the substituted phenyl groups rotate out of the plane of the tetracene backbone. The measured HOMO/LUMO gap of the molecule is approximately 2.2 eV [121, 122]. The main polymorph is an orthorhombic crystal [123–125] with D_{2h}^{18} point group symmetry (while the molecule has C_{2h} point group symmetry), and has four molecules in the unit cell. There are 102 Raman-active vibrational modes for the crystal. The crystal also has a high melting point ($>315^\circ\text{C}$).

Rubrene has an almost 100% photoluminescent efficiency at room temperature [126]. Scientists have successfully doped it into many other OLED devices to improve characteristics such as lifetime [127], stability [128], color [129] and brightness [130]. Other devices including chemical sensors [131], actinometers [32], and lightsticks make use of its properties. The consensus from the literature is that the crystals have a room-temperature band gap of approximately 2.21 eV [132]. Many research facilities have reproduced measurements of its hole mobility. Researchers have measured extremely high FET mobility [133, 134] sometimes as high as $20\text{ cm}^2/\text{V}\cdot\text{s}$ at room temperature, even higher than that of amorphous hydrogenated silicon. Also, time-of-flight measurements of the hole mobility in rubrene [135] indicate values as high as $2\text{ cm}^2/\text{V}\cdot\text{s}$. Some of these measurements may be complicated by the fact that rubrene readily forms a peroxide which alters the surface [136, 137]. Scientists know much less so far about the electronic and vibrational structure of the crystal. Studies of (relatively defect free) single crystals allow one to learn about the intrinsic characteristics of the material and shed light on the exceptionally high mobility of rubrene in comparison to other oligoacenes.

Physicists have measured the absorption spectrum in the visible range for evaporated thin films of rubrene [121, 138–140], as well as the photoluminescence spectrum [126, 141]. A recent publication began the difficult task of understanding the photoexcitations that occur in the single crystal [142] and will be dis-

cussed in more detail in Section 4.3. The literature contains a few Raman spectra for unpurified thin films [106, 143–145], but these are of low quality and often only demonstrate new possibilities in experimental techniques (i.e., FT-Raman) rather than focus on the interpretation of the actual vibrational structure of rubrene.

There is no comprehensive example in the literature of the vibrational structure of rubrene or tetracene from a technique such as Raman or infrared spectroscopy. Nor have scientists yet studied the vibrational modes at different temperatures or pressures either. This dissertation addresses these seeming holes in the available literature on these interesting materials.

Chapter 2

Experimental Techniques

The data I collected in this dissertation are all from optical techniques which investigate the electronic and vibrational structure of small samples. Shubin Liu of the High Performance Computing group of UNC performed computer calculations that aided, and at times guided the interpretation of the experimental results.

2.1 Crystal Growth

Christian Kloc at Bell Laboratories, Lucent Technologies, grew the single crystals used in these measurements using horizontal physical vapor transport in a flow of argon gas. He acquired the starting materials for α -hexathiophene and rubrene crystals from Aldrich. Widely available sources in the literature describe the details of the growth process for α -hexathiophene [146], similar materials [147] and for rubrene [148]. To change the morphology of the growing crystals and to get thick bulk crystallites more suitable for this present study, He subsequently used some previously sublimed rubrene crystals for a typical vacuum-sealed ampoule growth.

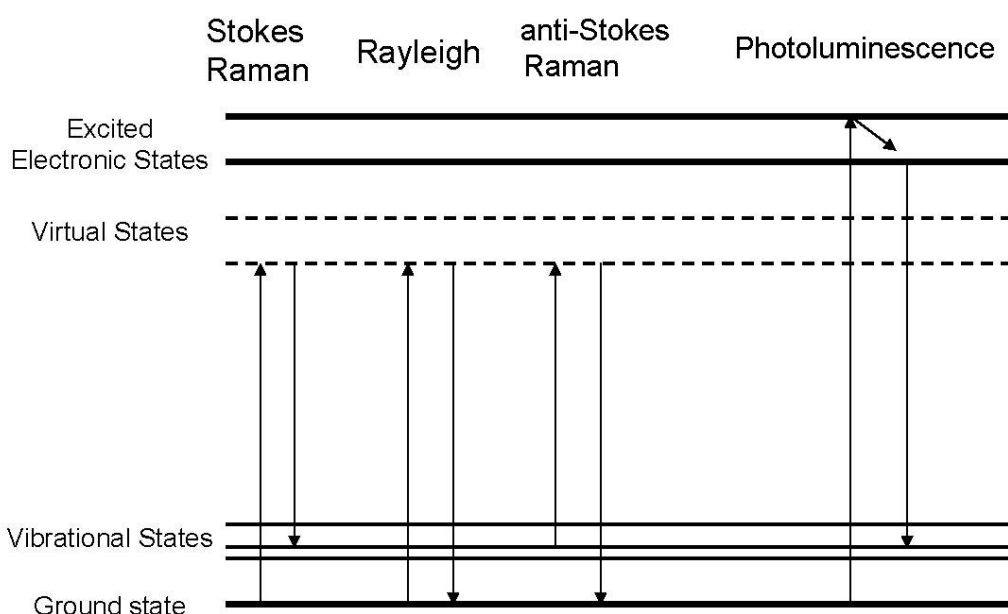


Figure 2.1: Possible interactions between an incident photon and a crystalline medium. Rayleigh scattering is an elastic process, while the Stokes and anti-Stokes interactions pictured are the inelastic Raman scattering processes.

2.2 Raman Spectroscopy

Raman spectroscopy is the inelastic scattering of light. It is a non-destructive, non-invasive probe of the vibrational structure and phonon modes of a crystal. Venkata Raman received the 1930 Nobel Prize in physics for measuring and understanding this inelastic scattering effect. The basic experiment requires a monochromatic incident light source (often a laser), a system of lenses to collect the scattered light, a system to separate the energies of the collected light (a spectrometer or spectrograph) and some sort of detector (initially photographic paper, now photomultiplier tubes (PMTs) and charge coupled devices (CCDs)).

Consider the example of a material irradiated by a high-intensity monochromatic light source. The molecules in the material will scatter this light, which one can collect for analysis. The majority of the scattering will be elastic, meaning that the scattered wavelength is equal to the incident wavelength. This phe-

nomenon is called Rayleigh scattering and is the second process from the left in the schematic of Figure 2.1. A very small proportion of the incident photons, (one in 10^6) however, will undergo Raman scattering in which the final state of the system is different from the initial state. In this case the outgoing, scattered photon has more (anti-Stokes scattering) or less (Stokes scattering) energy than the incident photon. The exact energy shift will depend on the type and strength of the bonds in the material which create phonons, so one can view the spectrum of a particular material as the vibrational fingerprint for the system.

2.2.1 Classical Theory

Although Raman scattering is a quantum-mechanical interaction, one can initially describe it classically. The incident monochromatic light source is a sinusoidal electro-magnetic planewave:

$$\vec{E}(\vec{r}, t) = \vec{E}_i(\vec{k}_i, \omega_i) \cos(\vec{k}_i \cdot \vec{r} - \omega_i t) \quad (2.1)$$

where ω is the frequency and \vec{k} is the wavevector of the incident radiation. This electric field will induce a sinusoidal polarization within the medium equal to:

$$\vec{P}(\vec{r}, t) = \chi(\vec{k}_i, \omega_i) \vec{E}_i(\vec{k}_i, \omega_i) \cos(\vec{k}_i \cdot \vec{r} - \omega_i t) \quad (2.2)$$

where $\chi(\vec{k}_i, \omega_i)$ is the susceptibility of the medium. The polarization has the same frequency and wavevector as the incident planewave. One can expand $\chi(\vec{k}_i, \omega_i)$ as a Taylor series in the normal modes of vibration of the system $\vec{Q}(\vec{r}, t)$. Here, $\vec{Q}(\vec{r}, t)$ is defined to be:

$$\vec{Q}(\vec{r}, t) = \vec{Q}(\vec{q}, \omega_0) \cos(\vec{q} \cdot \vec{r} - \omega_0 t) \quad (2.3)$$

where \vec{q} and ω_0 are the wavevector and frequency of the normal mode phonons. Expanding the susceptibility in terms of equation 2.3 yields

$$\begin{aligned}\chi(\vec{k}_i, \omega, \vec{Q}) &= \sum_{n=0}^{\infty} \left[\frac{1}{n!} \left(\frac{\partial^n \chi}{\partial \vec{Q}^n} \right)_0 \vec{Q}^n(\vec{r}, t) \right] \\ &= \chi_0(\vec{k}_i, \omega_i) + \left(\frac{\partial \chi}{\partial \vec{Q}} \right)_0 \vec{Q}(\vec{r}, t) + \dots\end{aligned}\quad (2.4)$$

Here χ_0 is the electric susceptibility with no fluctuations and the first-order differential of χ is an oscillatory susceptibility induced by normal modes in the medium. For this classical representation, one only needs to expand the susceptibility to first order in $\vec{Q}(\vec{r}, t)$. Substituting equation (2.4) into equation (2.2) yields the induced polarization:

$$\begin{aligned}\vec{P}(\vec{r}, t, \vec{Q}) &= \vec{P}_0(\vec{r}, t) + \vec{P}_{ind}(\vec{r}, t, \vec{Q}) \\ \text{where } \vec{P}_0(\vec{r}, t) &= \chi_0(\vec{k}_i, \omega_i) \vec{E}_i(\vec{k}_i, \omega_i) \cos(\vec{k}_i \cdot \vec{r} - \omega_i t) \\ \text{and } \vec{P}_{ind}(\vec{r}, t, \vec{Q}) &= \left(\frac{\partial \chi}{\partial \vec{Q}} \right)_0 \vec{Q}(\vec{r}, t) \vec{E}_i(\vec{k}_i, \omega_i) \cos(\vec{k}_i \cdot \vec{r} - \omega_i t) \\ &= \left(\frac{\partial \chi}{\partial \vec{Q}} \right)_0 \vec{Q}(\vec{q}, \omega_0) \cos(\vec{q} \cdot \vec{r} - \omega_0 t) \vec{E}_i(\vec{k}_i, \omega_i) \cos(\vec{k}_i \cdot \vec{r} - \omega_i t) \\ \text{or } \vec{P}_{ind}(\vec{r}, t, \vec{Q}) &= \frac{1}{2} \left(\frac{\partial \chi}{\partial \vec{Q}} \right)_0 \vec{Q}(\vec{q}, \omega_0) \vec{E}_i(\vec{k}_i, \omega_i) \\ &\quad \times \{ \cos \left[(\vec{k}_i + \vec{q}) \cdot \vec{r} - (\omega_i + \omega_0) t \right] \\ &\quad + \cos \left[(\vec{k}_i - \vec{q}) \cdot \vec{r} - (\omega_i - \omega_0) t \right] \}\end{aligned}\quad (2.5)$$

Two different sinusoidal waves compose the induced polarization, one with wavevector $\vec{k}_S = (\vec{k}_i - \vec{q})$ and frequency $\omega_S = (\omega_i - \omega_0)$ which is the Stokes-shifted wave and the other with wavevector $\vec{k}_{AS} = (\vec{k}_i + \vec{q})$ and frequency $\omega_{AS} = (\omega_i + \omega_0)$ which is the anti-Stokes-shifted wave.

2.2.2 Quantum Theory

In reality, the Raman effect is a quantum-mechanical interaction. Assume that the system starts in an initial state $|i\rangle$ with all the electrons in the ground state, and some number, $N_i(\omega_i)$, of incident photons with frequency ω_i , some number $N_i(\omega_s)$, of scattered photons with frequency ω_s , and some number $N_i(q)$, of phonons. After a Stokes Raman scattering event, the system will be in the final state $|f\rangle$, with all the electrons remaining in the ground state and $N_f(\omega_i) = N_i(\omega_i) - 1$ photons, $N_f(\omega_s) = N_i(\omega_s) + 1$ photons, $N_f(q) = N_i(q) + 1$ phonons. After an anti-Stokes scattering event, the final state $|f\rangle$ still has all the electrons in the ground state, and $N_f(\omega_i) = N_i(\omega_i) - 1$ photons, $N_f(\omega_s) = N_i(\omega_s) + 1$ photons, but $N_f(q) = N_i(q) - 1$ phonons.

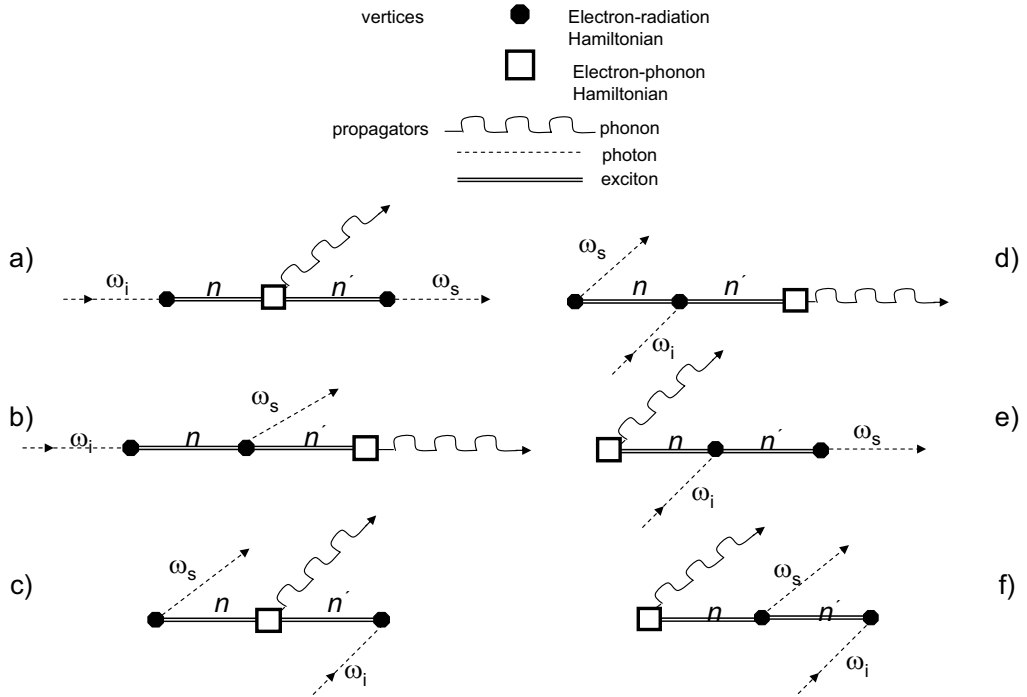


Figure 2.2: Feynman diagrams for the six scattering processes that contribute to Stokes Raman scattering and are commonly found in the literature. See for example reference [149].

The coupling between photons and phonons is very weak. Although all the electrons are in the same initial and final states, the scattering process is mediated by excited virtual states and an electron-phonon interaction Hamiltonian $\mathcal{H}_{\text{e-ion}}$. It is possible to draw a Feynman diagram for the interactions involved during a Raman scattering event. In Feynman diagrams, lines lead from excitations (propagators) into interactions (vertices). Arrows represent propagators, indicating creation (an arrow pointing away from a vertex) or annihilation (an arrow pointing towards a vertex) in an interaction. Given a single Feynman diagram for an interaction (as in Figure 2.2 a), it is possible to derive the other processes by just permutating the time order of the vertices of the original process. Therefore, one can see that there are in fact six possible scattering processes that will lead to Stokes scattering. Figure 2.2 shows all six Feynman diagrams representing these possible scattering processes, but I will discuss the process in only subFigure 2.2 (a) in detail. Since each vertex in the Feynman diagram represents an interaction, the probability of the interaction can be derived from the Fermi Golden rule and will have the general form:

$$P \propto \left| \sum_n \frac{\langle n | \mathcal{H} | i \rangle}{[\hbar\omega_i - (E_n - E_i)]} \right|^2 \quad (2.6)$$

where $|i\rangle$ is the initial state with energy E_i , $|n\rangle$ is an intermediate electronic state with energy E_n and \mathcal{H} is the Hamiltonian describing a particular interaction between states $|i\rangle$ and $|n\rangle$. Stepping through the interactions in Figure 2.2 (a) allows one to quickly write down the entire quantum-mechanical interaction for Stokes Raman scattering by simply multiplying terms from successive vertices. Multiplying the specific three vertices in Figure 2.2 (a) together yields:

$$P = \left(\frac{2\pi}{\hbar} \right) \left| \sum_{n,n'} \frac{\langle f | \mathcal{H}_{\text{e-R}}(\omega_s) | n' \rangle \langle n' | \mathcal{H}_{\text{e-ion}}(\omega_o) | n \rangle \langle n | \mathcal{H}_{\text{e-R}}(\omega_i) | i \rangle}{\Delta E_1 \Delta E_2 \Delta E_3} \right|^2 \quad (2.7)$$

$$\Delta E_1 = [\hbar\omega_i - (E_n - E_i)] \quad (2.8)$$

$$\Delta E_2 = [\hbar\omega_i - (E_n - E_i) - \hbar\omega_o - (E_{n'} - E_n)] \quad (2.9)$$

$$\Delta E_3 = [\hbar\omega_i - (E_n - E_i) - \hbar\omega_o - (E_{n'} - E_n) - \hbar\omega_s - (E_f - E_{n'})] \quad (2.10)$$

where $\mathcal{H}_{\text{e-R}}$ is the Hamiltonian for the electron-radiation interaction between the incident or scattered photon and the electrons of the system. $\mathcal{H}_{\text{e-ion}}$ is the electron-phonon interaction Hamiltonian which describes how an electron-hole pair is scattered when emitting a phonon. $|i\rangle, |n\rangle, |n'\rangle$, and $|f\rangle$ are the initial, possible intermediate and final states of the system. $\hbar\omega_i$ and $\hbar\omega_s$ are the energies of the incident and scattered photons respectively while $\hbar\omega_o$ is the energy of the scattered phonon.

One can simplify equation (2.7) slightly. First, equation (2.9) is equivalent to $\Delta E_2 = [\hbar\omega_i - \hbar\omega_o - (E_{n'} - E_i)]$, while equation (2.10) becomes $\Delta E_3 = [\hbar\omega_i - \hbar\omega_o - \hbar\omega_s - (E_i - E_f)]$. As previously mentioned Raman scattering does not change the final state of the electrons of a system, so $E_i = E_f$ and equation (2.10) further simplifies to $\Delta E_3 = [\hbar\omega_i - \hbar\omega_o - \hbar\omega_s]$. This will vanish if energy is conserved in the scattering process, so one can replace this denominator factor with the delta function: $\delta[\hbar\omega_i - \hbar\omega_o - \hbar\omega_s]$. This delta function further simplifies equation (2.9) since $\hbar\omega_i - \hbar\omega_o = \hbar\omega_s$, so $\Delta E_2 = \hbar\omega_s - (E_{n'} - E_i)$. Substituting these simplifications into equation (2.7) yields the final scattering probability for one possible Raman process:

$$P = \left(\frac{2\pi}{\hbar} \right) \left| \sum_{n,n'} \frac{\langle i | \mathcal{H}_{\text{e-R}}(\omega_s) | n' \rangle \langle n' | \mathcal{H}_{\text{e-ion}}(\omega_o) | n \rangle \langle n | \mathcal{H}_{\text{e-R}}(\omega_i) | i \rangle}{[\hbar\omega_i - (E_n - E_i)] [\hbar\omega_s - (E_{n'} - E_i)]} \right|^2 \dots \dots \times \delta[\hbar\omega_i - \hbar\omega_o - \hbar\omega_s] \quad (2.11)$$

To account for all the different possible processes (the other five Feynman diagrams pictured in Figure 2.2) one must simply repeat this procedure for each

process depicted as a subfigure in Figure 2.2 and sum the resulting terms. This yields the total probability for scattering.

2.2.3 Temperature Effects

Temperature will affect a crystal in two distinct manners, typically referred to as implicit and explicit temperature effects. One can quantify how each of these effects change the vibrational energy of a Raman mode:

$$\left(\frac{\partial\nu}{\partial T}\right)_P = \left(\frac{\partial\nu}{\partial T}\right)_T - \left(\frac{\alpha}{\beta}\right) \left(\frac{\partial\nu}{\partial P}\right)_T \quad (2.12)$$

where

$$\alpha = \left(\frac{1}{V}\right) \left(\frac{\partial V}{\partial T}\right)_P$$

is the expansivity of the material and

$$\beta = \left(\frac{1}{V}\right) \left(\frac{\partial V}{\partial P}\right)_T$$

is the compressibility of the material.

The first term in equation (2.12) is the explicit temperature effect related to changes in the phonon occupation number that occur with changes in temperature. The second term is the implicit temperature effect that quantifies the change in vibrational frequency due to thermal expansion and contraction of the crystal lattice with temperature.

In practice, lowering the temperature of a material will cause Raman lines both to narrow and to shift to higher frequency. Because the weak van der Waals force bond lengths change more than the covalent bond lengths during thermal contraction, intermolecular modes will vary disproportionately when exposed to changes in temperature compared to intramolecular modes.

2.2.4 Resonant Raman Effect

Raman scattering does not yield information about only the vibrational modes of a material studied. Looking closely at the denominator in equation (2.11), one can see there exists the possibility of a singularity if the energy of the incident or scattered photon is equal to the transition energy between an intermediate virtual state and the initial state of the system. Stated slightly differently, if the incident or scattered photon's energy is equal to the energy of an electronic transition in the material, the vibration and electronic states can couple, leading to a large enhancement of the scattering probability. This resonance allows one to extract information directly about the electronic states of the system, because the summation in equation (2.11) is dominated by one (or at most a few) intermediate states and the sums over n and n' collapse. In order to avoid the unphysical situation implied by the potential divergence of the denominator in equation (2.11), one must remember that intermediate states have a finite lifetime due to different decay processes, so that the energy of the state $(E_n - E_i)$ must be replaced by the complex energy $(E_n - E_i) - i\Gamma_n$. Therefore, the final probability for Raman scattering by a single photon is:

$$P = \left(\frac{2\pi}{\hbar}\right) \left| \sum_{n,n'} \frac{\langle i | \mathcal{H}_{e-R}(\omega_s) | n' \rangle \langle n' | \mathcal{H}_{e-ion}(\omega_o) | n \rangle \langle n | \mathcal{H}_{e-R}(\omega_i) | i \rangle}{[\hbar\omega_i - (E_n - E_i) - i\Gamma_n] [\hbar\omega_s - (E_{n'} - E_i) - i\Gamma_{n'}]} \right|^2 \dots \times \delta[\hbar\omega_i - \hbar\omega_o - \hbar\omega_s] \quad (2.13)$$

Having the energy of the incident or scattered photon approach that of an electronic transition is not enough to guarantee a resonant enhancement of a vibrational mode, though. The matrix element for that intermediate state must also be non-negligible ($\langle i | \mathcal{H}_{e-R}(\omega_s) | n' \rangle$, or $\langle n' | \mathcal{H}_{e-ion}(\omega_o) | n \rangle \neq 0$). Finally, the phonon (vibrational mode) and electronic intermediate state must have the same symmetry so that the two states are allowed to couple.

2.2.5 Experimental Setup

In these experiments, Raman spectra were dispersed using a Dilor XY triple spectrometer in a backscattering configuration and collected using a charge-coupled device (CCD) cooled with LN₂. The resolution of the spectrometer is 1 cm⁻¹. A schematic for the spectrometer is shown in Figure 2.3.

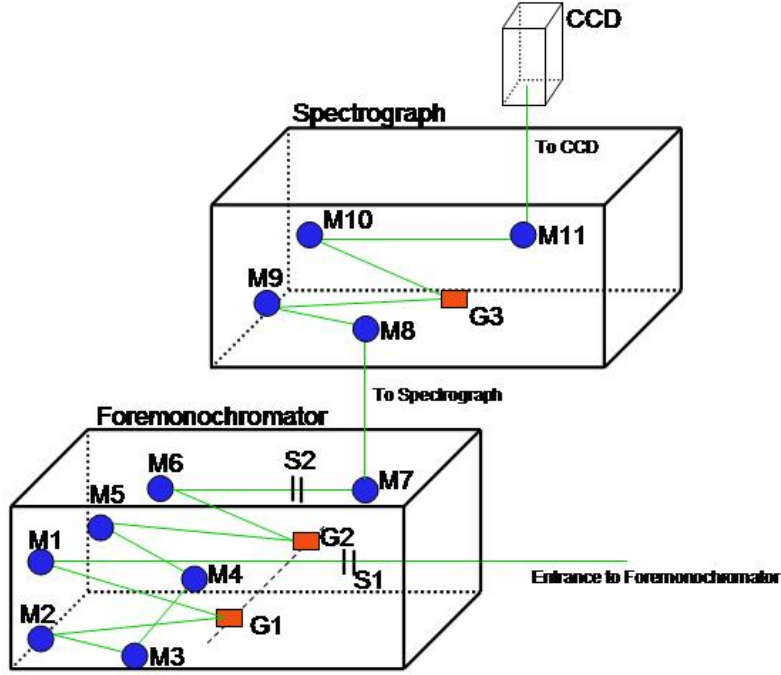


Figure 2.3: Raman Spectrometer Schematic. M1-M11 are mirrors, G1, 2 and 3 are gratings and S1 and 2 are slits in the system.

A variety of α -hexathiophene crystallites were used at different times throughout the experiments. All of the different crystallites were from the same crystal growth run. The crystallites were cooled to 33 K (for α -hexathiophene) or 18 K (for rubrene) with an Air Products closed-cycle He refrigerator in a vacuum chamber pumped down to approximately 3×10^{-6} Torr with a diffusion pump vacuum system.

I mounted the α -hexathiophene crystals with vacuum grease such that the

bc -plane was perpendicular to the incoming laser beam. I did not intentionally control the orientation of the \vec{b} and \vec{c} axes in the plane of the crystal. All of the reported measurements, therefore, average over the different polarizations. In one experiment I attempted to rotate the crystal through different orientations and measure actual polarization effects. Unfortunately, the resulting signal-to-noise ratio was too small for a meaningful analysis because of the reduced efficiency of the gratings in the spectrometer to perpendicularly polarized photons.

I used a Spectra Physics 2017 Ar⁺ laser to pump a Spectra Physics 375B dye laser with an organic dye. For the α -hexathiophene experiments, I chose Rhodamine 6G dye for the dye. I can tune the output energy of the laser with this dye in a continuously tunable range from 1.97 eV to 2.17 eV (629.3 nm to 571.3 nm). I acquired spectra in energy steps that ranged from 20 meV when scanning far from the resonant energy to 1 meV close to the resonant energy. The spectral windows ranged from approximately 70 cm⁻¹ to 1600 cm⁻¹, which includes both inter- and intra-molecular vibrations. The integration time for each scan depended on the excitation wavelength in use, but I chose it to maximize the signal-to-noise ratio while protecting the CCD from saturation from the background luminescence. As the excitation energy approached the band gap, the background luminescence increased; therefore, I averaged multiple shorter scans together to improve the signal-to-noise ratio of the data. I fit all peaks using a least-squares routine with a Voigt lineshape (where the Raman signal is assumed to be pure Lorentzian but equipment effects convolve the signal with a Gaussian distribution).

For the rubrene samples, I initially used multiple crystallites from the same growth batch, again mounted with vacuum grease, in the previously described refrigerator. I conducted a follow-up experiment at room temperature using the largest three-dimensional crystallites from different growth runs. Again, I did not pay any deliberate attention to the orientation of the crystallites at the time of mounting, so any polarization effects will therefore average out over the en-

tire group of crystals. I also made another attempt to investigate the effects of polarization, but the resulting signal-to-noise ratio was still not large enough to allow me to determine experimentally the symmetry of different modes. Studying multiple crystals also allowed me to investigate the consistency of crystals produced in a single growth run. Rubrene is known to highly favor creating a peroxide layer in the presence of light and oxygen [136]. I made no attempts to keep the crystals dry or in the dark, so room-temperature, ambient-pressure measurements are of both the underlying bulk rubrene crystal and the surface peroxide layer.

In the rubrene experiments, I used Kiton Red dye in the dye laser, yielding an output energy in a continuously tunable range from 608 to 711 nm (2.04 - 1.74 eV). I chose a single excitation wavelength of 653.55 nm (1.897 eV) in the experiments to minimize the photoluminescence from the sample in order to measure the weaker Raman effect. I collected data over the spectral range of approximately 35 cm^{-1} to 1600 cm^{-1} , again to include both intermolecular and intramolecular vibrations. These peak fits used a Lorentzian lineshape with a least-squares algorithm. For these experimental runs, compared to the α -hexathiophene measurements, I was able to improve my data analysis techniques. A new beam path design external to the spectrograph increased the power of the incident laser that reached the sample. More accurate collection of flat and dark spectra also allowed me to subtract out equipment effects like the non-linear response of the CCD. I found that Lorentzian rather than Voigt lineshapes were more appropriate after these improvements to fit the data.

2.3 Infrared Spectroscopy

Infrared Spectroscopy (IR) is a physical process almost identical to Raman spectroscopy, except for the distinction that Raman spectroscopy is a scattering process whereas IR spectroscopy is an absorption process. The incident en-

ergy infrared experiments use is in the infrared range, while Raman experiments mostly use incident excitations in the visible range. The selection rules for vibrations to be Raman- or IR- active are different. A mode is infrared-active if the vibration causes a change in the dipole moment of the bond, while a mode is Raman-active if it involves a change in the polarizability of the molecule. For materials with a point of inversion (such as all the molecular crystals discussed in this dissertation), the selection rules are mutually exclusive. Modes that are Raman-active must be IR-inactive and vice versa, so the two experiments form a complementary set of data. Finally, for molecules with a point of inversion, all IR-active modes have ungerade-type symmetry (while the Raman-active modes have gerade-type symmetry). Gerade-modes have even parity with respect to the inversion point of the molecule, while ungerade-modes have odd parity with respect to the same inversion point.

Arthur Ramirez and his student at Lucent Technologies recorded the infrared data reported in Section 4.2. Christian Kloc grew the rubrene crystals used in these measurements in the same or very similar growth runs to the crystals I used in the Raman and photoluminescence experiments.

2.4 Photoluminescence Spectroscopy

Photoluminescence spectroscopy (PL) is different from Raman and IR spectroscopy in that PL is the direct emission of light from an excited medium rather than the scattering of light and, as such, involves real rather than virtual excitations of electrons.

In PL, an excitation source optically pumps a material. Typically, this excitation source is greater in energy than the band gap of the material, in order to promote electrons to excited states. After a relaxation period, electrons that fall back to lower states through radiative recombination pathways emit photons, as shown schematically in Figure 2.4. Because of the thermal relaxation, the

Energy Level Diagram

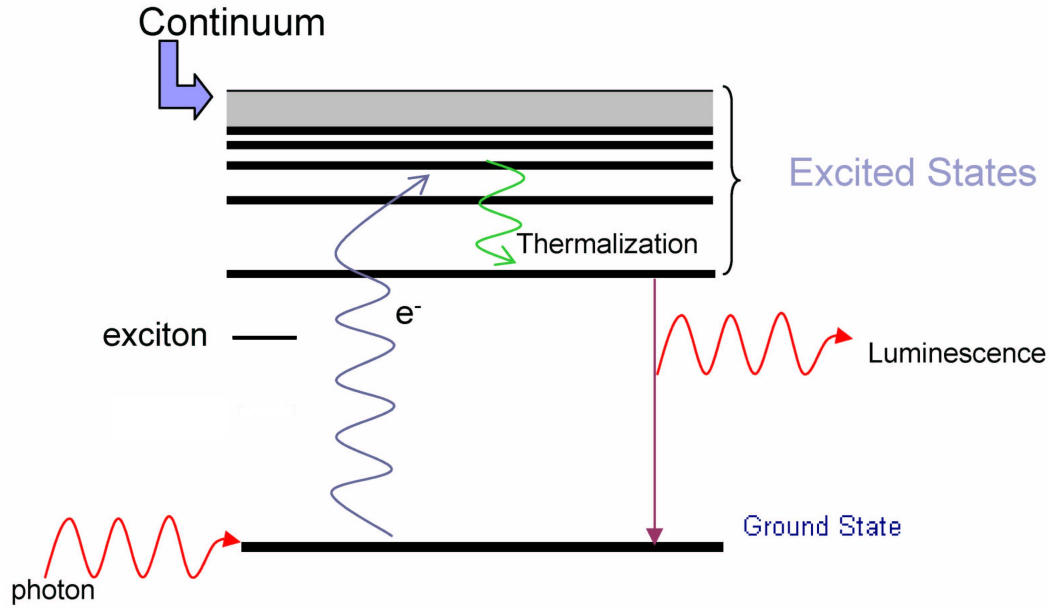


Figure 2.4: Photoluminescence Schematic

emitted photons have no correlation with the excitation process.

2.4.1 Photoluminescence Theory

It is impossible to discuss the emission of light without first considering the absorption of light, as the two processes are closely tied. Essentially, one can think of stimulated emission as the inverse of the absorption process; Einstein's B coefficient describes the rates of both of these processes. The Einstein coefficient A_{nm} describes the rate for spontaneous emission due to a transition from energy level n to m , while B_{nm} is the rate for either absorption or stimulated emission from level n to level m . Einstein showed $B_{nm} = B_{mn}$. In photoluminescence, one is mostly interested in spontaneous emission from a material. Luckily, the rate of spontaneous emission is related to that of stimulated emission:

$$A_{nm} = \frac{16\pi^2 \hbar \nu^3 n_\tau^3}{c^3} B_{nm} \quad (2.14)$$

where ν is the wavelength of the photon and n_τ is the refractive index of the medium. This Einstein A coefficient determines the rate for radiative transitions between two levels. If the upper level has a population N at time t , the radiative emission rate is:

$$\left(\frac{dN}{dt} \right)_{\text{radiative}} = -A_{nm}N \quad (2.15)$$

Solving this to find the population of the upper state as a function of time yields:

$$N(t) = N(0)e^{-At} = N(0)e^{-t/\tau_R} \quad (2.16)$$

where $\tau_R = A^{-1}$ is the radiative lifetime of the transition. Therefore, transitions which have large absorption coefficients also have high emission probabilities and short radiative lifetimes.

Electrons can also relax through non-radiative pathways, for example by emitting phonons or binding to traps. One can determine the photoluminescence efficiency η_R by considering non-radiative relaxation pathways. Taking both pathways into account, and using τ_{NR} for the non-radiative rate, one can then write the total emission rate of the excited state as:

$$\left(\frac{dN}{dt} \right)_{\text{total}} = -\frac{N}{\tau_R} - \frac{N}{\tau_{NR}} = -N \left(\frac{1}{\tau_R} + \frac{1}{\tau_{NR}} \right) \quad (2.17)$$

The photoluminescence efficiency is the ratio of the radiative emission rate to the total de-excitation rate. In other words, divide equation (2.15) by equation (2.17) to obtain:

$$\eta_R = \frac{AN}{N(1/\tau_R + 1/\tau_{NR})} = \frac{1}{1 + \tau_R/\tau_{NR}} \quad (2.18)$$

The simplification above makes use of the fact that $A = \tau_R^{-1}$ by definition. For a high photoluminescence efficiency, a material needs to have a much shorter radiative lifetime compared to the non-radiative lifetime.

I will discuss the different types of radiative recombination processes that occur regularly in semiconductors individually.

Band-to-Band Transitions (Electron-Hole Recombination)

A band-to-band transition occurs when an excited electron in the conduction band recombines with a hole in the valence band. If the semiconductor has a direct band gap and an allowed electric dipole transition, this recombination occurs with high probability. In indirect bandgap semiconductors, the recombination can only occur if mediated by a phonon. This is a second-order process and will have a lower probability or longer radiative lifetime (τ_R).

Free-to-Bound Transitions

The previously discussed band-to-band transitions will often dominate at higher temperatures when shallow impurities ionize. As the temperature of a sample decreases, however, impurities trap carriers. Free electrons can recombine radiatively with holes trapped on acceptors; these are called free-to-bound transitions. The emitted photon will have an energy $\hbar\omega = E_g - E_A$ where E_A is the acceptor's binding energy and E_g is the band gap of the material. Therefore, emission due to free-to-bound transitions is a simple way of measuring impurity binding energies.

Donor-Acceptor Pair Transitions

This type of emission is similar to the previously discussed transition free-to-bound transition. A compensated semiconductor will have both donors and acceptors which will allow for more types of interactions. It is possible for electrons on donors to recombine radiatively with holes on acceptors in a donor-acceptor pair transition. The emitted photon will have the energy $\hbar\omega = E_g - E_A - E_D + \frac{e^2}{4\pi\epsilon_0\epsilon R}$ where E_A is still the acceptor's binding energy and E_D is the donor's binding energy. The $e^2/4\pi\epsilon_0\epsilon R$ term is Coulomb interaction between the ionized donors and acceptors where R is the separation between the donors and acceptors in the material.

Free-Exciton Emission

In high-purity semiconductors, photoexcitation often leads to the generation of free excitons (bound electron-hole pairs). If these excitons annihilate radiatively, a free-exciton peak will be present in the emission spectrum. A first approximation would assume that simple radiative decay leads to free exciton emission, which would be equivalent to a delta function at the exciton ground state energy. Broadening effects from the lifetime of the exciton, however, would turn this delta function lineshape into a Lorentzian distribution. Actual experimental data, however, indicates that most free-exciton emission peaks are in fact asymmetric in shape. In order to understand this, one must think of the excitons formed as excitonic polaritons. Polaritons are coupled phonon-photon systems which then link to the exciton in discussion. This excitonic polariton can relax towards lower energies by scattering with phonons via their exciton component. However, the photon component of the polariton has a much weaker interaction with phonons, scatters less efficiently which leads to the observed asymmetry in the emission peak shape.

Trapped-Exciton Emission

Finally, if the semiconductor has neutral or ionized donors or acceptors, van der Waals interactions attract the excitons described in the previous section to the impurities, lowering the exciton energy. Therefore the emission energy from a exciton bound to a donor or acceptor will be lower in energy than the free exciton emission peak.

Most likely transitions for organic molecular crystals

For the materials of interest in this thesis, the dominant transitions are going to be the band-to-band transitions described first. As already discussed in Section 1.2.2, rubrene has a near 100% photoluminescence yield, which means that basically all excited electrons will radiatively recombine. The incident energy used in the experiments is greater than the band gap of the material, so photoexcited electrons will start in the conduction band of the crystals. A large peak associated with recombination from the bottom of the conduction band to the top of the valence band will dominate the PL spectrum. Molecular crystals readily form excitons after photoexcitation, so additional features in the photoluminescence spectrum are most likely due to exciton emission (although exciton emission is increasingly likely at lower temperatures - see the discussion of PL temperature effects in Section 2.4.2). Even though the crystals used in these experiments are of very high quality, it is impossible to have perfect crystals. In molecular crystals, the challenge of high purity is even greater than with standard inorganic semiconductors. When you have fairly large molecules stacked together in the solid-state, steric hindrance between the molecules prevents a very rigid lattice. Essentially this means that there are many possible locations for environmental impurities to easily penetrate the lattice. This, in turn, means that when exciton emission occurs, it is often from trapped excitons rather than free excitons.

2.4.2 Temperature Effects

One of the main differences between the absorption and emission transitions is that electrons and holes thermally relax to approximately $k_B T$ from the bottom of the excited state band before being re-emitted. Radiative recombination occurs only between electron and hole states that are thermally occupied. As the electrons have time to relax to within $k_B T$ of the band edge, emission will be from a very narrow energy range near the band edge.

As the temperature of the sample changes, the band edge can shift and follows the following empirical equation:

$$E_g(T) = E_g(0) - \frac{\alpha T^2}{T + \beta} \quad (2.19)$$

where α and β are constants measured for each material and $E_g(0)$ is the band gap energy at zero temperature. As the band edge shifts, the PL emission will also shift since band-to-band transitions dominate the emission. Most often, the band gap will shrink with increasing temperature which means the emission will also redshift with increasing temperature. Also, due to the increased presence of phonons, which broaden electronic levels as the temperature of a material increases, the PL emission thermally broadens with increasing temperature. Therefore, higher temperature measurements often have overlapping peaks that may be more difficult to separate and analyze.

Finally, if the temperature of the sample is larger than the typical exciton binding energy ($k_B T > E_{binding}$), excitons will thermally dissociate and emission from free and trapped excitons will decrease greatly.

2.4.3 Experimental Setup

I collected photoluminescence spectra using a Spex 0.85m 1403 double monochromator and a Hamamatsu photomultiplier tube (PMT). Figure 2.5 pictures a schematic of the experimental beam path for this Spex spectrometer. The

resolution of the spectrometer is variable. Since the PL peaks are intrinsically quite broad, I reduced collection times for scans by setting the resolution to approximately 25 cm^{-1} . I used the same cryostat from the Raman experiments to cool the crystals. A Lakeshore temperature controller regulated the temperature of the cryostat between 18 and 275 K. The photoluminescence experiments used the same rubrene platelets as the Raman measurements. For a description of mounting details please refer to Section 2.2.5. I collected most of the data using the 514.54 nm (2.41 eV) line from the Spectra Physics 2016 Ar⁺ laser; for other data runs, I used other Ar⁺ excitation lines as well as lines from a Liconix 4230NB HeCd laser. Spectra varied over the entire luminescence range of the rubrene crystals (from approximately 518 to 750 nm or 2.393 to 1.653 eV) with a variable step size depending on the resolution desired for a specific scan. The integration time per scan was also varied to maximize the signal-to-noise ratio and account for changes in the photoluminescence efficiency with changing temperature of the sample. After subtracting the background, I fit all peaks with Gaussian lineshapes using a least-squares algorithm.

2.5 Computer Calculations

My collaborator, Shubin Liu, simulated the Raman spectra for isolated molecules of α -hexathiophene, rubrene and tetracene using GAUSSIAN 03 [38]. He used the Hartree-Fock method to do a structural optimization and the density functional theory (DFT) B3LYP method to calculate the Raman frequencies, both with the 6-31G* basis set. He repeated the calculation with GAUSSIAN 03 with both the structural optimization and the frequency simulation done with the DFT B3LYP method and at the 6-31G9(d) basis set level.

Shubin attempted to predict the excited electronic states of the rubrene molecule as well. Using GAUSSIAN 03 he calculated excitation energies for a single molecule system as well as for a two- and a three-molecule configuration.

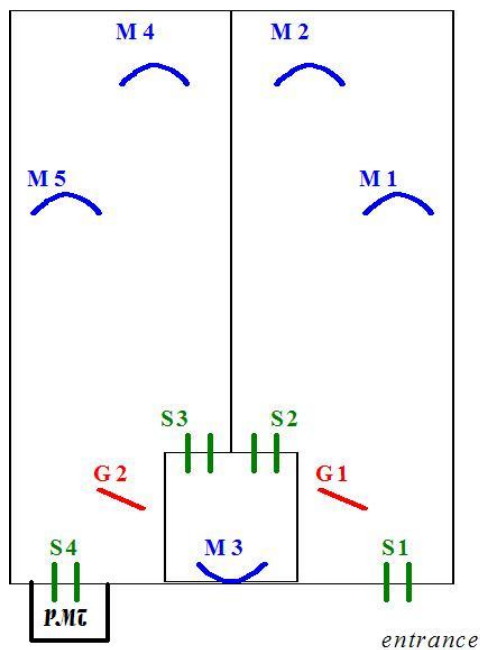


Figure 2.5: Photoluminescence Spectrometer Schematic. M1-M5 are mirrors, G1 and G2 are gratings and S1-S4 are variable slits in the system.

GAUSSIAN 03 did not converge for four molecules (equivalent to the physical unit cell in rubrene single crystals). At the time of the writing of this dissertation, an additional calculation with the CASTEP module from Cerius² [150] is in progress, with a configuration that includes four rubrene molecules in the unit cell orientation and period boundary conditions. So far, the cluster has been working on this configuration for six weeks and it is unclear if it will converge to a solution. All calculations ran on an SGI Origin 3800 with 64 CPUs and 128 GB memory running the IRIX 6.5 OS.

Chapter 3

Raman Spectroscopy of Alpha-Hexathiophene

The room-temperature and low-temperature Raman spectra of α -hexathiophene measured in our lab closely match spectra available in the literature. Resonant Raman measurements of α -hexathiophene at 33 K have identified twelve vibrational modes that couple to electronic excitations in the single crystal [72]. These excitations, at 2.066 eV and 2.068 eV with a width of 2 meV, are either a bound singlet Frenkel exciton or a triplet Frenkel exciton. The resonance quenches at 55 K. This temperature corresponds to the binding energy of the trap in the case of a singlet exciton or the binding energy of the triplet exciton. I discuss these experiments and results below.

3.1 Alpha-Hexathiophene Crystals

α -hexathiophene is a small, aromatic hydrocarbon of six thiol rings bonded at the α -carbons (the carbons associated with the sulfur atom) as shown in Figure 3.1. Christian Kloc at Lucent Technologies grew the crystals by horizontal vapor growth. The crystallites are a few microns thick and millimeters in lateral dimension. The growth process yields platelets with the \vec{bc} axes in the plane of

the crystallites. The molecule crystallizes in a monoclinic $P2_1/n$ space group, and has C_{2h} point group symmetry with four molecules in the unit cell. The lattice constants for the monoclinic unit cell are: $|\vec{a}| = 44.7 \text{ \AA}$, $|\vec{b}| = 7.851 \text{ \AA}$, and $|\vec{c}| = 6.029 \text{ \AA}$ [60]. Figure 3.2 shows the molecular stacking in the single crystal. My collaborator, Shubin Liu, calculated the geometric structure of the molecule, following the atomic labeling scheme in Figure 3.1. The structure is also found in the literature from both X-ray measurements and theoretical calculations [56,57]. Table 3.1 lists the experimental and theoretical atomic bond lengths and angles. It is important to note how closely the calculations performed at UNC follow the published theory and measured values.

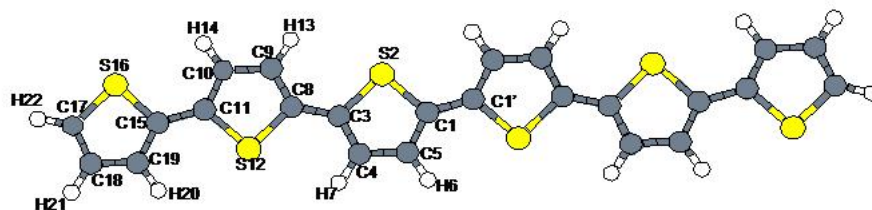


Figure 3.1: Alpha-hexathiophene ($C_{20}H_{14}S_6$) Molecule: the labels on the atoms are in reference to Table 3.1

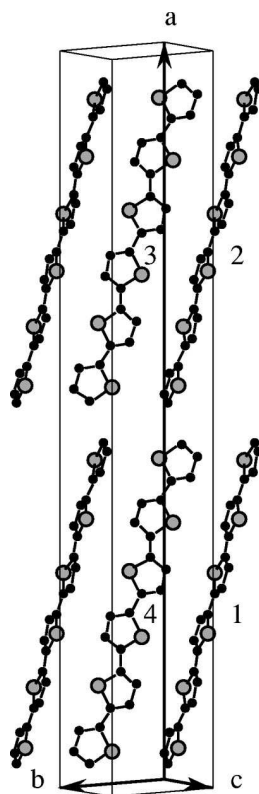


Figure 3.2: Molecular Stacking in the Unit Cell of α -hexathiophene

Table 3.1: Comparison of experimental and theoretical geometrical structures of α -hexathiophene molecules. Refer to the atomic labeling scheme in Figure 3.1. Data in the columns labeled Theory_{Lit} and Exp_{Lit} are from the work of Esposti, *et al.* [56, 57]. That group used GAUSSIAN 94 with basis set 3-21G* for their calculations. The data from the column labeled Theory_{UNC} were calculated by Shubin Liu using GAUSSIAN 03 and the 631G9(d) basis set.

	Theory _{Lit}	Exp _{Lit}	Theory _{UNC}
Distances			
C ₁ C _{1'}	1.455 Å	1.445 Å	1.423 Å
C ₃ C ₈	1.455 Å	1.45-1.46 Å	1.423 Å
C ₁₁ C ₁₅	1.457 Å	1.45 Å	1.428 Å
C ₁ S ₂	1.734 Å	1.730-1.731 Å	1.827 Å

Continued on the next page

Table 3.1 cont.

	Theory _{Lit}	Exp _{Lit}	Theory _{UNC}
S ₂ C ₃	1.732 Å	1.733-1.739 Å	1.827 Å
C ₁₁ S ₁₂	1.734 Å	1.729-1.733 Å	1.826 Å
C ₈ S ₁₂	1.734 Å	1.733-1.742 Å	1.827 Å
C ₁₅ S ₁₆	1.735 Å	1.719-1.726 Å	1.828 Å
C ₁₇ S ₁₆	1.721 Å	1.704-1.711 Å	1.804 Å
C ₁ C ₅	1.354 Å	1.37-1.38 Å	1.376 Å
C ₃ C ₄	1.354 Å	1.36 Å	1.375 Å
C ₈ C ₉	1.354 Å	1.36 Å	1.375 Å
C ₁₀ C ₁₁	1.354 Å	1.38 Å	1.373 Å
C ₁₅ C ₁₉	1.354 Å	1.38-1.40 Å	1.372 Å
C ₁₇ C ₁₈	1.348 Å	1.31-1.32 Å	1.360 Å
C ₄ C ₅	1.428 Å	1.40-1.41 Å	1.418 Å
C ₉ C ₁₀	1.429 Å	1.40 Å	1.420 Å
C ₁₈ C ₁₉	1.433 Å	1.41-1.42 Å	1.432 Å
C ₅ H ₆	1.069 Å	-	1.082 Å
C ₄ H ₇	1.069 Å	-	1.082 Å
C ₉ H ₁₃	1.069 Å	-	1.082 Å
C ₁₀ H ₁₄	1.069 Å	-	1.082 Å
C ₁₉ H ₂₀	1.069 Å	-	1.082 Å
C ₁₈ H ₂₁	1.069 Å	-	1.081 Å
C ₁₇ C ₂₂	1.067 Å	-	1.078 Å
Angles			
C ₅ C ₁ C _{1'}	127.9°	128.7°	129.8°
S ₂ C ₁ C _{1'}	121.2°	120.9°	120.1°
S ₂ C ₃ C ₄	111.0°	110.5-111.3°	110.1°

Continued on the next page

Table 3.1 cont.

	Theory _{Lit}	Exp _{Lit}	Theory _{UNC}
C ₁ S ₂ C ₃	91.9°	91.9-91.8°	89.8°
C ₃ C ₄ C ₅	113.1°	113.4-113.8°	115.0°
S ₂ C ₃ C ₈	121.2°	119.6-119.3°	120.1°
S ₁₂ C ₈ C ₅	121.2°	119.9-119.7°	120.1°
C ₃ C ₈ C ₉	127.9°	129.4-129.7°	129.8°
C ₈ S ₁₂ C ₁₁	91.9°	91.9-91.8°	89.9°
C ₈ C ₉ C ₁₀	113.1°	113.7-114.0°	114.9°
C ₁₇ C ₁₈ C ₁₉	112.5°	113-.1-113.6°	114.2°
S ₁₆ C ₁₅ C ₁₁	121.2°	120.9-121.1°	120.1°
S ₁₂ C ₁₁ C ₁₅	121.1°	121.0-121.4°	120.0°
C ₁₅ S ₁₆ C ₁₇	91.6°	91.2-91.6°	89.6°
H ₆ C ₅ C ₁	123.4°	-	122.1°
H ₇ C ₄ C ₃	123.4°	-	122.1°
H ₁₃ C ₉ C ₈	123.4°	-	122.1°
H ₁₄ C ₁₀ C ₁₁	123.4°	-	122.1°
H ₂₀ C ₁₉ C ₁₅	123.4°	-	122.3°
H ₂₁ C ₁₈ C ₁₇	124.0°	-	123.0°
H ₂₂ C ₁₇ C ₁₈	127.1°	-	129.0°

3.2 Room Temperature Experiments

As mentioned in Section 1.2.1, previous researchers have measured the vibrational spectra of α -hexathiophene using infrared and Raman spectroscopies as well as inelastic neutron scattering [55, 57]. In order to compare the quality and composition of the crystals from Lucent Technologies with that referenced in the literature, I first measured the Raman spectrum of single crystals of α -

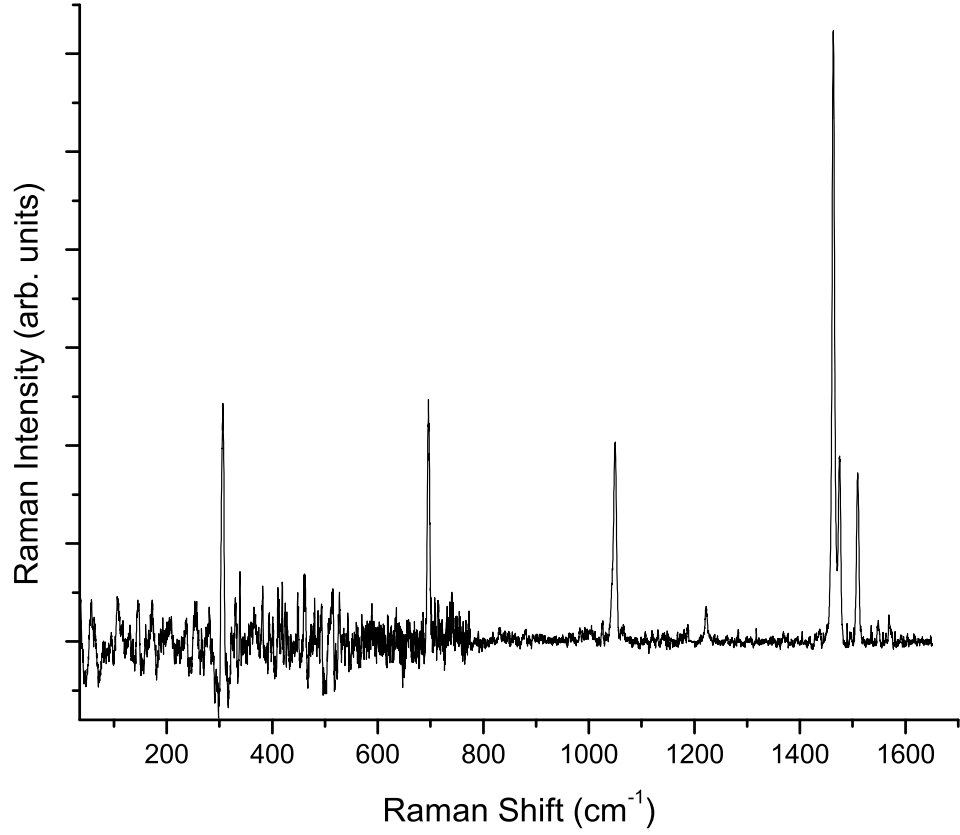


Figure 3.3: Room-temperature Raman spectrum of α -hexathiophene with $\lambda_{exc}=607$ nm (2.043 eV)

hexathiophene at room temperature. Figure 3.3 is a reproduction of this off-resonance, room-temperature spectrum of α -hexathiophene. The signal-to-noise ratio clearly changes with energy across this representative spectrum, because the spectrum in Figure 3.3 is in reality an amalgam of multiple individual scans at different spectrometer settings. At this excitation wavelength the photoluminescence from the α -hexathiophene crystals noticeably decreases with increasing Raman shift. Practically, this means that it is easier to subtract the background at higher Raman shifts, leading to larger signal-to-noise ratios for higher-energy Raman modes.

Comparing the measured spectrum with that available in the literature shows a close correspondence between peaks that I measured and peaks identified by other researchers. There are additional experimentally-measured peaks cited in the literature, but they are not visible above the noise in the spectra reported here. Table 3.2 lists the peak positions for experimentally-measured and theoretically-predicted intramolecular Raman modes. Table 3.3 contains highlights from Table 3.2, focusing only on the experimentally-observed, strongest modes.

Table 3.2: Peak positions and intensities for intramolecular Raman modes from the the work of Esposti, *et al.* [55] as well as those measured and calculated at UNC. The symmetry assignments for the vibrational modes are from the work of Esposti, *et al.*. Some of the modes seen originally by Esposti, *et al.*, are not visible above the noise in the nonresonant spectrum, but are clearly visible with excitation energies near the electronic transitions and are relisted in Table 3.4. The spectra were collected with $\lambda_{exc}=1024\text{ nm}$ (1.21 eV) and $\lambda_{exc}=632.8\text{ nm}$ (1.96 eV) (marked with an †) by Esposti, *et al.*, and with $\lambda_{exc}=607\text{ nm}$ (2.043 eV) or $\lambda_{exc}=599.43\text{ nm}$ (2.068 eV) (marked with a ‡) in this work.

Sym	Exp _{Lit} (cm ⁻¹)	Theory _{Lit} (arb. units)	Int _{Lit} (cm ⁻¹)	Theory _{UNC} (cm ⁻¹)	Int _{UNC} (arb. units)	Exp _{UNC} (cm ⁻¹)
1A _g	3110	3103.1	552	3185.6	929	
2A _g	3102	3071.2	390	3131.1	564	
2A _g	3081	3071.0	131			
4A _g		3070.8	51.8	3127	336	
5A _g	3070	3057.3	30			
6A _g	3065	3057.1	71	3116.9	556	
7A _g	3057	3057.0	354	3114.4	236	
8A _g	1562	1554.1	965	1590.3	1421	1592 †
9A _g	1541	1536.4	367	1565.8	4904	1587 ‡

Continued on the next page

Table 3.2 cont.

Sym	Exp _{Lit} (cm ⁻¹)	Theory _{Lit} (arb. units)	Int _{Lit} (cm ⁻¹)	Theory _{UNC} (cm ⁻¹)	Int _{UNC} (arb. units)	Exp _{UNC} (cm ⁻¹)
10A _g	1504	1511.4	3740	1522.2	49460	1507
11A _g	1469	1459.6	83030	1463.1	132375	1473
12A _g	1458	1456.7	770	1452.1	414960	1461
13A _g	1426	1436.9	1439	1447.6	55797	1436
14A _g	1366	1378.2	3822	1343.8	47758	
15A _g		1352.8	707	1336.1	47	
16A _g		1300.4	115	1291.4	115.7	1293.5 [‡]
17A _g	1265	1262.6	187	1258	50	
18A _g	1237	1238.3	92			
19A _g	1218	1217.0	30	1212.3	8	1223
20A _g		1204.0	3			
21A _g		1194.1	13	1188.8	4770	
22A _g		1173.5	808	1169.0	14290	
23A _g	1085 [†]	1082.2	115	1163.5	1046	1091 [‡]
24A _g	1067 [†]	1066.0	24	1156.6	1354	1063 [‡]
25A _g	1050	1061.8	5978	1060.9	45	1054
26A _g		1044.4	150	1042.1	27	
27A _g		916.5	2	1024.4	15000 ^a	
1B _g	894 [†]	901.7	28	1018.1	28375 ^b	
2B _g	876 [†]	879.4	180	857.2	36	
28A _g		876.9	1			
3B _g	865 [†]	873.4	6	841.9	110	
29A _g	836 [†]	837.1	16	837.3	2	

Continued on the next page

^aNo good correspondence for this peak

^bNo good correspondence for this peak

Table 3.2 cont.

Sym	Exp _{Lit} (cm ⁻¹)	Theory _{Lit} (arb. units)	Int _{Lit} (cm ⁻¹)	Theory _{UNC} (cm ⁻¹)	Int _{UNC} (arb. units)	Exp _{UNC} (cm ⁻¹)
4B _g	820 [†]	832.7	9	834.1	68	
5B _g	809 [†]	804.8	0.1			
6B _g	800 [†]	796.0	0.1	786.6	52	
30A _g	740	751.3	47	777.2	6	
31A _g		749.5	16	756.4	2	
32A _g	735 [†]	747.7	34	753.6	.1	
33A _g	696	702.0	237	724.2	62	698
7B _g		697.4	4	639.9	30	
34A _g	667 [†]	672.9	16	635.4	5	
35A _g	614 [†]	625.6	13	624.7	4421	
8B _g	588	581.6	61	611.8	205	
9B _g		579.8	21	598.8	237	
10B _g		573.6	4	559.5	144	
11B _g		561.2	6	549.2	5	
12B _g		531.7	1	529.6	3	
36A _g		480.0	11	482.6	6	
13B _g		476.2	1	450.4	0.4	
37A _g		390.4	1			
38A _g	381 [†]	385.7	9	377.8	1	390 [‡]
14B _g	373 [†]	369.9	8	349.7	14	365 [‡]
39A _g	304 [†]	305.5	56			309
40A _g		285.9	6	289.2	1641	296 [‡]
15B _g		276.7	2	266.6	79	269 [‡]
16B _g	203 [†]	178.3	2	181.4	5	209 [‡]
41A _g	145 [†]	147.2	10	150.7	148	145 [‡]

Continued on the next page

Table 3.2 cont.

Sym	Exp _{Lit} (cm ⁻¹)	Theory _{Lit} (arb. units)	Int _{Lit} (cm ⁻¹)	Theory _{UNC} (cm ⁻¹)	Int _{UNC} (arb. units)	Exp _{UNC} (cm ⁻¹)
17B _g	103 [†]	102.5	2	104.4	2	
42A _g	94 [†]	94.7	2	97.2	2	96 [‡]
43A _g		53.8	0.3	75.3	1	
44A _g		33.1	3	38.4	3	

3.3 Temperature Dependent Raman

In order to determine the temperature dependence of the vibrational modes, I collected spectra with fixed excitation wavelengths of 606.95 nm and 598.17 nm (2.043 eV and 2.073 eV) while varying the temperature of the sample from 300 K to 33 K. Figure 3.4 shows this change with temperature for some of the intramolecular modes of α -hexathiophene. As previously discussed in Section 2.2.3, changes in temperature affects intramolecular and intermolecular modes in a crystal differentially. A slight decrease in the lattice spacing causes the main vibrational shift with decreasing temperature, stiffening the bonds and thus shifting the Raman modes to higher frequencies (the second term in equation 2.12). Temperature changes affect the weak intermolecular van der Waals forces more than the covalent intramolecular bonds, resulting in larger shifts for the lower-energy Raman peaks. Lowering the temperature of the crystal also reduces thermal broadening effects because the number of phonons in the system decreases at lower temperatures (the first term in equation 2.12). This can reduce the overlap of peaks, making the identification and fitting of vibrational modes easier at low temperature. These temperature effects are clearly visible

Table 3.3: Highlights from Table 3.2 - peak positions only. Only the modes experimentally observed by Esposti *et al.* [55] are listed in this shortened table. Modes marked by a † were observed with 632.8 nm (1.96 eV) excitation by Esposti *et al.*, the other modes were observed with 1024 nm (1.21 eV) excitation. I observed the modes marked by a ‡ only with a 599.43 nm (2.068 eV) excitation source and they will be discussed in more detail in Section 3.4. The other modes in column E_{exp} were observed with an excitation of 607 nm (2.043 eV).

Symmetry	$E_{\text{literature}}$ (cm^{-1})	E_{exp} (cm^{-1})	% Difference
$8A_g$	1562	1592^\ddagger	1.6%
$9A_g$	1541	1541^\ddagger	1.2%
$10A_g$	1504	1507	0.2%
$11A_g$	1469	1471	0.3%
$12A_g$	1458	1461	0.2%
$13A_g$	1426	1436	0.7%
$19A_g$	1218	1223	0.4%
$23A_g$	1085^\dagger	1091^\ddagger	0.5%
$24A_g$	1067^\dagger	1063^\ddagger	-0.3%
$25A_g$	1050	1054	0.4%
$33A_g$	696	698	0.3%
$38A_g$	381^\dagger	390^\ddagger	2.3%
$14B_g$	373^\dagger	365^\ddagger	-2.2%
$39A_g$	304^\dagger	309	1.6%
$16B_g$	203^\dagger	209^\ddagger	3.3%
$41A_g$	145^\dagger	145^\ddagger	0.0%
$42A_g$	94^\dagger	96^\ddagger	2.1%

in the α -hexathiophene example as upshifts on the order of 0.2% - 0.4% for intramolecular modes (higher-energy modes with frequencies above approximately 300 cm^{-1}). Meanwhile, much larger shifts of approximately 1% - 7% appear for intermolecular modes (lower-energy modes with frequencies below 300 cm^{-1}).

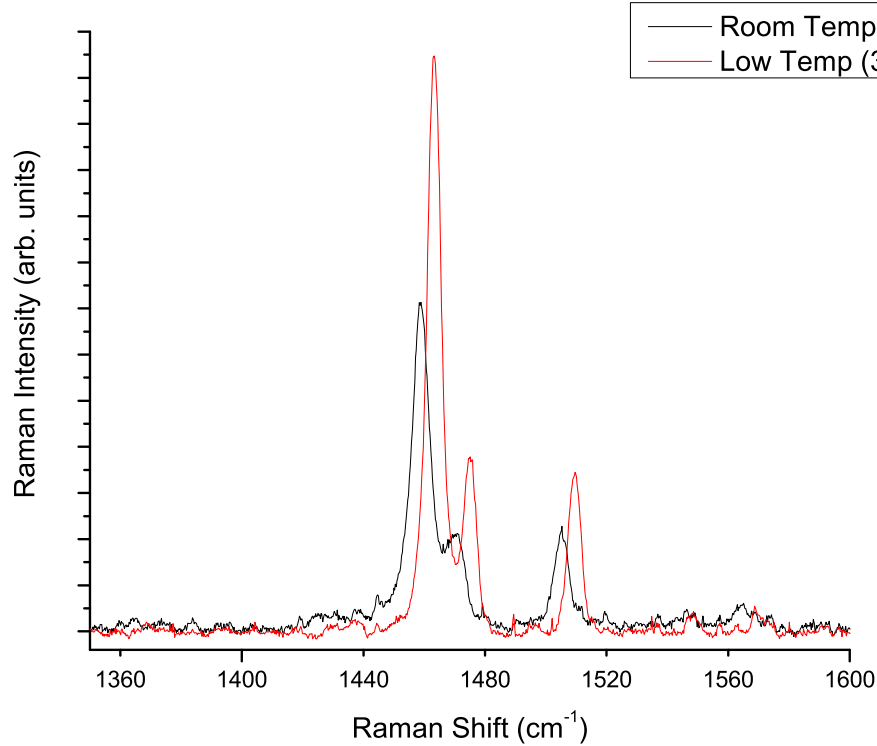


Figure 3.4: Room-temperature and low-temperature (33 K) of α -hexathiophene with $\lambda_{exc}=607$ nm (2.043 eV)

Figure 3.5 shows this temperature dependence for some example modes. These upshifts agree well with the expected shifts in frequency for cooled molecular crystals.

3.4 Resonant Raman Spectroscopy

Although α -hexathiophene behaved as expected for a molecular crystal in room- and low-temperature Raman experiments, it displayed more unusual effects when the incident excitation energy changed. At the resonant excitation energies, I observed seventeen vibrational lines in the 250 - 1600 cm⁻¹ spectral range that no other published spectrum of α -hexathiophene reported. In addi-

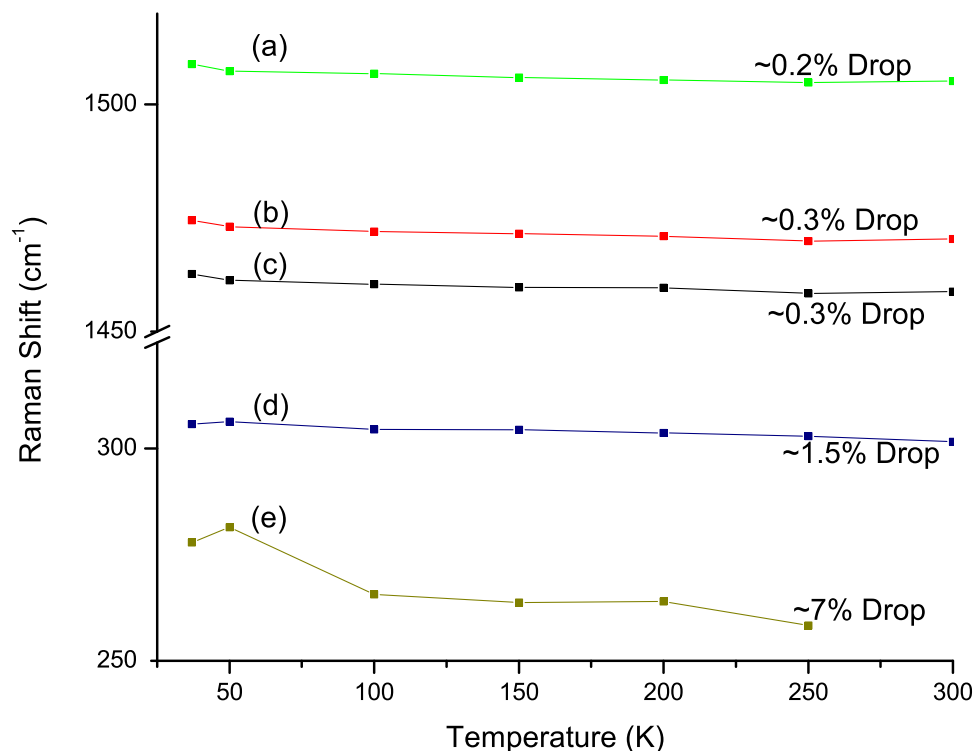


Figure 3.5: Peak position vs. temperature for both intermolecular and intramolecular modes. The peaks were fit with a least-squares routine using Voigt line shapes. Some of the highest-frequency intramolecular modes (with very little temperature dependence) are plotted, along with the strongest intermolecular modes that display up to a 7% shift with temperature. Plot (a) is the temperature dependence of the Raman peak at 1507 cm^{-1} , (b) is the peak at 1473 cm^{-1} , (c) is the peak at 1460 cm^{-1} , (d) is the peak at 304 cm^{-1} , and (e) is the peak at 280 cm^{-1} .

tion, seven lines previously measured by Esposti *et al.* [55] were visible above the noise in the spectrum. Figure 3.6 displays the on-resonance spectrum of α -hexathiophene. The peaks marked with an asterisk all represent resonance interactions. Tables 3.4 and 3.5, respectively list the frequencies for all the newly-measured intramolecular and intermolecular resonant Raman modes and specify which lines Esposti's group previously reported.

Unlike the strong correspondence between the predicted and observed fre-

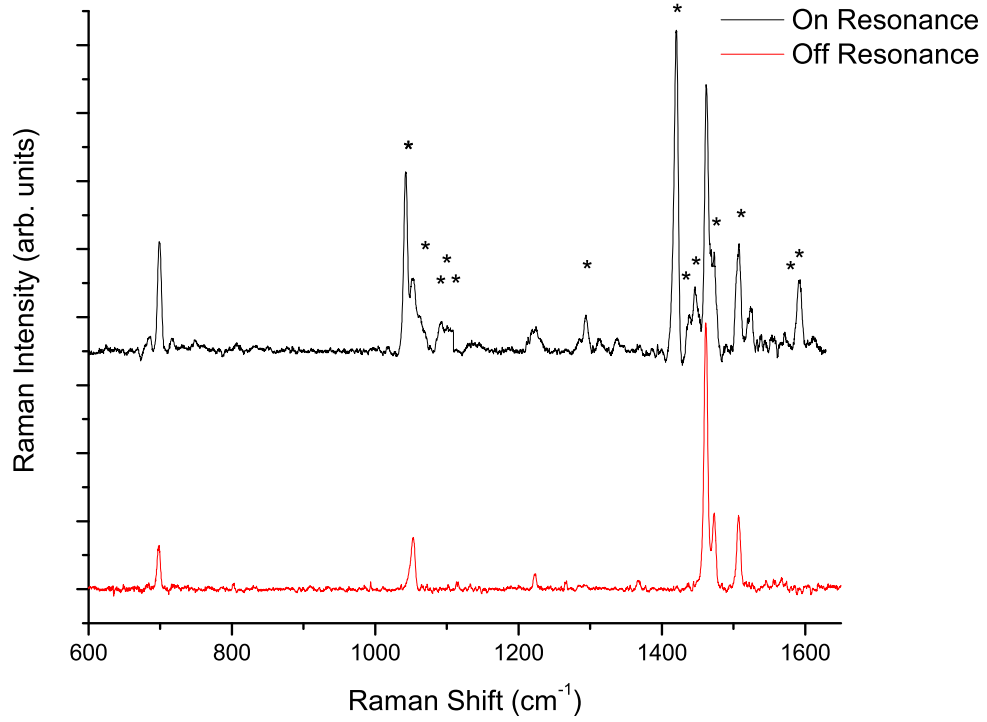


Figure 3.6: Raman spectra of α -hexathiophene on resonance, $\lambda_{exc}=599.43$ nm (2.0683 eV), and off resonance, $\lambda_{exc}=602$ nm (2.059 eV). The background luminescence as well as all instrumental effects have been subtracted out of the original spectra. All resonant vibrational modes are marked with asterisks.

quencies in the off-resonance spectra, these resonant modes do not correspond directly to other modes predicted by Esposti, *et al.* [55, 57] or by Shubin Liu at UNC. However, not all of the predicted modes from the theory have been observed. Therefore, it is conceivable that some of the modes that appear in my work correspond to vibrational modes predicted at incorrect frequencies. Additional improvements of the force fields used in the theory (including a coupling to electronic transitions at 2.066 eV and 2.068 eV) would presumably improve the predictions and, one hopes, lead to a better correspondence.

Table 3.4: Additional intramolecular Raman modes observed in this work. The spectra were collected with $\lambda_{exc}=599.43$ nm (2.0683 eV). The vibrational modes listed below marked with a \ddagger were previously listed in Tables 3.2 and 3.3. All other peaks have never been experimentally observed or theoretically predicted in the literature. The energy values listed below correspond to peaks marked with asterisks in Figure 3.6.

Frequency (cm ⁻¹)			
1592 \ddagger	1417	1063 \ddagger	296
1587 \ddagger	1293.5	390.5 \ddagger	277
1522	1284	365 \ddagger	269
1468.5	1116	343	250
1446	1103	327	239
1420.5	1091 \ddagger	318	209 \ddagger

Table 3.5: Intermolecular resonant Raman modes of α -hexathiophene observed experimentally. The spectra were collected with $\lambda_{exc}=599.43$ nm (2.0683 eV). Experimentally, because of the elastically scattered (Rayleigh scattered) photons, it is unfeasible to observe peaks below approximately 40 cm⁻¹. The vibrational modes listed below marked with a \ddagger were previously listed in Tables 3.2 and 3.3. All other peaks have never been experimentally observed or theoretically predicted in the literature.

Frequency (cm ⁻¹)	
174.5	96 \ddagger
145 \ddagger	66
121	50
111	

3.4.1 Results

In order to learn more about (and possibly identify) the peaks labeled with asterisks in Figure 3.6, it is important to understand the dependence of the intensity of the peak on incident excitation energy. Unfortunately, in typical Raman experiments the absolute intensity (or area) of an individual peak is an unreliable and highly variable quantity because it is closely tied to experimental conditions,

such as focus, CCD efficiency, accumulation time of the scan, etc., that are not intrinsic properties of the material. In order to resolve this problem, it is possible to compare the ratio of two peaks within a single scan to the corresponding ratio among many scans. This procedure normalizes for different experimental factors while preserving intrinsic information about changes between different vibrational modes. The ratio of resonant peak intensity to nonresonant peak intensity is plotted in Figure 3.7.

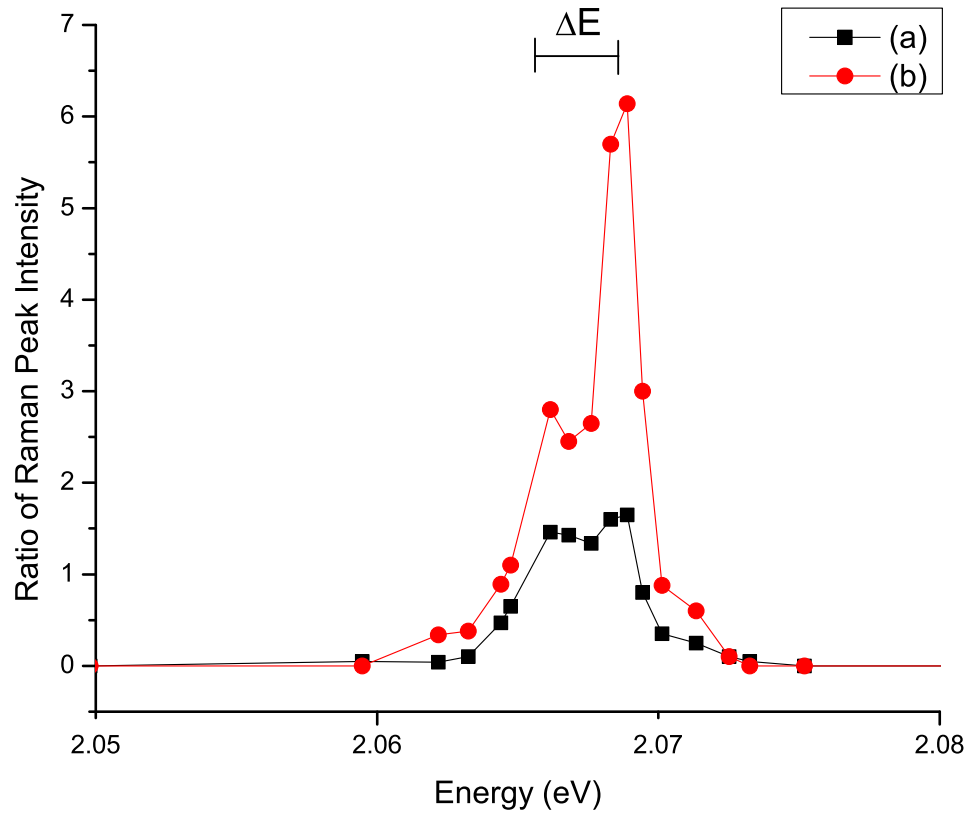


Figure 3.7: (a) Ratio of the intensity of the 1422 cm^{-1} resonant mode to the 1463 cm^{-1} nonresonant mode vs. excitation energy. (b) Ratio of the intensity of the 1045 cm^{-1} resonant mode to the 1052 cm^{-1} nonresonant mode vs. excitation energy. The peaks were fit with Voigt lineshapes in a least-squares routine.

The excitation profiles in Figure 3.7 clearly have two maxima, suggesting the

existence of two excitations. All of the excitation profiles associated with the resonant Raman lines identified in Figure 3.6 with asterisks have the same two maxima, at excitation energies of 2.066 eV and 2.068 eV, with a full width at half maximum (FWHM) of 2 meV for each peak. Thus, all the resonant Raman modes must involve the same electronic state. The splitting, $\Delta E = 0.002$ eV between the two peaks, is 16 cm^{-1} when expressed in wavenumber units.

3.4.2 Frenkel Excitons

Both the small width of these resonances and their proximity in energy to the band edge support the identification of the resonance being the result of a Frenkel exciton. Frenkel excitons are closely bound electron-hole pairs and are the primary photoexcitations of molecular crystals. Previous researchers have identified the lowest-energy singlet Frenkel exciton in a single crystal of α -hexathiophene by photoabsorption spectroscopy at 2.3 eV [46], but this $S1$ exciton has A_u symmetry. Both the molecule α -hexathiophene and its crystal are centrosymmetric because of their inversion points. Therefore, only modes with gerade-type symmetry can be Raman active. As stated in Section 2.2.4, the vibrational mode and the electronic excitation it couples to in a resonance situation must have the same symmetry. The difference in energy and the symmetry of the mode to which the electronic excitations couple indicate that the excitations I observed are different from the one Frolov, *et al.* [46] reported. Therefore, there must be other, lower-energy electronic transitions in the single crystal of α -hexathiophene with gerade-type symmetry that no other experiment has observed.

The fact that the transitions are lower in energy than the previously identified exciton suggests that trapped Frenkel excitons cause the resonances I observed. The two different peaks in the intensity profile could correspond to the excitation of two different trapped excitons, with slightly different binding energies. Since there is only 2 meV between the two excitations, the binding locations must be very similar. One possible example of similar but slightly different binding lo-

cations would be if excitons were localized on different carbons on an individual α -hexathiophene molecule. The difference in energy between the binding locations would then be the result of the different electronic configurations around the α - and β -carbons in an individual thiol ring. Another possibility would be excitons localized on an inner or outer ring of an individual α -hexathiophene molecule. Again, these locations have slightly different electron densities. Therefore they would represent different environments for the trapped Frenkel exciton, and thus, different binding energies.

Alternatively, the resonances may involve a triplet state of the $S1$ Frenkel exciton reported by Frolov, *et al.* [46]. A triplet exciton, by definition, is of opposite parity from the associated singlet state. Therefore, it would have A_g symmetry which is an allowed coupling to the observed Raman modes. Also, in the triplet symmetry state, the exciton would have lower energy than the previously-measured singlet state. Typical singlet-triplet energy splittings, ΔE_{S-T} , are on the order of 0.5 eV for organic molecules [1]. If the resonances observed here are from the triplet state of the exciton observed by Frolov, *et al.*, then $\Delta E_{S-T}=0.23$ eV, the correct order of magnitude as compared to other organic materials. Also, typical Davidov splitting energies ΔE_D for triplet excitons are on the order of 10 cm^{-1} , while ΔE_D for singlet excitons generally range from 100 to 1000 cm^{-1} [1]. The ΔE_D measured for the two unknown excitations in α -hexathiophene, as previously mentioned in Section 3.4.1, is 16 cm^{-1} . This would suggest that the splitting between the two electronic excitations could be Davidov split states of a triplet exciton. At first, the possibility of a triplet state may strike the reader as impossible since it would represent a forbidden optical transition from ground state of the material, but the possibility of a triplet as an intermediate state is allowed, although not very probable, due to spin-orbit coupling. The small matrix element for this transition is offset by the fact that it is only observed in resonance conditions when the denominator of the cross-section for scattering reaches a near singularity. With these very specific conditions, even typically

forbidden transitions can be measured.

3.4.3 Temperature Dependence of Resonances

In order to investigate the electronic excitations further, I varied the temperature of the sample and repeated the resonance experiment. For each temperature measured, I plotted the ratio of a resonant peak intensity to a non-resonant peak intensity versus energy, as shown in Figure 3.7. For simplicity, the figure displays the plot of only one ratio (that of the intensity of the 1045 cm⁻¹ resonant mode to the 1052 cm⁻¹ nonresonant mode), and each trace in the resulting figure represents the experiment at a different temperature. All of the ratios for other resonant modes follow the same trends depicted in Figure 3.8.

The most striking feature of Figure 3.8 is that the resonance profiles (absolute ratios) decrease with increasing temperature. In fact, by 55 K, the resonance is just barely visible above the noise of the spectrum. Clearly, something is quenching the coupling of the vibrational modes to the Frenkel exciton above 55 K.

As discussed in Section 2.2.4, a resonant Raman interaction occurs when the incident or scattered photon's energy approaches the energy of an electronic transition in the material. Equation (2.13) states the probability of Raman scattering by a single photon. To find the full differential scattering cross section, equation (2.13) must include a summation over the initial state of the crystal and be multiplied by a function of ω .

$$\begin{aligned} \frac{\partial^2 \sigma}{\partial \Omega \partial \omega} = F(\omega) \sum_0 \left| \sum_{n,n'} \frac{\langle i | \mathcal{H}_{e-R}(\omega_s) | n' \rangle \langle n' | \mathcal{H}_{e-ion}(\omega_o) | n \rangle \langle n | \mathcal{H}_{e-R}(\omega_i) | i \rangle}{[\hbar\omega_i - (E_n - E_i) - i\Gamma_n][\hbar\omega_s - (E_{n'} - E_i) - i\Gamma_{n'}]} \right|^2 \dots \\ \dots \times \delta[\hbar\omega_i - \hbar\omega_o - \hbar\omega_s] \end{aligned} \quad (3.1)$$

In equation (3.1) one can see only two locations that temperature can affect

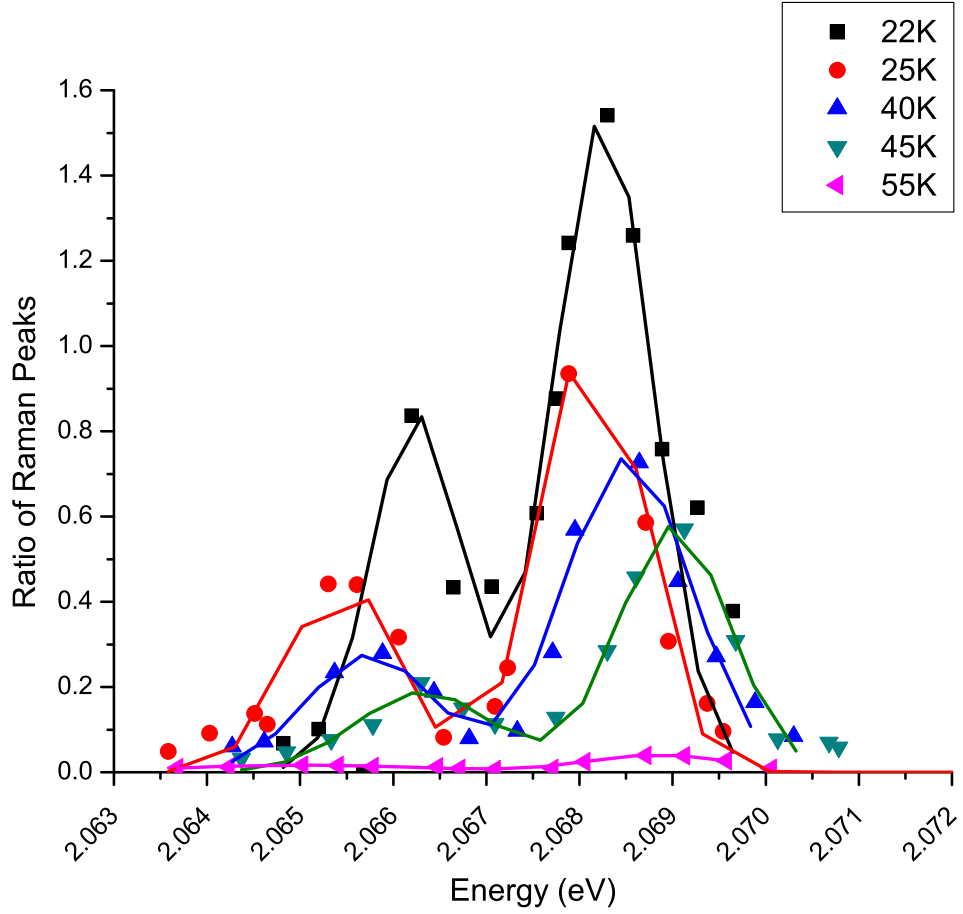


Figure 3.8: Temperature dependence of the resonance profile for α -hexathiophene. The temperatures range from 22 K to 55 K.

the scattering probability. One is in the sum over all possible initial states which includes a typical Boltzman distribution:

$$n = \frac{1}{e^{\frac{\hbar\omega}{k_B T}} - 1} \quad (3.2)$$

Although the phonon distribution in the initial state will change with temperature, this distribution will not cause the quenching of the entire resonance with temperature as seen in the experiment. As T increases, n approaches infinity, as expected - at higher temperatures there are more phonons present in the ground

state of the system. This means simply that a warmer material has a ground state that includes increasingly more vibrational excited states but this does not affect the possible intermediate virtual states involved in the resonance coupling. Since this does not affect the excited electronic states, this temperature effect cannot cause the observed quenching.

The only other location that temperature appears in equation (3.1) is in each denominator factor. Along with the energy of the phonon and the energy of the intermediate state, there is the $i\Gamma_n$ term, or width, of each intermediate state $|n\rangle$. This width is inversely related to the lifetime of the state (because of the standard quantum mechanical uncertainty principle) and is temperature dependent. As the temperature of the sample increases, the width of the state also increases due to thermal broadening from additional phonons. Mathematically, this increasing width prevents the denominator in equation (3.1) from approaching zero, thereby quenching the resonance. Physically, the wider the intermediate state, the less likely it is for a single incident or scattered photon to exactly equal the state's energy which decreases the probability of a resonance.

Thus, a measurement of the resonance quenching temperature is a direct link to the lifetime of the excited state (Frenkel exciton) involved in the resonance. If, as postulated in Section 3.4.2, the excited state involved in the resonance is a triplet exciton, the quenching energy is a direct link to the binding energy of the electron-hole pair in that exciton. On the other hand, if the excited states are bound singlet excitons, this quenching energy is a direct link to the binding energy of the traps. The energy of quenching, that occurs at temperature T is approximately $k_B T$, so the threshold of 55 K is only approximately 4.7 meV. Typical binding energies for Frenkel excitons are more on the order of 1 eV. They can and do exist in some materials at room temperature (where $k_B T \approx 0.025$ eV). This may imply that the bound exciton model hypothesis better fits the data or that the measured triplet excitons are in fact in an excited state and therefore have a lower binding energy.

3.5 Conclusion

I measured the Raman spectrum of α -hexathiophene at multiple temperatures and with multiple excitation wavelengths. The resonant Raman spectra have permitted the identification of electronic transitions not previously measured that couple strongly to vibrational modes. I have tentatively identified these electronic transitions as either bound singlet Frenkel excitons or a free triplet Frenkel exciton state. Plotting the resonant interaction versus temperature demonstrates a quenching point of the resonance at 55 K which is a direct link to either the binding energy of the triplet exciton or the binding energy of the traps of the single exciton.

Chapter 4

Optical Characterization of Rubrene and Tetracene

I compare the Raman spectra for single crystals of rubrene and tetracene to the calculated spectra for the isolated molecules. The Raman measurements I present here are of the bulk properties of the material and confirm that the vapor growth process yields very pure, unstrained rubrene crystals. They indicate that rubrene, unlike many other oligoacenes, has very weak intermolecular coupling and no observed intermolecular Raman vibrational modes. I discuss the apparent conflict between the high mobility and the weak π -electron overlap in this material. The temperature dependent photoluminescence spectra of rubrene single crystals both agrees with and contradicts other researchers' work available in the literature, while the change in PL with different photoexcitation energy is unremarkable.

4.1 Raman Measurements

4.1.1 Rubrene and Tetracene Crystals

Rubrene is a relatively small aromatic hydrocarbon consisting of a backbone of four fused benzene rings (tetracene) with four substituted phenyl groups (two

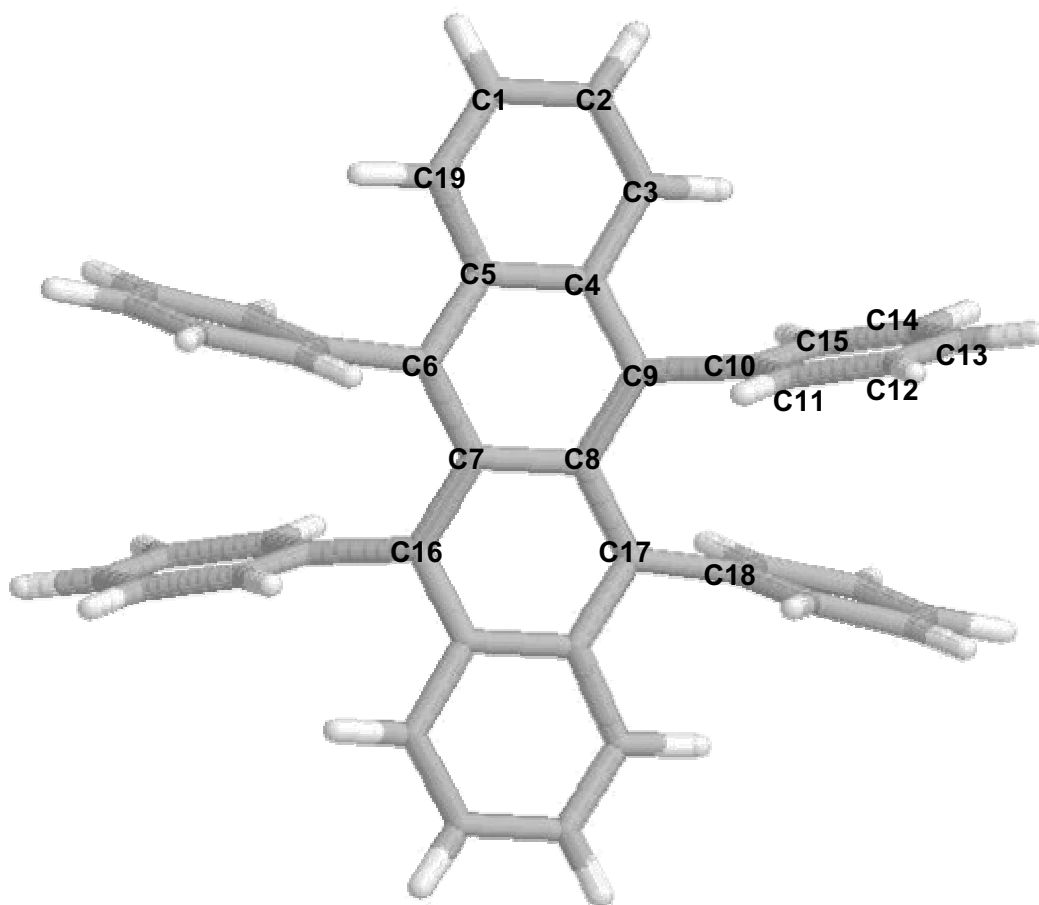


Figure 4.1: Rubrene ($C_{42}H_{28}$) molecule. The labels on the carbon atoms are in reference to Table 4.1.

on each internal ring) as shown in Figure 4.1. Steric hindrance dictates that the substituted phenyl groups rotate out of the plane of the tetracene backbone.

Christian Kloc grew the single crystals used in these measurements at Lucent Technologies by horizontal physical vapor transport in a flow of argon gas starting with rubrene powder acquired from Aldrich. Other publications describe the details of this growth process for rubrene [148] and for similar materials [147]. To change the morphology of the growing crystals and to get thick bulk crystallites more suitable for this present study, some previously-sublimed rubrene crystals subsequently served as the starting point for a typical vacuum-sealed ampoule growth. The molecule crystallizes in an orthorhombic structure and has D_{2h}^{18} point

Table 4.1: Comparison of experimental and theoretical geometrical structures of rubrene and tetracene molecules. Refer to the atomic labeling scheme in Figures 4.1 and 4.3.

	Rubrene		Tetracene	
	Experiment ^a	Theory	Experiment ^b	Theory
Distances				
C1-C2	1.442 Å	1.408 Å	1.431 Å	1.420 Å
C2-C3	1.366 Å	1.351 Å	1.367 Å	1.365 Å
C3-C4	1.439 Å	1.433 Å	1.434 Å	1.427 Å
C4-C5	1.466 Å	1.440 Å	1.452 Å	1.452 Å
C7-C8	1.474 Å	1.464 Å	1.452 Å	1.455 Å
C8-C9	1.431 Å	1.418 Å	1.410 Å	1.395 Å
C4-C9	1.409 Å	1.397 Å	1.393 Å	1.391 Å
C9-C10	1.503 Å	1.506 Å	N/A	N/A
C10-C11	1.402 Å	1.385 Å	N/A	N/A
C11-C12	1.395 Å	1.386 Å	N/A	N/A
Angles				
C3-C4-C9	121.8°	122.4°	122.3°	122.3°
C4-C9-C10	116.0°	115.6°	N/A	N/A
C8-C9-C10	122.9°	123.1°	N/A	N/A
C9-C8-C17	122.2°	122.3°	N/A	N/A
C10-C9-C17-C18	29.4°	25.1°	N/A	N/A

^a See reference [151]

^b See reference [152]

group symmetry [123] with four molecules per unit cell. The lattice constants for the orthorhombic unit cell are $|\vec{a}| = 26.901$ Å, $|\vec{b}| = 7.187$ Å, and $|\vec{c}| = 14.430$ Å. Figure 4.2 shows the molecular stacking in the crystal. Most crystallites are thin or thick platelets, millimeters in lateral dimension. The face of the crystallites

is the (100) plane. The consensus from the literature is that the crystals have a room-temperature band gap of approximately 2.21 eV [132].

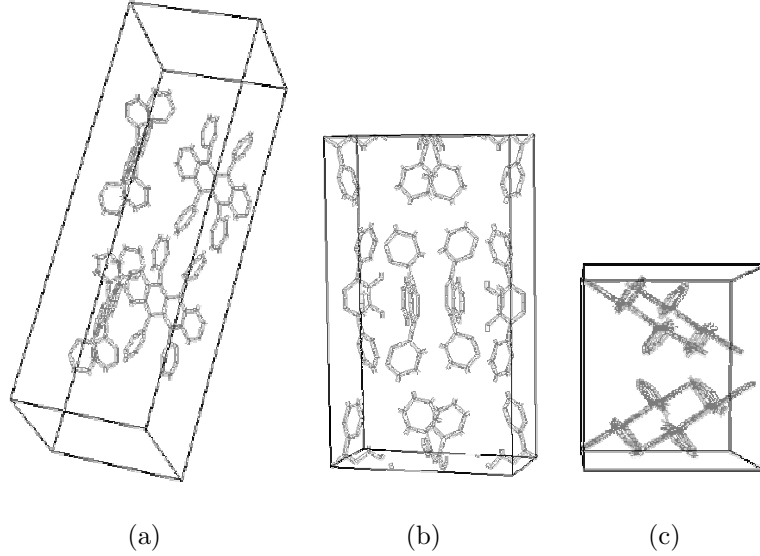


Figure 4.2: Three views of the packing in rubrene single crystals. (a) and (c) show the orientation of molecules with respect to each other while (b) is the primitive unit cell. The figures are based on x-ray data of the molecular orientation.

Christian Kloc also grew the tetracene single crystals at Lucent Technologies, in a similar horizontal vapor transport set-up. As tetracene makes up the backbone of the rubrene molecule, it is an ideal simpler system to use in understanding the properties of the more complicated rubrene molecule. Tetracene crystallizes in a triclinic structure and has C_i point group symmetry with two molecules in the unit cell. The lattice constants for the triclinic unit cell are: $|\vec{a}| = 7.98 \text{ \AA}$, $|\vec{b}| = 6.14 \text{ \AA}$, and $|\vec{c}| = 13.57 \text{ \AA}$ [105].

4.1.2 Experimental Conditions

I mounted multiple crystallites from the same growth batch at the same time for the initial experiment, paying no deliberate attention to the orientation of the crystallites. Any polarization effects will therefore average over the entire group of crystals which will affect analysis of the data. Studying multiple crystals

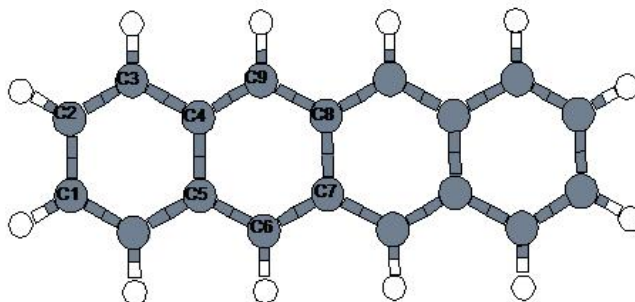


Figure 4.3: Tetracene ($C_{18}H_{12}$) Molecule: The labels on the carbon atoms are in reference to Table 4.1.

also allowed me to investigate the consistency of crystals produced in a single growth run. I selected the largest, nearly three-dimensional crystallites from multiple growth runs in order to gain access to different crystal faces, and thus observe vibrational modes with different symmetries. As I previously mentioned, rubrene highly favors creating a peroxide layer in the presence of light and oxygen [136]. I made no attempt to keep the crystals dry or in the dark, so the room-temperature, ambient-pressure spectra I present here are of both the underlying bulk rubrene crystal and the surface peroxide layer. It is important to remember during the subsequent discussion that the Raman data are of the bulk material, while other interesting attributes of rubrene’s high FET mobility are possibly from surface channel conduction.

I recorded Raman spectra using a Dilor XY triple spectrometer in a backscattering configuration and a charge-coupled device (CCD) cooled with LN_2 . The

resolution of the spectrometer is 1 cm^{-1} . Using an Air Products closed-cycle He refrigerator in a cryogenic chamber pumped down to approximately 10^{-6} Torr with a diffusion pump vacuum system, I cooled the crystals to 20 K. I pumped a Spectra Physics 375B dye laser with Kiton Red dye with a Spectra Physics 2017 Ar⁺ laser, yielding an output energy that is continuously tunable from 608 to 711 nm. I chose an excitation wavelength of 653.55 nm (1.897 eV) in the experiments to minimize the photoluminescence from the sample in order to measure the weaker Raman effect. My spectral windows ranged from approximately 35 cm^{-1} to 1600 cm^{-1} , a range that should include both intermolecular and intramolecular vibrations. After subtracting the background, I fit all peaks using Lorentzian lineshapes with a least-squares algorithm.

4.1.3 Computer Simulations

My collaborator, Shubin Liu, simulated the Raman spectra for isolated molecules using GAUSSIAN 03 [38]. He used the Hartree-Fock method for the structural optimization and the density functional theory (DFT) B3LYP method to calculate the Raman frequencies. Both simulations ran with the 6-31G* basis set. He repeated the calculation with GAUSSIAN 03 with both the structural optimization and the frequency simulation performed with the DFT B3LYP method and the 6-31G9(d) basis set. All calculations ran on an SGI Origin 3800 with 64 CPUs and 128 GB memory running the IRIX 6.5 OS.

4.1.4 Rubrene Single Crystal Raman Results

Overall, I can make a few statements about rubrene based on this Raman investigation. First, the vapor deposition growth process produces very homogeneous crystals within each run. I recorded Raman spectra for a number of crystallites, but made no attempt to mount the crystals in specific orientations. In Raman spectroscopy, the cross section for scattering depends in part on the

scalar product of the incident light polarization, the Raman tensor for a particular mode, and the polarization of the scattered light:

$$\frac{\partial \sigma_s}{\partial \Omega} \propto |\hat{\epsilon}_s \cdot \tilde{R} \cdot \hat{\epsilon}_i|^2 \quad (4.1)$$

In equation (4.1), $\partial \sigma_s / \partial \Omega$ is the differential scattering cross-section; $\hat{\epsilon}_s$ and $\hat{\epsilon}_i$ are the polarizations of the scattered and incident light, respectively; and \tilde{R} is the Raman tensor for the system. The geometric arrangement of the experimental set up, the polarization of the incident and scattered light, and the symmetry of the crystal are therefore important factors in the overall scattering cross section. As previously mentioned, rubrene crystallizes in the D_{2h}^{18} point group, which allows vibrations of eight symmetry types: A_g , A_u , B_{1g} , B_{1u} , B_{2g} , B_{2u} , B_{3g} , B_{3u} . This point group has a center of inversion, so only the gerade modes are Raman active. The Raman tensors for these allowed modes are:

$$\begin{aligned} A_g &= \begin{pmatrix} a & 0 & 0 \\ 0 & b & 0 \\ 0 & 0 & c \end{pmatrix} & B_{1g} &= \begin{pmatrix} 0 & d & 0 \\ d & 0 & 0 \\ 0 & 0 & 0 \end{pmatrix} \\ B_{2g} &= \begin{pmatrix} 0 & 0 & e \\ 0 & 0 & 0 \\ e & 0 & 0 \end{pmatrix} & B_{3g} &= \begin{pmatrix} 0 & 0 & 0 \\ 0 & 0 & f \\ 0 & f & 0 \end{pmatrix} \end{aligned} \quad (4.2)$$

The rubrene crystal cleaves along the (100) face, so the bc plane is available in many different orientations in this experiment. As Table 4.2 enumerates, in a backscattering configuration, one can observe only A_g and B_{3g} modes. Depending on the relative orientation of the crystal axes in the face of the crystallites and the incident polarization, the relative intensities of the A_g and B_{3g} modes should change. I collected Raman spectra from ten different platelet-like crystallites (as well as from multiple locations on some of the larger crystallites). All of the

spectra are substantially the same, other than small changes in the relative intensities of individual peaks. This is a strong indication that the crystal-growing process is creating only very pure, unstrained rubrene crystals. Figure 4.4 is a representative Raman spectrum measured from the different crystallites.

Table 4.2: Allowed Raman Modes for Backscattering Geometry: The incident light polarization must be $\hat{\epsilon}_i = (x \ y \ 0)$ while the scattered light polarization must be $\hat{\epsilon}_s = (x' \ y' \ 0)$ where x, y, x' , and y' are components of the polarization in the plane of the crystal face.

Symmetry Type	$ \hat{\epsilon}_s \cdot \tilde{R} \cdot \hat{\epsilon}_i $
A_g	$bx x' + cy y'$
B_{1g}	0
B_{2g}	0
B_{3g}	$f(xx' + yy')$

4.1.5 Comparison to Theory

One gains more information about the individual modes from the spectra, especially when comparing them to calculations of the Raman modes of both isolated rubrene and tetracene molecules. The positions of the peaks in the calculated spectrum for the isolated rubrene molecule, when plotted against the positions from the experimentally-measured spectrum from the rubrene single crystal, lie along a least-squares fit line with a slope of 1.05 and a correlation coefficient of 0.9998 (see Figure 4.5). Table 4.1 lists the atomic positions and the bond angles from the geometric minimization of the rubrene molecule. The initial input for the geometric minimizations was a set of X-ray measurements taken by Theo Siegrist at Lucent Technologies (where the crystals were grown). The predicted positions from the calculation show that their structure agrees with that previously published for rubrene [151] and tetracene [152]. As mentioned previously, Shubin Liu performed two calculation runs with GAUSSIAN 03 on the isolated rubrene molecule. The second calculation required much more

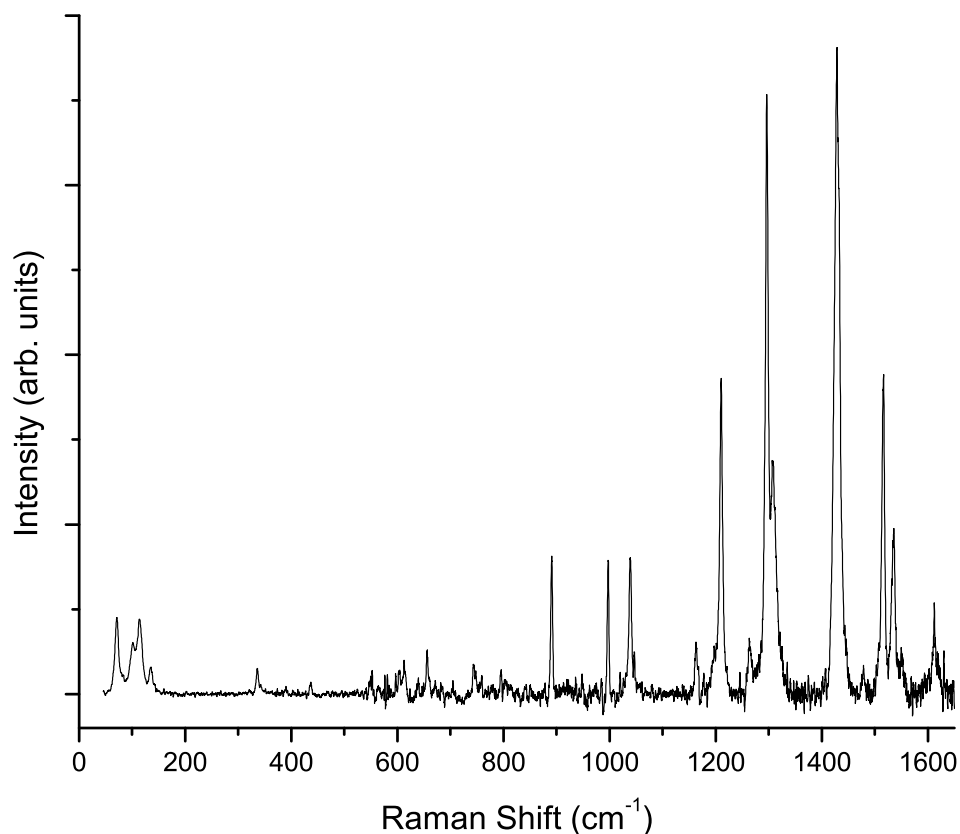


Figure 4.4: Representative room temperature Raman spectrum of rubrene single crystals collected with an excitation energy of 653.55 nm (1.897 eV).

CPU time, but there is virtually no difference between the two simulated spectra for almost every higher-energy mode. For the low-energy modes, only small differences appeared: the lowest-energy mode at about 21 cm⁻¹ upshifted 13%, the other low-energy modes upshifted 3% or less, and the rest of the intramolecular modes changed less than 1% with the higher-level basis set calculation.

There is an extremely close agreement between the calculated isolated-molecule Raman spectrum and the experimentally-observed single crystal spectrum. All but five of the twenty-five highest-predicted-intensity peaks in the calculated spectra correspond to experimentally-measured modes on the platelet crystals. The backscattering geometry of the experimental set-up, with the platelet crys-

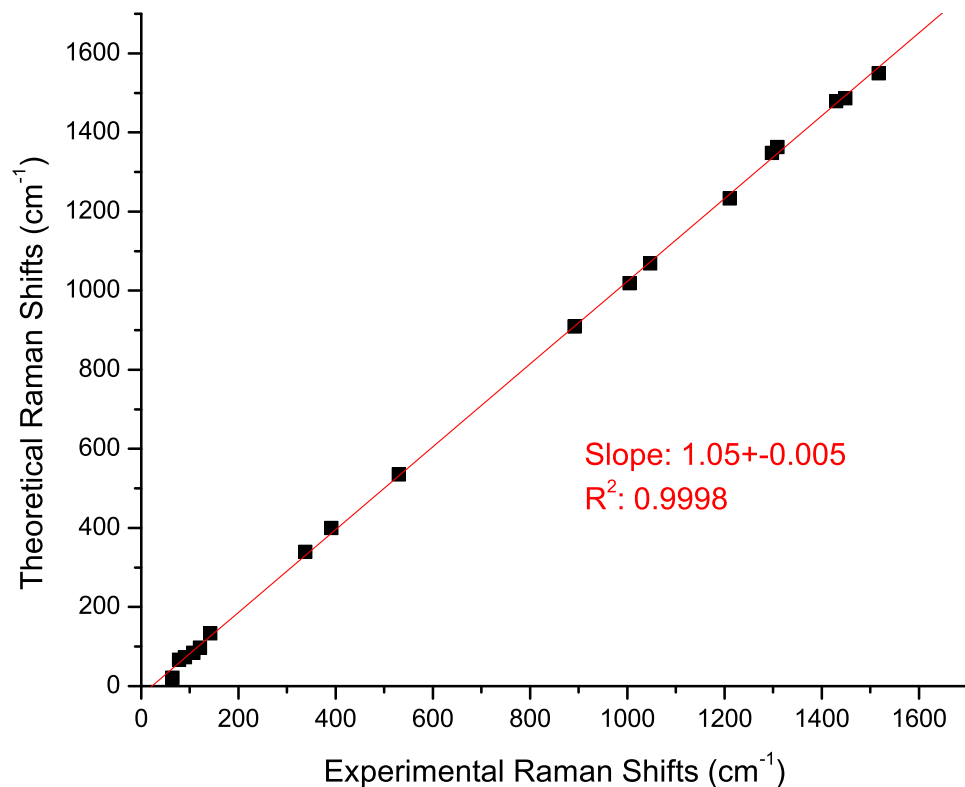


Figure 4.5: Experimentally-measured single crystal vs. theoretically-predicted isolated molecule peak positions for rubrene. Experimental data were collected with an excitation energy of 653.55 nm (1.897 eV)

tals, allows only observation of the A_g and B_{3g} symmetries, so the peaks in the calculated spectrum not observed in the experimental spectrum must be of a different symmetry type (B_{1g} or B_{2g}). Larger, three-dimensional crystallites allowed access to different crystal faces. I observed the remaining predicted modes in measurements of these different crystal faces. No modes not predicted by the theory appeared in these additional scans. Overall, for modes of frequency greater than 300 cm⁻¹, the calculated peak energies are within 2% of the experimentally observed energies after the typical scaling factor [153] of 0.96 has been applied to the theoretical frequencies.

The lower-energy modes are farther from experimental values for two main

reasons. Mathematically, small errors at low frequency simply appear large when given as percentages. Errors as large as 20% correspond to shifts of only ten to twenty wavenumbers if the peak position is 200 cm^{-1} or less. Physically, one would also expect crystal forces (van der Waals bonding between molecules) to affect lower-energy modes more than vibrational modes with higher energy. As the simulation is for a single molecule that cannot take into account intermolecular interactions, rather than the measured single crystal, it is not surprising that the theory and experiment diverge more in the low-energy range. For each CCD window, I scaled the peaks in the experimental spectrum so that the tallest experimental peak matched the intensity of the corresponding theoretical peak. This scaling technique resulted in intensities that matched within a factor of two between the experimental and theoretical spectra.

The isolated rubrene molecule has C_{2h} point group symmetry and also has a point of inversion. The possible Raman-active modes for the molecule are therefore of symmetries A_g or B_g only, compared with the four possible Raman mode symmetries in the single crystal (A_g , B_{1g} , B_{2g} , and B_{3g}). It is still possible, however, to use the theoretical calculations from the isolated molecule to identify the symmetries of the single crystal vibrational modes. A close inspection of Figures 4.1 and 4.2 reveals that part of a rubrene molecule lies along a mirror plane in the primitive unit cell. Therefore, a mode that was initially symmetric with respect to the axis of symmetry (A_g) in the isolated molecule would still have to be symmetric with respect to a mirror plane in the single crystal. This means that it is impossible for a mode predicted as A_g to become any B_g symmetry when the molecule crystallizes. A detailed group theory analysis of the molecule allows the calculation of the number of each symmetry mode once one knows the irreducible representation (see Table 4.3) and the character table (see Table 4.4) for the C_{2h} point group. The number of allowed modes of each symmetry for a particular symmetry group is:

$$a_i = (1/h) \sum_i (g_i \chi_i(\Gamma_i) \chi_a(\Gamma)) \quad (4.3)$$

where a_i is the number of modes of a particular symmetry, h is the number of symmetry operations for a particular class ($h = 8$ for D_{2h}^{18} point group symmetry) and g_i is the number of elements in each class (1 for the D_{2h}^{18} point group). $\chi_i(\Gamma_i)$ is the character from the irreducible representation (see Table 4.3) and $\chi_a(\Gamma)$ is the character of the symmetry class from the character table (see Table 4.4). From this group theory analysis one can predict 51 A_g , 51 B_g , 51 A_u and 51 B_u modes for rubrene, exactly the same distribution of modes from the theoretical simulations. The nearly one-to-one correspondence between peaks in the calculated and observed spectra, the close correlation in energy of these peaks, and symmetry considerations of the molecule and single crystal allow me tentatively to identify the symmetries of the single crystal Raman modes. Table 4.5 lists these modes.

Table 4.3: Irreducible Representation for the Isolated Rubrene Molecule

E	C ₂ (y)	i	σ_{xz}
210	-2	0	0

Table 4.4: Character Table for the C_{2h} Point Group

	E	C ₂	i	σ_h
A_g	1	1	1	1
B_g	1	-1	1	-1
A_u	1	1	-1	-1
B_u	1	-1	-1	1

Table 4.5: Peak positions for the measured and calculated Raman spectra of rubrene, including symmetry assignments from the theoretical calculations - B_g modes from the isolated molecule spectrum are B_{3g} modes in the single crystal spectrum for the platelet crystals and either B_{1g} or B_{2g} for the modes found on the other crystallite faces of the larger three-dimensional crystal.

Symmetry	Theory ^a	Experiment	Comparison
	Position (cm ⁻¹)	Position (cm ⁻¹)	% Difference
B_g	72.2	73.7	2%
B_g	80.3	85.7	6.3%
A_g	83.2	107.0	22.2%
B_g	96.5	120.3	19.8%
A_g	128.6	141.7	9.2%
A_g	205.3	204.4 ^b	0.4%
A_g	254.4	236.6 ^b	7.5%
A_g	326.4	342.0	4.6%
B_g	385.4	393 ^b	1.9%
B_g	467.7	470 ^b	0.5%
A_g	514.1	517 ^b	0.5%
B_g	575.3	613.7	6.2%
A_g	872.8	896.3	2.6%
A_g	977.7	1003.9	2.6%
A_g	1026.6	1046.0	1.9%
A_g	1183.9	1163.0	-1.8%
B_g	1251.1	1268.2	1.4%

Continued on the next page

^aAdditional peaks were calculated to be at 22.9 and 67.2 cm⁻¹ but this is outside the range of the measured spectrum

^bFrom 3D crystallite experiment

Table 4.5 cont.

Symmetry	Theory ^a	Experiment	Comparison
	Position (cm ⁻¹)	Position (cm ⁻¹)	% Difference
A _g	1295.1	1299.9	0.4%
A _g	1307.1	1310.9	0.3%
B _g	1330.5	1315.7	-1.1%
A _g	1420.8	1432.3	0.8%
B _g	1487.7	1519.9	2.1%
A _g	1530.4	1539.9	0.6%
A _g	1592.3	1616.8	1.5%

^aAdditional peaks were calculated to be at 22.9 and 67.2 cm⁻¹ but this is outside the range of the measured spectrum

4.1.6 Tetracene Single Crystal Spectrum

One can glean additional insights in the interpretation of the rubrene single crystal spectrum by comparing it to the Raman spectra from similar molecules, specifically tetracene and benzene. Rubrene comprises a tetracene backbone with four substituted benzene rings. These benzene rings do not disrupt the conjugation or bonding of the tetracene backbone. Therefore, one would expect great similarities between the vibrational modes of rubrene and tetracene, with the possible addition of lines from the benzene spectrum. As there is a lack of high-quality single crystal spectra of tetracene in the literature [106, 109], we have measured and calculated the Raman spectrum of tetracene for the purpose of comparing it with the Raman spectrum of rubrene. Figure 4.7 is the measured Raman spectrum for tetracene single crystals. The slope of the least-squares fit of the positions of the calculated and measured tetracene modes is 0.9994 with a correlation coefficient of 0.9997, as seen in Figure 4.6, showing once again how well the theory matches the experimental spectrum. The Raman spectrum

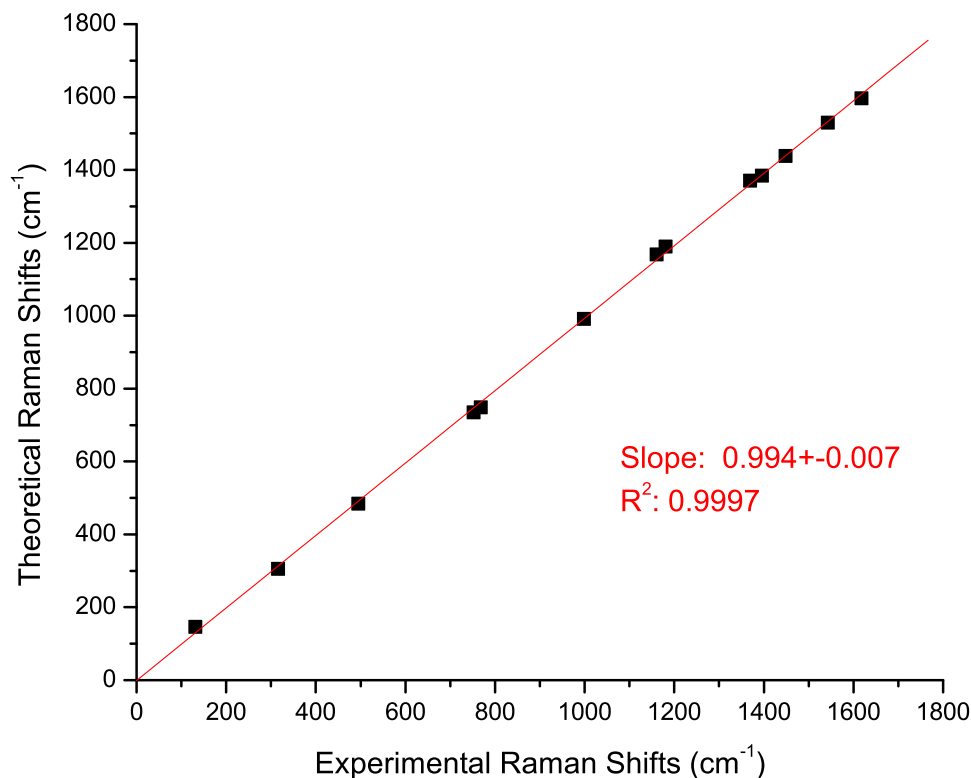


Figure 4.6: Experimentally-measured single crystal vs. theoretically-predicted isolated molecule peak positions for tetracene. Experimental data collected with an excitation energy of 653.55 nm (1.897 eV)

of benzene, on the other hand, is well established in the literature [154–156]. Therefore, I did not measure or perform calculations to predict its spectrum for this work. At first glance, rubrene, tetracene and benzene have surprisingly different Raman spectra.

Before comparing the tetracene and rubrene spectra, a short discussion of the tetracene spectrum is beneficial. The correspondence between the simulated isolated single-molecule spectrum and the measured single crystal spectrum is not nearly as close as that of rubrene. There are two important reasons for this. First, tetracene is a rigid, planar molecule that can pack very tightly. Tetracene crystallizes with triclinic C_i symmetry with two molecules in the unit

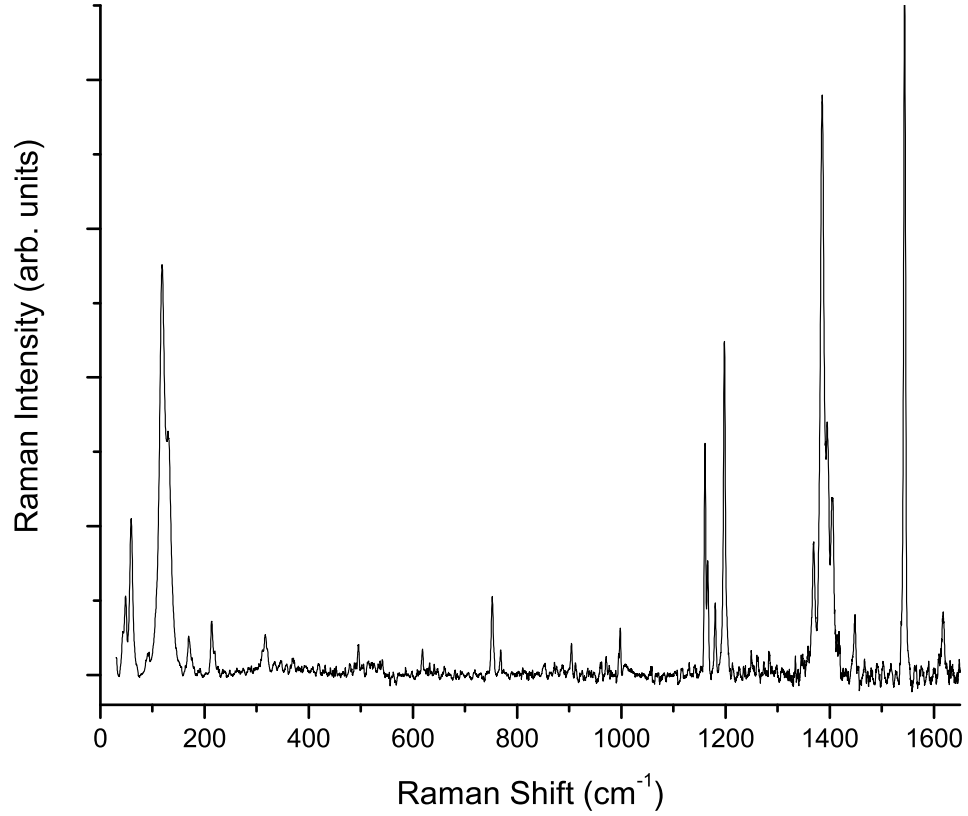


Figure 4.7: Room temperature Raman spectrum of tetracene single crystals collected with an excitation energy of 653.55 nm (1.897 eV).

cell. The lattice parameters are $|\vec{a}| = 7.98 \text{ \AA}$, $|\vec{b}| = 13.57 \text{ \AA}$, and $|\vec{c}| = 6.14 \text{ \AA}$ [105], while the lattice parameters of rubrene are $|\vec{a}| = 26.9 \text{ \AA}$, $|\vec{b}| = 14.43 \text{ \AA}$, and $|\vec{c}| = 7.19 \text{ \AA}$ [123,125]. The primitive unit cell of rubrene is more than four times as large as that of tetracene. While the rubrene molecule itself is larger than tetracene, it is mainly the differences in packing that cause the change in the size of the unit cell. The phenyl groups on the rubrene molecule prevent the close packing arrangement achieved by tetracene in the solid state. The molecules in a rubrene crystal are nearly three times farther from each other than are those in the tetracene crystal. For this reason, it is not surprising to find much stronger intermolecular interactions between tetracene molecules, and

hence a larger difference between the simulated isolated molecule spectrum and the measured single crystal spectrum.

These intermolecular interactions affect the crystal spectrum in two ways: by the presence of new, low-energy intermolecular vibrational modes and by the lifting of degeneracies of higher-energy intramolecular modes. A comparison of the two spectra demonstrate both of these intermolecular interactions. Although difficult to see in Figure 4.7, many of the Raman modes are actually doublets. The positions for all of the peaks are listed in Table 4.6. The splitting of peaks could be the result of crystal field splitting such as Davydov splitting, or the vibronic mixing of different molecular states. Either way, the doublets are caused by the crystallization of the molecule. An analysis of the energy split versus temperature is necessary to distinguish the exact cause of the observed doublets.

I believe that all the modes observed in tetracene below 200 cm^{-1} are, in fact, intermolecular vibrational modes, and therefore not predicted in the isolated molecule simulation. The tetracene crystal has two molecules in the unit cell; therefore, interactions in the solid state could, in principle, split all peaks into doublets. While it is not possible to resolve every doublet in the experimental data, all the frequencies (including all members of each pair) of the higher-energy modes are within 1.3% of a scaled predicted mode. Table 4.6 lists the correspondence between the experimentally-observed intramolecular modes and those predicted by the theoretical simulations. Every calculated mode with a scaled intensity above the noise of the experiments has a corresponding experimentally-observed mode, indicating the strong correlation between the theory and the experiment. Given this correspondence, one can use other information from the theoretical predictions to help interpret the experimental spectrum: specifically the symmetry assignments of the actual modes and the atomic motions they represent. Included in Table 4.6 are the symmetries of the modes from the theoretical predictions.

Table 4.6: Frequency of intramolecular modes for tetracene, both experimentally measured for the single crystal and calculated for the isolated molecule.

Symmetry	Theory Position (cm ⁻¹)	Experiment Position (cm ⁻¹)	Comparison % Difference
B _{1g}	146.0	130.7	11.7%
A _g	305.8	316.1	-3.3%
B _{3g}	484.8	495.0	-2.1%
A _g	735.2	752.2	-2.3%
B _{2g}	748.8	768.3	-2.5%
A _g	990.9	998.1	-0.7%
B _{3g}	1168.5	1160.5	0.7%
		1165.9	0.2%
A _g	1190.1	1180.2	0.8%
		1197.8	-0.6%
A _g	1370.6	1368.8	0.1%
		1386.0	-1.1%
A _g	1384.6	1395.6	-0.8%
A _g	1438.1	1403.5	-1.3%
		1448.1	-0.7%
A _g	1529.6	1543.0	-0.9%
		1544.7	-10%
B _{3g}	1596.9	1617.5	-1.3%

4.1.7 Comparison of Rubrene and Tetracene Spectra

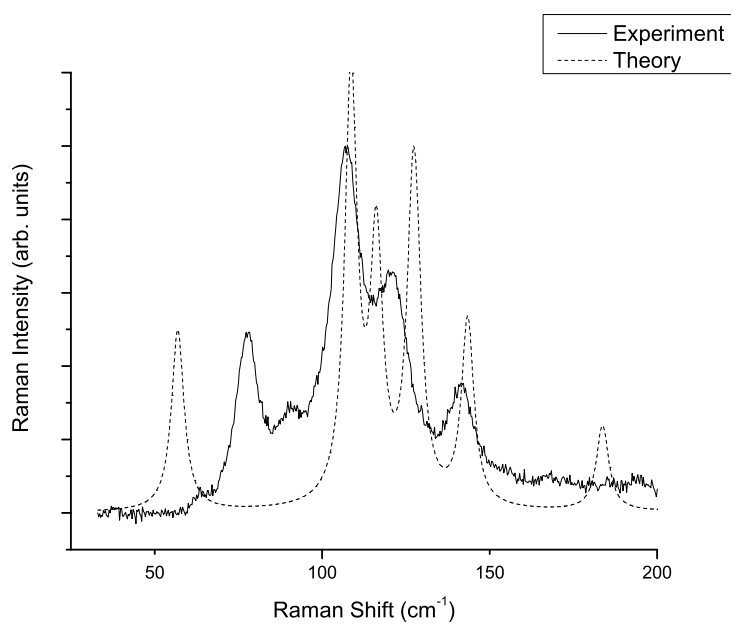
Since the rubrene molecule is just a derivative of the tetracene molecule, it should be possible to categorize some of the vibrational modes of rubrene as combinations of modes from the tetracene backbone and from individual benzene

ring modes. The Raman-active vibrational modes of benzene are well understood and characterized [154–156]. This experiment measured the crystal modes of tetracene. The theoretical calculations yield individual displacement vectors per atom per normal mode of vibration.

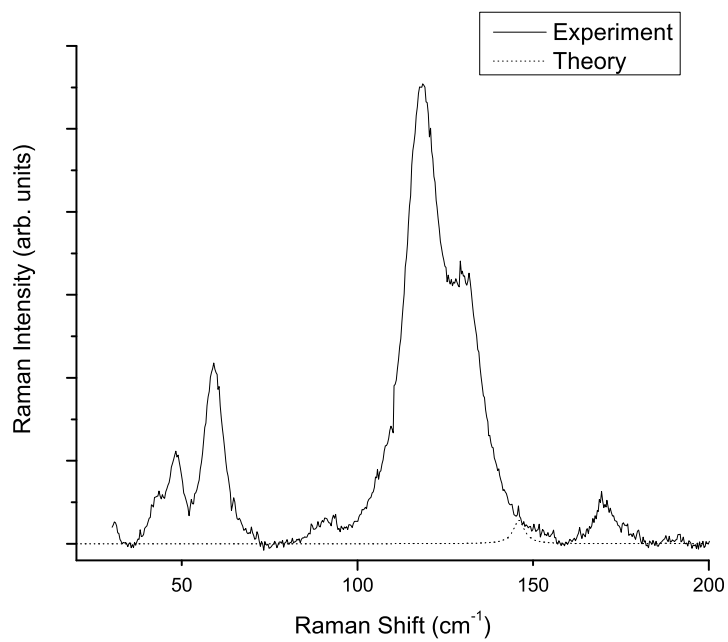
I converted these theoretical calculations for each vibrational mode into molecular animations viewable as individual movies at <http://www.physics.unc.edu/project/mcneil/MolecularAnimations/anim.php>.

Viewing these animations allows one to understand the motions involved in different vibrational modes and compare them with other spectra, like those of benzene and tetracene. For example: the rubrene mode at 83.2 cm^{-1} involves almost no motion of the atoms in the backbone and is simply a symmetric breathing of the atoms in the phenyl rings. Meanwhile the mode at 80.3 cm^{-1} involves the shearing of atoms in the backbone of the molecule only (parallel to the long axis of the molecule).

Finally, comparing the theoretical calculations of the isolated molecule with measured spectra from the single crystal indicates that the vibrational coupling between molecules in rubrene crystals is very small. In most molecular solids, Raman modes below about 150 cm^{-1} are almost always intermolecular modes. However, the calculated Raman spectrum for the isolated rubrene molecule predicts many low energy modes in this region and the one-to-one correspondence with the experimental spectrum indicates that the lowest-energy modes measured here are, in fact, all intramolecular. In stark contrast to this is the predicted spectrum for the isolated molecules of tetracene. In that instance the theory predicts that there are essentially no modes below 300 cm^{-1} , however, experiments do observe modes in this energy region. This contrast between the low-energy theoretical and experimental spectra for rubrene and tetracene is very evident in Figure 4.8.



(a)



(b)

Figure 4.8: Room temperature low-energy experimental data and theoretical predictions for (a) rubrene and (b) tetracene single crystals

4.1.8 Temperature Dependence of Rubrene Spectra

A very obvious difference between inter- and intramolecular modes lies in their temperature dependence. Temperature disproportionately affects intermolecular modes associated with vibrations of the atoms bound by the weaker van der Waals forces. In comparison, the stronger covalent bonds stretch much less in intramolecular vibrational modes because temperature changes cause changes in the lattice constants rather than molecule itself. In fact, when the rubrene crystallites are cooled from room temperature to 20 K, there is only a small upshift in the Raman signal (see Figure 4.9). These modes change by less than 3% (see Table 4.7), whereas lattice modes of other organic molecular crystals change more on the order of 5%. Recall the 7% change in some α -hexathiophene intermolecular modes from Figure 3.5 in Section 3.3. Between the weak temperature dependence and the strong correlation with the theory that cannot predict intermolecular modes, it seems that all the observed vibrational modes of rubrene are intramolecular in nature. This lack of strong intermolecular modes and the close correspondence between the isolated single molecule and the crystal indicate very weak coupling between molecules in the solid state of rubrene.

Table 4.7: Peak positions for rubrene intramolecular modes at 300 K and 20 K

Position (cm ⁻¹)	Position (cm ⁻¹)	% Difference
300 K	20 K	
73.7	75.6	2.5%
85.7	83.2	-2.9%
107.0	107.2	0.2%
120.3	123.5	2.7%
141.7	138.0	2.6%

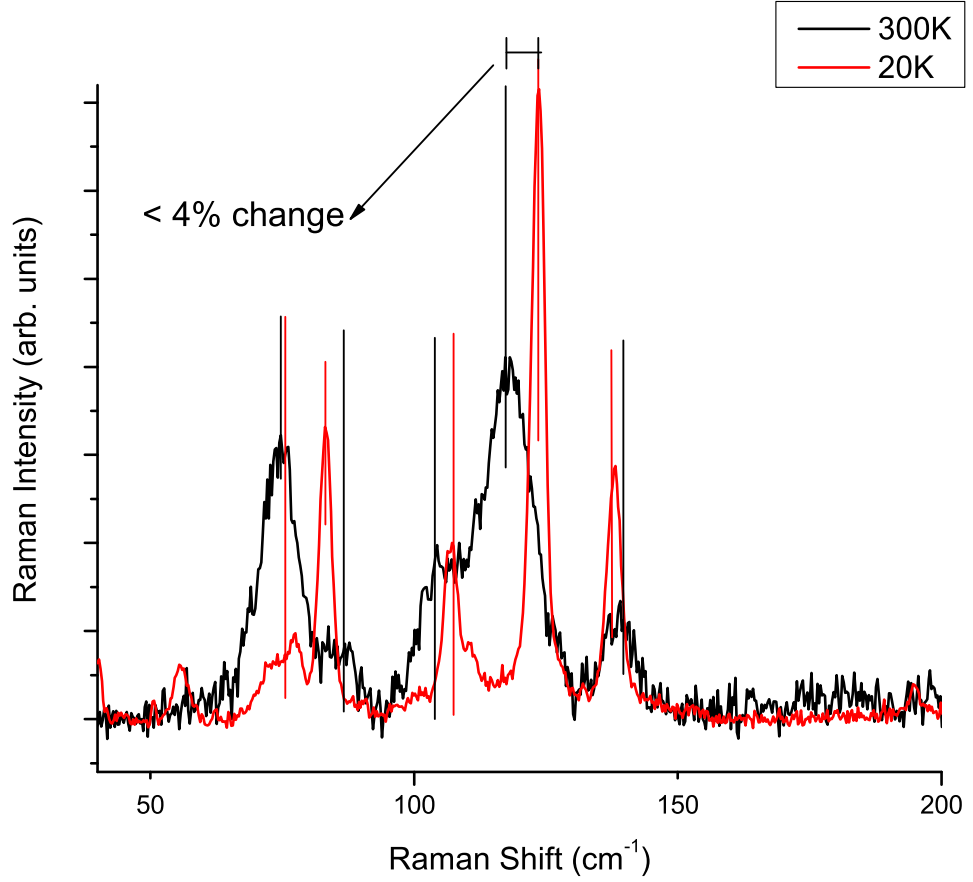


Figure 4.9: Low-frequency Raman spectrum of rubrene at 300K and 20K collected with an excitation energy of 653.55 nm (1.897 eV)

4.1.9 Intermolecular Coupling in Rubrene Single Crystals

The commonly held belief in the field of “plastic electronics” is that molecules should be chosen such that they have close packing arrangements to allow for strong π -electron overlap and that this strong π -electron overlap is necessary for high mobility. The results of the Raman measurements are in apparent conflict with this reasoning. However, the mobility does not depend only on π -electron overlap. The mobility in a material is actually:

$$\mu = \frac{e\tau}{m^*} \quad (4.4)$$

where τ is the mean time between collisions in a material, and m^* is the effective mass of the carriers in question (typically holes).

The dependence of the mobility on m^* follows the commonly held idea. The closer the packing of molecules, the broader the band of electronic states. Since m^* is proportional to the curvature of the band, the broader the band, the smaller m^* . Therefore, large overlap leads to smaller effective mass which, in turn, increases mobility. Conversely, smaller π -electron overlap increases m^* and therefore decreases mobility. Molecular crystals that have tight packing, and hence more overlap, tend to have a higher mobility. This trend is evident when comparing the rigid oligoacenes. As the number of phenyl rings increases, the density of the crystal increases. At the same time, the mobility increases, as Table 4.8 lists. The trend of increasing mobility with chain length is much clearer from the theoretical predictions. Experimental results do follow this pattern, but it is clear from an investigation of the literature that crystal preparation and purity are as important – if not more so – than the actual molecular composition in determining the mobility.

But m^* is not the only parameter that determines the mobility, τ is also important. Larger τ implies fewer scattering events or weak electron-phonon coupling so that times between collisions (or mean free paths) increase. The Raman data supports the probability of a large value of τ in rubrene because of the lack of measured intermolecular vibrations that can scatter carriers. This indicates that it is the ratio of τ/m^* that is crucial in determining mobility and the apparent conflict between the Raman results and molecule design objectives is not actually a problem.

Measurements of mobility in organic field-effect transistors have focused predominantly on lower-bandgap materials, for which it is easier to fabricate contacts. The high mobilities reported may be more a result of the small bandgap than of the large π -electron overlap. The measured mobilities to date are, in fact, only lower bounds for intrinsic reasons such as traps and defects. These can limit

the source-drain conductivity and result in a decreased transistor mobility compared to the bulk properties of the material. Additionally, difficulties in making high quality, low resistance contacts can lower the measured mobility of a device. Unfortunately, the size of the crystals is typically too small to allow for a four-contact device, so corrections cannot be made for the contact resistance. Other research groups have been able to fabricate four-probe single-crystal FETs and similarly find a high contact-corrected mobility of $8 \text{ cm}^2/\text{V-s}$ [133]. Regardless of the contacts, however, in FET structures the transport takes place in a very thin surface layer.

As previously stated, rubrene readily forms an endoperoxide, but this oxidation is limited to a very thin surface layer on a single crystal [137]. The Raman measurements discussed in Section 4.1.2 are from the bulk of the crystal. The energy used in this experiment (1.897 eV) is well below the band gap for the material so one can assume that the absorption coefficient is very small. Thus, only the depth of focus of the objective used in the experiment limits the scattering volume that the Raman signal is collected. For this experimental configuration, the depth of focus of the objective is on the order of one micron. Since the excitation energy used in these experiments allowed hundreds of unit cells to be probed, the Raman spectra I report here represent the bulk, intrinsic properties of rubrene crystals. This means that measurements of rubrene FETs may show a high mobility separate from the true intrinsic properties of the material.

Table 4.8: Densities and Mobilities of Oligoacenes

Crystal	Density (g/cm ³)	Exp'l Hole mobility (cm ² /V-s)	Th'l Hole mobility (cm ² /V-s)
Naphthalene	1.17 ^a	1 ^b	1.32 ^c
Anthracene	1.24 ^d	2.1 ^e	1.84 ^c
Tetracene	1.29 ^f	1.3 ^g	4.24 ^c
Pentacene	1.33 ^d	2.2 ^h	5.37 ^c
Rubrene	1.27	20 ⁱ	

^a S.C. Abrahams, J.M. Robertson, and J.G. White, *Acta Crystallographica* **2**, 233 (1949).

^b N. Karl, *Synthetic Metals* **133-134**, 649 (2003).

^c W.Q. Deng and W.A. Goddard, *Journal of Physical Chemistry B* **108**, 8614 (2004).

^d A. Mathieson, J. M. Robertson, and V.C. Sinclair, *Acta Crystallographica* **3**, 245 (1950).

^e E.A. Silin'sh and V. Capek, *Organic Molecular Crystals: Interaction, Localization, and Transport Phenomena* (AIP Press, New York, NY, 1994).

^f J. Trotter, *Acta Crystallographica* **15**, 289 (1950).

^g C. Goldmann, S. Haas, C. Krellner, K.P. Pernstich, D.J. Gundlach, and B. Batlogg, *Journal of Applied Physics* **96**, 2080 (2004).

^h J.M. Roberson, J. Kowalik, L. Tolbert, C. Kloc, R. Zeis, X. Chi, R.M. Fleming, and C. Wilkins, *Journal of the American Chemical Society* **127**, 3069 (2005).

ⁱ See reference [134]

4.2 Infrared Spectrum of Rubrene

As discussed in Section 2.3, complementary information can be learned from the IR spectrum of a material. Since rubrene has a point of inversion, modes are exclusively Raman-active and IR-inactive or Raman-inactive and IR-active, so the IR spectrum provides information on different modes compared to the Raman spectrum. Arthur Ramirez and his students at Lucent Technologies measured the infrared spectrum also using crystals grown by Christian Kloc. While the crystallites from those experiments may not be from the exact same growth run as the other crystallites I measured, the same lab produced them. Therefore, the crystals in these and the previously described Raman experiments have nearly identical growth parameters, which should make comparisons between the Raman and IR data possible. The theoretical calculation previously discussed in Section 4.1.5 that predicted Raman frequencies also generates IR frequencies and intensities.

Many of the experimentally-measured peaks have a very close correspondence to theoretically-predicted peaks. The data sets, however, clearly match each other better in some places than in others. Figure 4.10 shows the comparison of the theory for the isolated molecule and the measured experimental spectrum for the single crystals of rubrene. Table 4.9 lists the peak positions, intensities and percentage difference between the theory and experiment for the molecule. Peaks seem either to match up very well (see for example Figures 4.10 (b) and (e)) or to be completely absent (Figures 4.10 (c) and (d)). For the peaks that do match well, the positions of the peaks in the calculated spectrum, when plotted against the positions from the experimentally-measured spectrum, lie along a least-squares fit line with a slope of 0.9975 and a correlation coefficient of 0.9999 (see Figure 4.11).

There are a few predicted peaks that do not appear in the experimental spectrum at all. The crystallites measured are platelets, similar in dimensions

to the initial crystallites I used in my experiments. The possible IR modes of rubrene have symmetries A_u , B_{1u} , B_{2u} , and B_{3u} . With the platelets and a backscattering experimental geometry, the IR measurements could access only A_u and B_{3u} symmetry modes. As the geometry of the experimental setup allows for observation only of modes with specific symmetries, the remaining modes that the theory predicts are most likely inaccessible here. As I do not have access to the equipment that made these measurements, I cannot make a similar follow-up study with the larger three-dimensional crystallites to confirm this hypothesis.

One can see from either Figures 4.10 (c) and (d) or from the table that there are quite a few strong experimental lines that the theory did not predict at all. As the other modes match so well, I believe that these modes are from impurities in the material. Since rubrene so readily forms a peroxide, if these crystals were exposed to oxygen, we might expect to see some C=O stretching modes around 1800 cm^{-1} . The modes at slightly higher frequency (but below the C-H stretching modes at 3000 cm^{-1} and above) are probably the result of other impurities - possibly the A and B compounds mentioned by Zeis, *et. al* [148], which are impurities commonly found after vapor crystal growth of rubrene. Compound A in particular ($\text{C}_{42}\text{H}_{30}$) comprises more than just benzene rings, and would therefore have C-C and C=C stretching modes at energies different from rubrene.

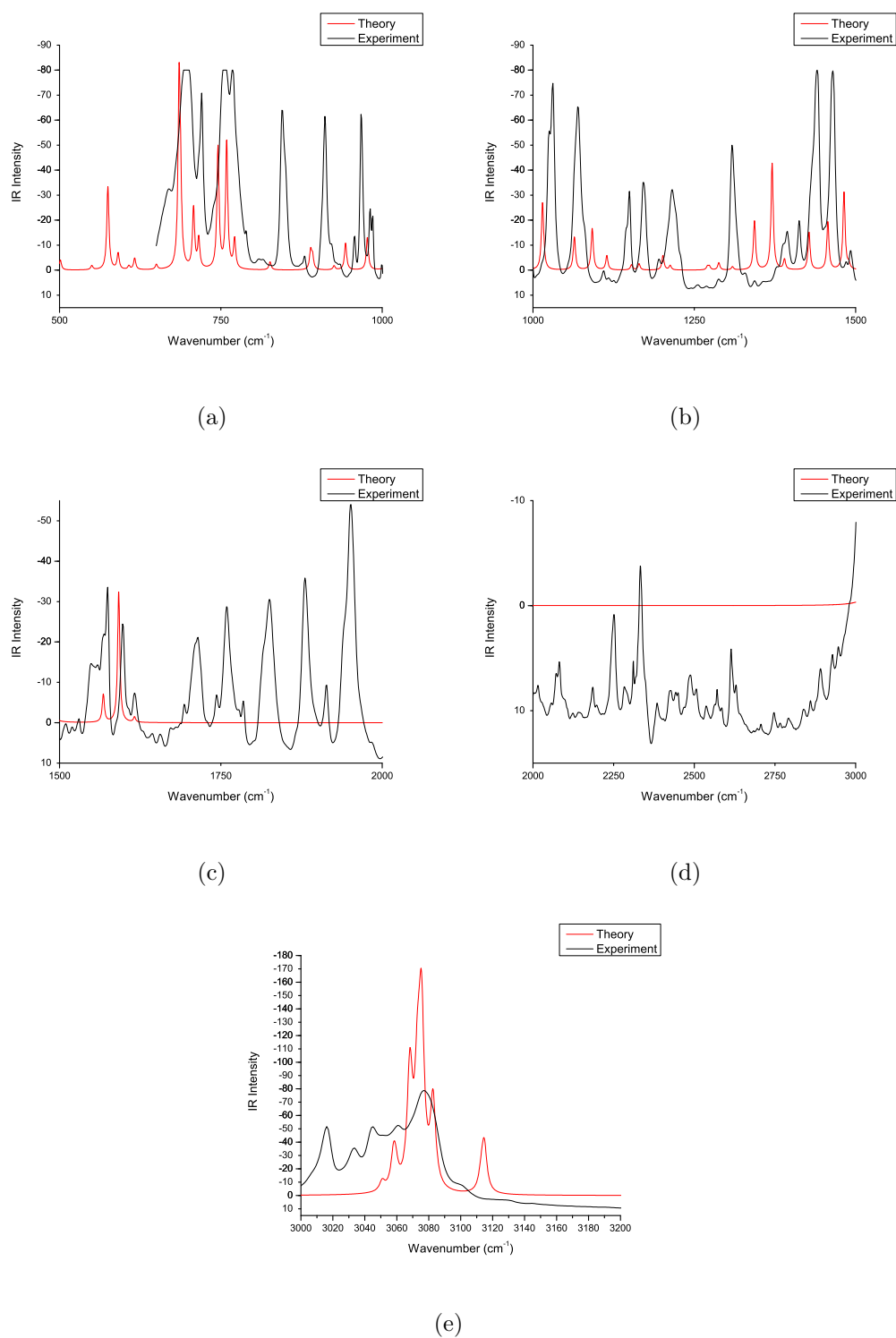


Figure 4.10: Comparing theoretical predictions for isolated molecules and experimental measurements of single crystals of the IR spectrum of rubrene

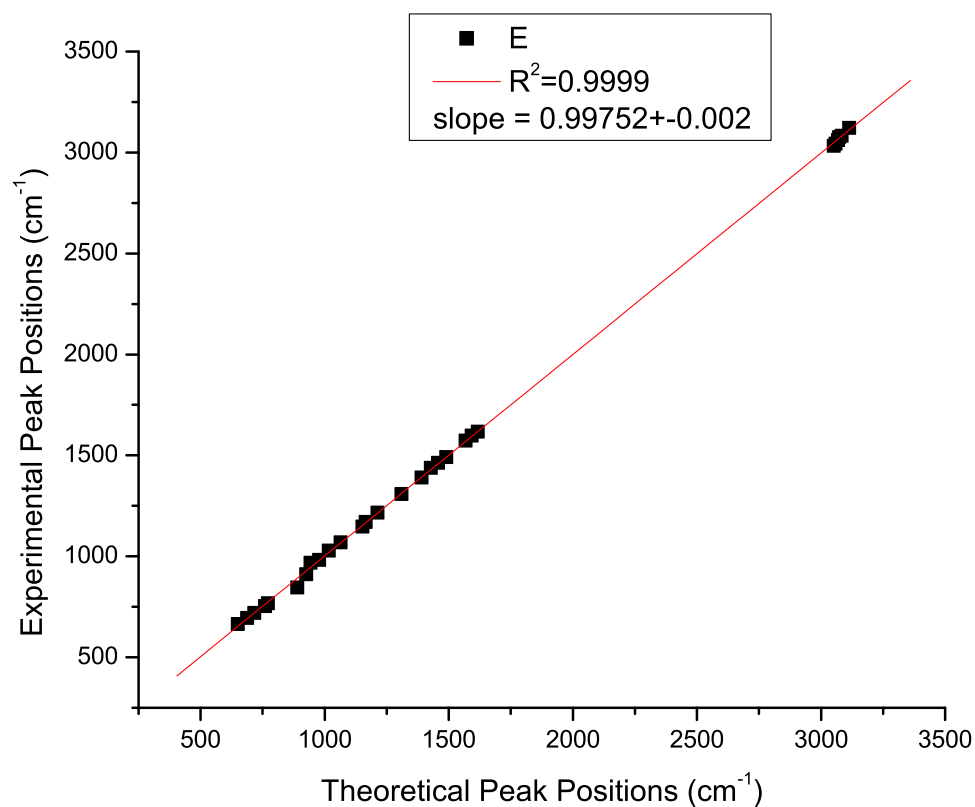


Figure 4.11: Experimental vs. theoretical peak positions for infrared spectrum of rubrene single crystals

Table 4.9: Infrared Peak Positions and Intensities from Theoretical Simulations Using GAUSSIAN 03 and Experimental Measurements

Th. Peak Pos. (cm ⁻¹)	Predicted Int. (arb. units)	Exp. Peak Pos. (cm ⁻¹)	Measured Int. (arb. units)	% Diff
616.4	4.6	-	-	
650.1	2	665.1	17.9	2%
685.3	72	695.9	84.3	1.5%
687.5	23.9	695.9 ^a	84.3	1.2%

Continued on the next page

^aExact identification of this peak questionable

Table 4.9 cont.

Th. Peak Pos. (cm ⁻¹)	Predicted Int. (arb. units)	Exp. Peak Pos. (cm ⁻¹)	Measured Int. (arb. units)	% Diff
707.6	24.2	-	-	
715.7	11.8	720.0	49.2	0.6%
745.6	48.7	-	-	
759	50.7	754.1	63.4	-0.6%
771.3	11.7	768.6	64.1	-0.3%
826.2	3.2	-	-	
889.1	7.4	846.3	66.6	-5%
892.1	5.1	-	-	
925.4	1.6	911.3	63.6	-1.5%
943.2	10.7	967.7	66.1	2.5%
977	12.9	982.7	24.7	0.6%
1014.8	26.1	-	-	
1016.7	2	1028.7	79.8	1.1%
1063.7	13.5	1069.4	73.6	0.5%
1091.8	16.6	-	-	
1114.5	5.7	-	-	
1152.7	2.1	1148	33.8	-0.4%
1164.4	2.5	1171.6	43.1	0.6%
1201.4	5.8	-	-	
1212.6	1.8	1216	40.2	0.3%
1271.8	2.8	-	-	
1287.9	2.9	-	-	
1309.1	1.3	1309.5	57.8	<0.1%
1343.2	19.5	-	-	
1370.6	42.7	-	-	

Continued on the next page

Table 4.9 cont.

Th. Peak Pos. (cm^{-1})	Predicted Int. (arb. units)	Exp. Peak Pos. (cm^{-1})	Measured Int. (arb. units)	% Diff
1389.7	4.1	1391.4	19.3	0.1%
1427.8	15	1412.5	19.8	1.1%
1457	19.1	1438.8	84.4	1.3%
1481.7	31.2	1464.3	87.7	-1.1%
1489.4	2	1492.1	11.2	0.2%
1523.1	0.6	1556.2	22.6	2.1%
1567.7	7	1573.2	29.8	0.3%
1592	32.6	1597.9	28.1	0.4%
1616.2	1.3	1617.1	11.1	<0.1%
-	-	1815.6	16.3	
-	-	1826.2	36.0	
-	-	1881.2	44.4	
-	-	1912.8	14.7	
-	-	1939.8	13.7	
-	-	1951.6	62.7	
-	-	2249.5	9.6	
-	-	2333.0	13.9	
-	-	2925.5	2.1	
-	-	3015.6	32.9	
-	-	3022.7	22.7	
3050.8	7.4	3033.2	16.8	-0.5%
3058.5	16	3044.6	22.9	-0.4%
3068	88.4	3061.5	50.1	-0.2%
3072.9	71.2	3076.2	48.9	0.1%
3075.3	130	3083.5	35.5	0.3%

Continued on the next page

Table 4.9 cont.

Th. Peak Pos. (cm^{-1})	Predicted Int. (arb. units)	Exp. Peak Pos. (cm^{-1})	Measured Int. (arb. units)	% Diff
3082.7	65.7	3096.0	13.7	0.4%
3113.8	47.2	3122.6	1.8	0.3%

4.3 Photoluminescence of Rubrene

4.3.1 Crystals and Experimental Setup

For the photoluminescence experiments described below, I used the same platelet crystallites from the Raman measurements described in Section 4.1.2. The particular crystallites chosen were rather large, so I could measure multiple positions on each crystallite. The PL results reported here are often an average from different locations (at least four per crystallite).

4.3.2 Low Temperature Photoluminescence Results

Unlike the previous Raman sections, it makes more sense to start the photoluminescence discussion with the low temperature results because such spectra are more straightforward. Electronic transitions at low temperatures are narrower due to less thermal broadening and show no quenching or trapping – both situations that slightly complicate the higher temperature spectra. Figure 4.12 shows a typical spectrum from a single position on one platelet crystallite. At low temperatures, there is not much variation with position on the crystallites. Figure 4.13 shows eleven scans from different positions on the two mounted crystallites. The spectra are essentially the same.

As discussed in Section 2.4.1, the different peaks in the PL spectrum represent radiative recombination pathways in a photoexcited material. The particular pathways depend on the actual created excited states of the material. Table 4.10

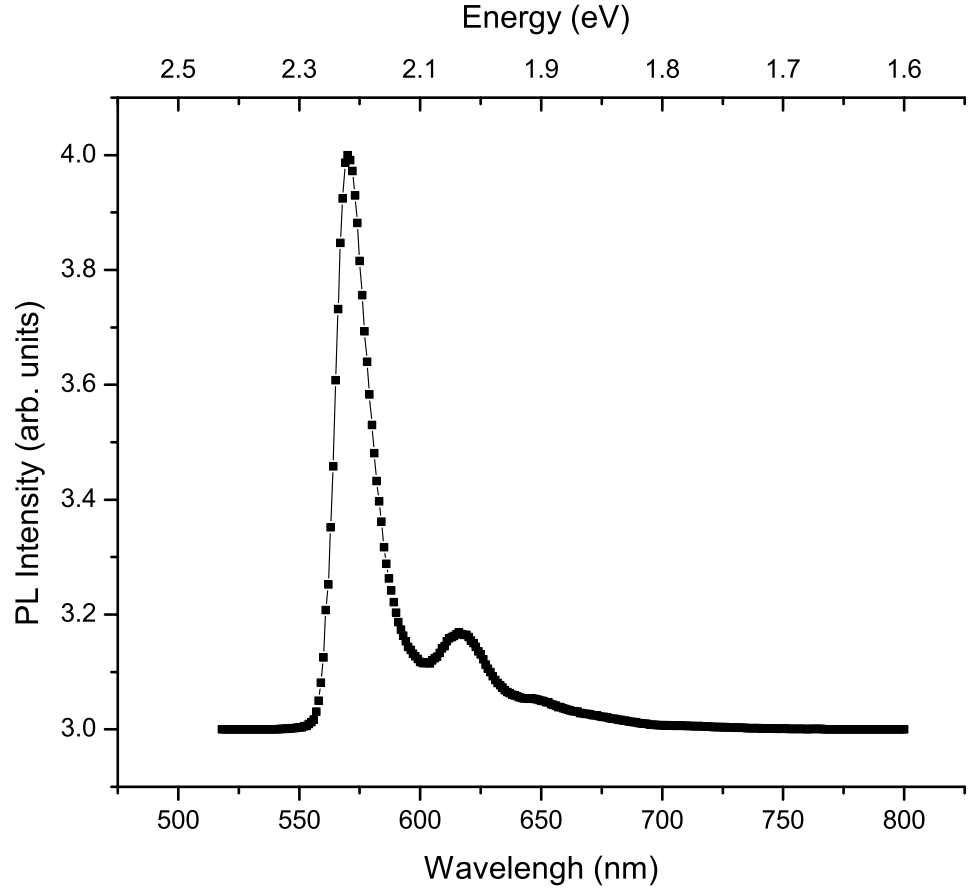


Figure 4.12: One low temperature (18K) photoluminescence spectrum of rubrene single crystals after photoexcitation from an incident energy source of 2.41 eV

lists the average peak positions from fitting the photoluminescence measured in this experiment. An example of the number and location of Gaussian lineshapes used to fit the PL spectra is shown in Figure 4.14.

In a recent paper by Najafov, *et al.* [142], groups at Rutgers and Lehigh Universities measured the excitation spectra of transient luminescence and transient photoconductivity after pulsed excitations with various energies (from 420 to 680 nm or 2.95 to 1.82 eV). They found that the primary photoexcitations in rubrene single crystals are free excitons if the incident photon energy is above

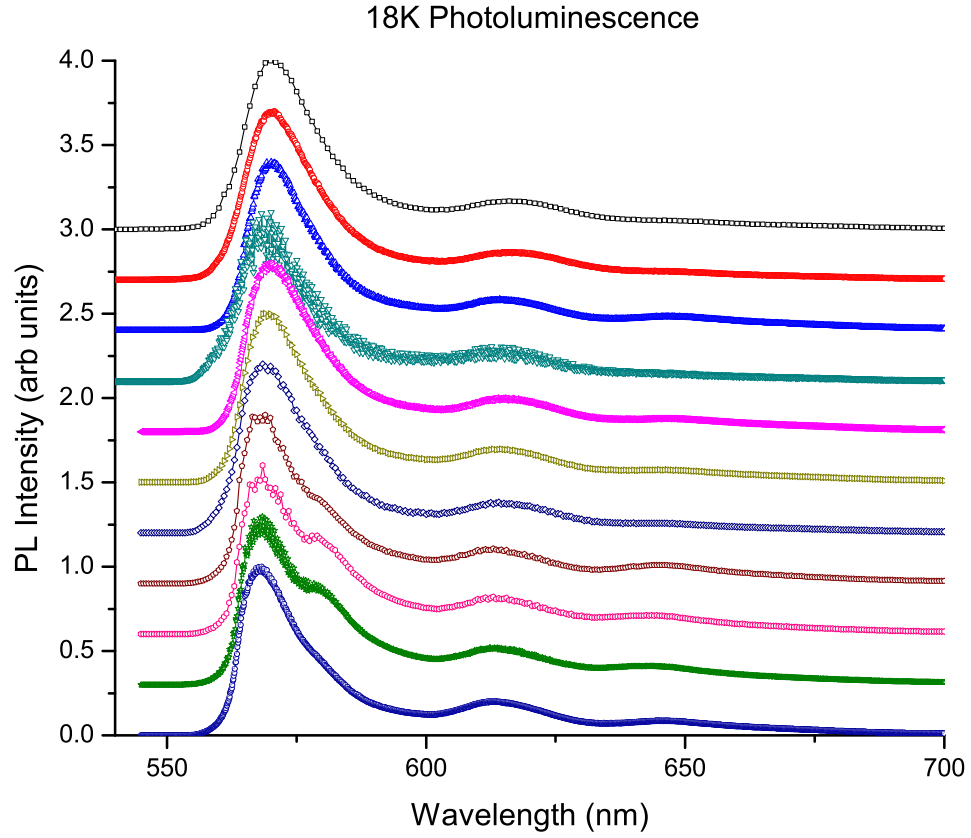


Figure 4.13: Eleven different positions from photoluminescence measurements of rubrene single crystals at 18 K after photoexcitation from an incident energy source of 2.41 eV

2.0 eV. At higher incident photon energies, there are also excited states with higher vibronic levels. This free exciton (which the experiments described here most likely also create as the incident photon energy used is at least 2.41 eV) can, according to Najafov, *et al.*, follow one of three possible relaxation pathways. First, it could radiatively recombine and emit a band centered at 570 nm (2.18 eV). Secondly, it could convert the free exciton into a molecular exciton that, when it radiatively recombines, emits a band centered at 620 nm (2 eV). Finally, it could lead to an intermediate state which self-ionizes into free carriers. The band centered at 570 nm from free excitons matches very well with the three first

Table 4.10: Peak Positions from Low Temperature (18 K) Photoluminescence Measurements of Rubrene Single Crystals

Peak Position	
Wavelength (nm)	Energy (eV)
567.7	2.184
573.9	2.161
584.8	2.120
613.8	2.020
637.7	1.944

observed peaks in Table 4.10, while the band centered at 620 nm from molecular excitons matches fairly closely with the fourth peak in the observed spectrum (2.0 eV from the literature compared to 2.02 eV reported here). The final peak, in my experimentally-measured spectrum, well within the band gap (almost a quarter of an eV from the band edge), is most likely a bound exciton as described in Section 2.4.1.

4.3.3 Comparison to Theory

In an attempt to learn more about the structure of the excited states of the system, Shubin Liu made theoretical calculations on the material. While the full crystal is too complex for current, locally available computing capabilities, it was possible to generate some information about the excited states of one and two molecules of rubrene. The calculations took progressively more time (run one, with one molecule, took 22 hours, while run two, with two molecules, took 6 days and 10 hours to converge) without substantial changes to the excited state energies predicted. The calculation assumes zero temperature, and therefore it is best to compare it to the low-temperature photoluminescence measurements of rubrene. The first excited state that the theory predicts is at 2.1945 eV, only 0.5% different from that measured at 18 K. Remembering that one should

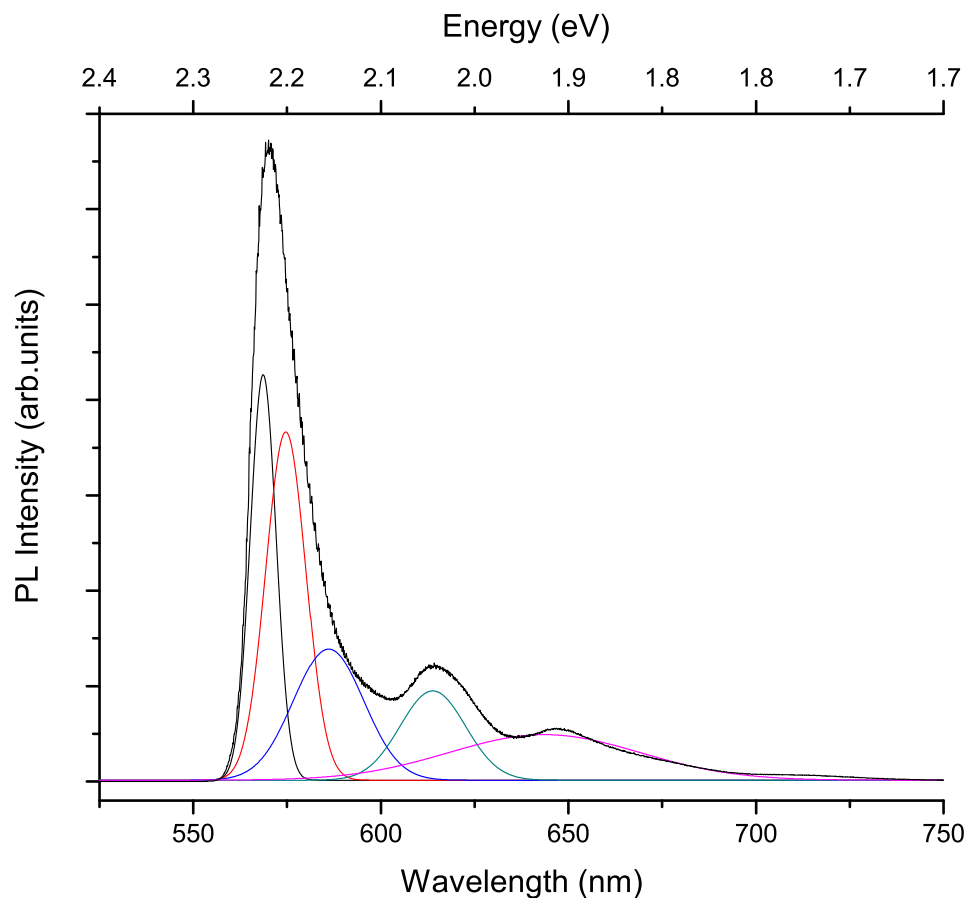


Figure 4.14: Example fit of photoluminescence spectrum of rubrene single crystal at 18 K photoexcited with an energy of 514.5 nm (2.41 eV).

expect a small energy increase as the temperature of the sample decreases, the calculations indicates that the one- and two-molecule simulations do quite a good job predicting the band edge transition in the material (in reality, just the HOMO/LUMO separation since the calculation is not for a crystal). However, since these simulations are not for the single crystal, they will not be able to help with the identification of the other states measured, which lie in the band gap and are therefore most likely excitonic in nature, as previously discussed. If the theory is correct (and it is difficult to argue that it is fundamentally wrong

since it matches the experimentally-measured highest energy emission so well), then this result is in direct conflict with the conclusions reached by Najafov, *et al.* They claim that the highest emission peak is due to free excitons, but our theoretical predictions and experimental spectra indicate that the emission is actually from band-to-band transitions in rubrene single crystals.

4.3.4 Temperature Dependence of Rubrene PL Spectra

Once one understands the low temperature spectrum of rubrene single crystals, albeit with a possible unresolved identification of the highest energy emission peak, it is instructive to follow the different excitation levels with changing temperature of the sample. I controlled the temperature of the refrigerator to within 0.5 K, and took measurements every 25 degrees approximately. Table 4.11 lists the emission peak position from fits of the data; Figure 4.15 shows a plot of the same information for ease of interpretation.

Figure 4.15 has many different pieces of information. I will discuss each peak's temperature trace in turn. First, I added the theoretical value for the first excited transition of rubrene to the plot at 0 K. This seems to track nicely the trajectory of the highest energy PL peak (red line). The two highest emission energy peaks of the PL spectrum gradually decrease in intensity with increasing temperature until experiments can no longer detect them. There is an observable redshift just as Section 2.4.2 predicted. The shrinking band gap of a material with increasing temperature causes the observed redshift. Peak 1 from this figure is due to transitions from the bottom of the conduction band to the valence band. Peak 2 has the same temperature dependence as that of Peak 1. It could be due to either transitions from an indirect band gap (the emission would then be mediated by phonons) or due to a weakly bound exciton just below the band edge. As the temperature increases, increased numbers of phonons make indirect bandgap transitions more probable than direct bandgap transitions. Following the intensity of these two peaks vs. temperature, should therefore show a faster

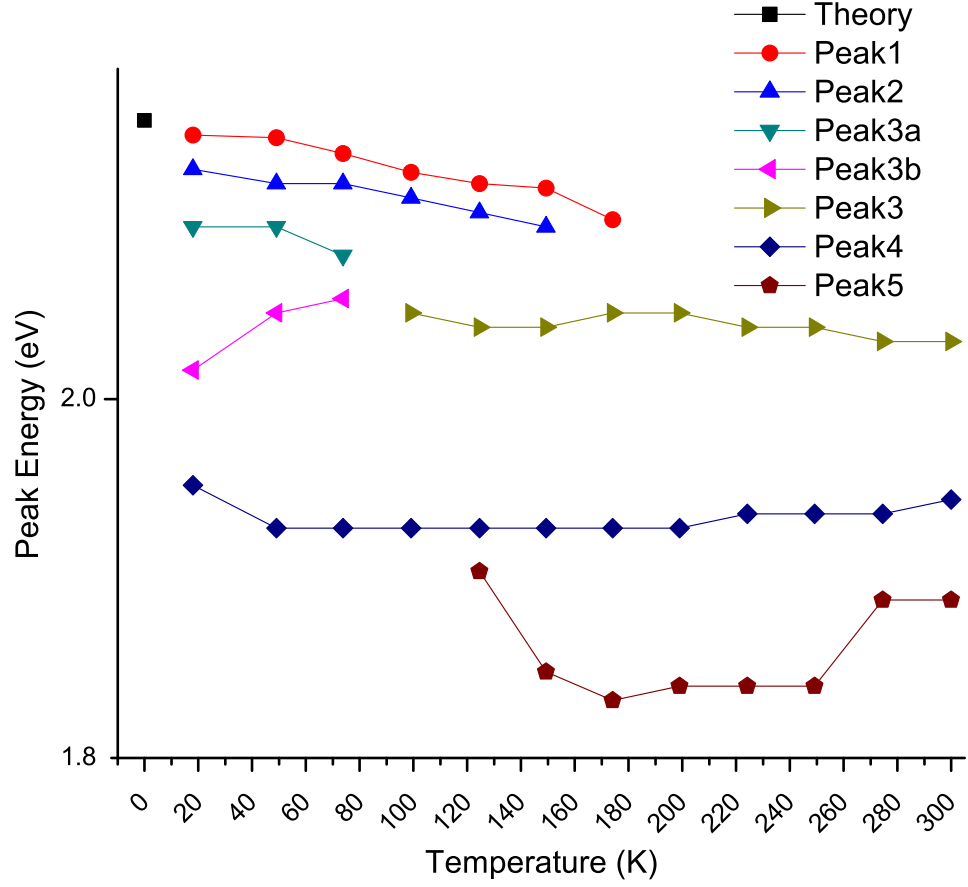


Figure 4.15: Temperature Dependence of the Peak Positions in the Photoluminescence Spectra of Rubrene Single Crystals

decrease in one emission than the other. However, the two emission lines have the same temperature dependence for the intensity as they do for the emission energy, so this second peak is not likely due to an indirect bandgap transition. Therefore, peak 2 is most likely due to a free exciton, only approximately 20 meV below the band edge. This binding energy is rather low for a Frenkel exciton, but not at all surprising for a weakly bound, charge-transfer exciton. Above 180 K, the band-to-band transition (from free carriers described in Section 4.3.2) and the free exciton emission are no longer observable. The temperature of 180 K corresponds to 15 meV, basically the exact same binding energy of the exciton. The observed

quenching of peak 2, therefore, is most likely due to thermal dissociation of the charge transfer exciton. The quenching of the band-to-band transition, on the other hand, is due to the increased number of non-radiative pathways that exist with increasing temperature in the sample (i.e., the increased number of phonons).

Table 4.11: Photoluminescence peak energy vs. temperature for rubrene single crystals

Temp. (K)	Pk Pos. (eV)	Pk Pos. (eV)	Pk Pos. (eV)	Pk Pos. (eV)	Pk Pos. (eV)	Pk Pos. (eV)
0.0 ^a	2.194					
18.0	2.184	2.16	2.12	2.02	1.94	-
49.0	2.182	2.15	2.12	2.06	1.91	-
73.8	2.171	2.15	2.10	2.07	1.91	-
99.1	2.158	2.14	-	2.06	1.91	-
124.6	2.150	2.13	-	2.05	1.91	1.88
149.3	2.147	2.12	-	2.05	1.91	1.81
174.1	2.125	-	-	2.06	1.91	1.79
199.0	-	-	-	2.06	1.91	1.80
224.1	-	-	-	2.05	1.92	1.80
249.2	-	-	-	2.05	1.92	1.80
274.5	-	-	-	2.04	1.92	1.86
300.0	-	-	-	2.04	1.93	1.86

^a From the theoretical calculation

The third highest energy emission peak in Figure 4.15 is a little confusing at first. There are actually two possible peaks at the lowest temperatures (labeled Peaks 3a and 3b in the figure legend) that seem to merge into one peak at higher temperatures. While it is difficult to track these two peaks individually beyond

about 75 K, this is not a surprising result. As the temperature of a material increases, increased numbers of phonons in the system will thermally broaden energy levels which, in turn, broaden emission lines. The merging of Peaks 3a and 3b into Peak 3 is an example of this very effect. The slightly surprising behavior is that Peak 3b actually increases in energy with increasing temperature over a short range before becoming indistinguishable from Peak 3a. This indicates that this particular peak is not from band-to-band emission since Peaks 1, 2 and 3a conclusively show that the band edge shrinks with increasing temperature. As predicted by Najafov, *et al.*, a molecular exciton emission could cause this peak. The higher temperature trace of Peak 3, at approximately 2 eV would support this identification and one would not expect it to have a strong temperature dependence.

Peak 4 from Figure 4.15 has a different temperature dependence from those previously discussed. Although the other peaks do not change much (0.06 eV or less over 175 K), Peak 4 basically does not shift through the entire temperature range measured. Therefore, a semi-deep level, 0.25 eV below the band edge, is the source of emission for this peak. Other researchers have measured an impurity level in rubrene due to oxygen at approximately 0.3 eV below the conduction band [157]. Oxygen readily diffuses into the crystal, and I made no attempts to prevent oxygen exposure, so it is a likely impurity in the system.

Finally, Peak 5 may seem to move more than any other emission line in terms of energy. But this is a little misleading, and it is, perhaps, incorrect to plot it with the other peaks previously discussed on this temperature dependence diagram. As I mentioned previously, I made measurements at multiple locations on two different crystallites. All of the data I present in this section are averages from these different location scans. This last peak represents emission from different impurities and/or defects in the crystallites that seem to have more variation with location on the crystallites than the temperature of the sample. By eye, these measured crystallites are clearly stacked platelets, and it is not sur-

prising that there are a number of stacking fault lines as well as impurities (recall the A and B compounds mentioned in Section 4.2 that are common impurities in these samples) whose dispersal throughout the crystallites is inhomogeneous. Therefore, it is not surprising that this final peak is the result of a variety of defects and impurities in the crystallites.

4.3.5 Rubrene PL Dependence on Photoexcitation Energy

I also took measurements at room temperature of the same rubrene crystallites with various incident excitation energies. Because of the number of defects that cause traps at room temperature, the resulting spectra vary more by change in location than by change in incident excitation energy. Figure 4.16 shows the PL spectra from three different locations on the crystal for which I used an incident excitation energy of 496.5nm (2.5eV) from an Ar⁺ laser. For these particular scans, I made no attempt to avoid grain boundaries and other large, visible by eye, defects on the crystallites. In contrast, Figure 4.17 shows the change in PL spectra when various excitation energies photoexcited the same location on the crystallite.

Especially considering the variability in PL emission with one excitation, a detailed analysis of the changes in PL spectra with changing excitation energy is a pointless endeavor. Additionally, from a practical standpoint, it is quite difficult to maintain a constant position on a crystal when switching excitation lines (which requires realigning the system between measurements). However, despite these limitations, the spectra in Figure 4.17 are remarkably similar. Clearly, changes in the incident excitation source do not have a strong effect on the photoluminescent spectrum of rubrene single crystals.

All of the excitation energies used in this section are above the band gap of the material. Therefore, the only difference between the scans in Figure 4.17 is

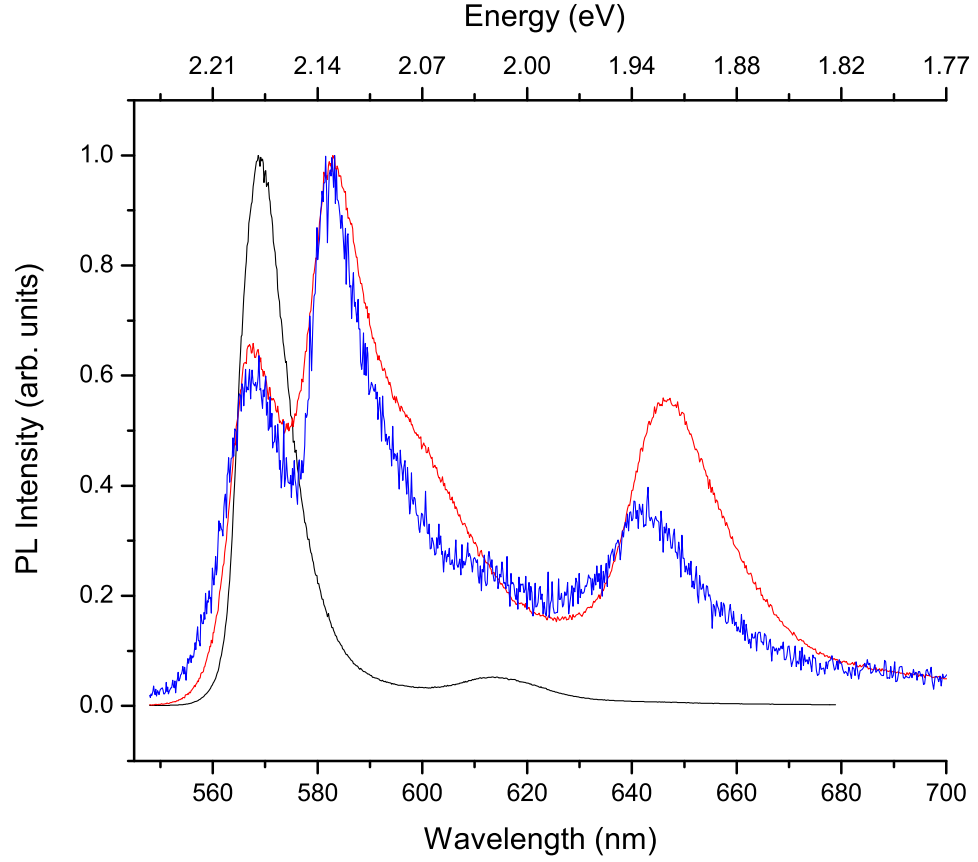


Figure 4.16: PL Spectra from three different locations on rubrene single crystals with 496.5 nm (2.5 eV) excitation source

the penetration depth of the laser with respect to the sample. This penetration depth depends on the absorption of rubrene at each wavelength in question. Najafov, *et al.*, have published an absorption spectrum for rubrene [142]. The intensity at a particular depth in a material is given by the following equation:

$$I(d) = I_0 e^{-\alpha d} \quad (4.5)$$

where I_0 is the intensity of light incident on the sample, $I(d)$ is the intensity at a particular depth, α is the energy dependent absorption and d is the depth into the sample. It is possible to read the values of α for each wavelength used in this experiment straight from the Figure in the literature. One interesting fact about

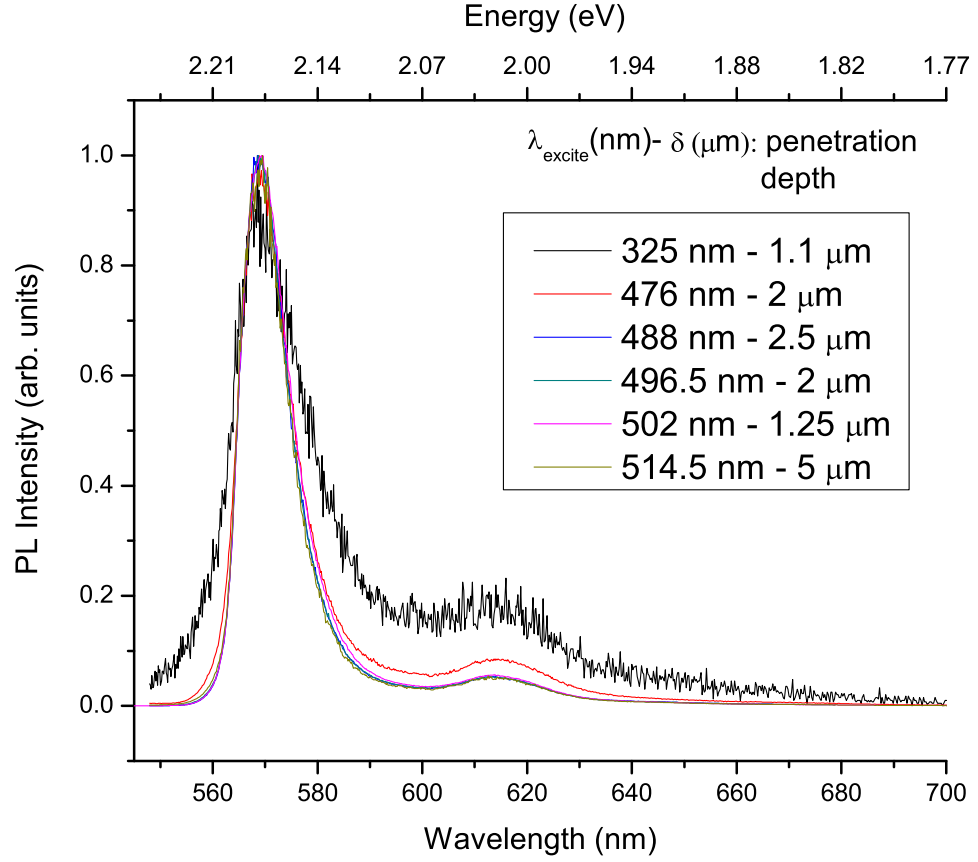


Figure 4.17: PL Spectra from one location on a rubrene single crystal with excitation sources equal to 325 nm (3.81 eV), 476 nm (2.61 eV), 488 nm (2.51 eV), 496.5 nm (2.5 eV), 502 nm (2.47 eV), and 514 nm (2.41 eV)

rubrene is that the absorption spectrum has strong vibronic components which means that α can vary quite a bit over a small energy region. The approximate penetration depths for each laser line used are listed in the legend for Figure 4.17. Remembering that the crystallites measured are approximately microns in thickness, one can see from the different penetration depths that the PL spectra in Figure 4.17 represent probing emission from anywhere from the first micron through the entire sample. The fact that all the PL spectra look remarkably similar is an indication that the crystallites are very homogeneous perpendicular

to the large (001) face. This same homogeneity is not seen when measuring different locations on a single crystallite.

4.4 Conclusion

Since rubrene is of interest to many researchers for its possible application in devices, motivated mostly by an extremely high measured hole mobility, a fundamental understanding of the underlying physics that makes the material unique is important. The Raman data indicate that there are very small intermolecular interactions in rubrene. All organic molecular solids have weak intermolecular bonds, as the van der Waals bonds between molecules are orders of magnitude weaker than the covalent bonds between atoms in a molecule, but rubrene appears to be more of an extreme case than other materials. The intermolecular forces in rubrene are small enough that one cannot measure the vibrational energies with Raman spectroscopy. At the very least, I could not observe the intermolecular modes in any of the experiments described in this chapter. This weak intermolecular coupling as well as weak electron-phonon coupling indicates that the long mean free path, rather than the actual band structure of rubrene is responsible for the high measured mobilities.

The photoluminescence results indicate that photoexcitation creates both free carriers as well as numerous types of band gap states. All of these states can relax through radiative recombination pathways leading to the observed emission lines. The temperature dependence of the photoluminescence spectrum allows the identification of the different types of emission. I recorded emission from free carriers (band-to-band recombination), from free charge transfer excitons, from Frenkel excitons, from impurity states (most likely due to oxygen diffusion in the crystal) and from deep traps caused by defects in the crystallites. The dependence of the PL emission on incident excitation energy is unremarkable. The main conclusion from those measurements is that the crystals are more

homogeneous perpendicular to the (001) than at different positions across the sample.

Chapter 5

Conclusions

In this dissertation, I have sought to build an understanding of the structural and electronic properties of some new and promising organic semiconducting molecular crystals. The desire to produce efficient and novel display devices drives the current interest in the properties of these molecular crystals. Current technological abilities in organic chemistry make the construction of nearly any molecular structure possible. However, “black box chemistry” dominates new material production. Rather than starting from a fundamental understanding of the relationship between the structure of a molecule and its electronic properties, and then customizing molecules for the desired optical properties, researchers test different materials until they find one with promising characteristics. This method works to some degree, as both α -hexathiophene and rubrene have high mobility and have been used in a variety of successful devices; however, this unsystematic approach to materials development is not the most efficient technique.

I have focused on two of these promising molecular crystals that have drawn considerable attention from other researchers for their possible applications in a host of display devices. A complete understanding of the relationship between structure and electronic properties is still a goal for the distant future, but this work has started to illustrate some of the interesting connections in these materials.

In α -hexathiophene, resonant Raman experiments yielded information about previously-unidentified low energy excitations. These particular electronic transitions couple to vibrational modes of the material. I have tentatively identified these low energy excitations as the Davydov splitting of a free triplet Frenkel exciton or two bound singlet Frenkel excitons. Following the resonance's temperature dependence allowed me to measure a quenching of the coupling at 55 K, which is a direct link to the binding energy of the triplet exciton or the binding energy of the traps of the singlet excitons at 4.7 meV.

In rubrene, the measured Raman, infrared, and photoluminescence spectra were compared to the results of theoretical calculations. While all molecular crystals have low intermolecular coupling, I found rubrene to have exceptionally low coupling, to the point that I was not able to measure any intermolecular vibrational modes. To date, rubrene has the highest measured mobility compared to other small organic molecular crystals. This appears to contradict the Raman results because a high mobility usually implies strong π -electron overlap, running counter to the small intermolecular coupling measured. The resolution of this apparent conflict may lie in the fact that most of the mobility measurements are made on device structures that have not been encapsulated. Rubrene readily forms an endoperoxide on its surface, and the FET mobility measurements measure surface conduction. Thus, the high mobility may in fact be of the endoperoxide, while the low intermolecular coupling results that the Raman spectra suggest are just the bulk properties of the rubrene crystals. Or, rubrene might actually have a very high intrinsic mobility as suggested by FET measurements. In that case, the apparent conflict is resolved with the understanding that band structure and effective mass do not uniquely determine mobility. The time between collisions (related to the mean free path) must also be considered. For the extremely high measured mobilities and low intermolecular coupling, therefore, rubrene must also have very large mean free paths (and low electron-phonon coupling) which is a consequence of the low intermolecular coupling suggested

by the Raman results.

The photoluminescence spectra of rubrene show very little change with changing incident excitation source, indicating that the crystallites are very homogeneous in cross-section. I have classified the different PL emission peaks as emission from band-to-band transitions (free carriers), free charge transfer and Frenkel excitons, oxygen impurities levels and deep traps caused by defects and other impurities in the crystals. The temperature dependence of these emission peaks follow the expected trajectories and helped with the identifications of Chapter 4.

Both α -hexathiophene and rubrene are promising molecular crystals that researchers have already incorporated into a host of photonic devices. Not only to these materials have interesting properties that make them attractive for novel products, they also have interesting physical properties, namely the strong electron-phonon coupling of α -hexathiophene and the incredibly weak intermolecular coupling of rubrene single crystals. Once scientists reach a fundamental understanding of the interplay between the structure and electronic properties of these materials, the possibilities for future developments are very exciting. Eventually scientists will reach the goal of understanding how to tailor molecules to have the exact properties required for specific applications. At that point, chemists, physicists and engineers can work together to create new, more efficient, higher resolution, longer lifetime display devices.

REFERENCES

- [1] M. Pope and C. E. Swenberg, *Electronic Processes in Organic Crystals* (Oxford University Press, New York, 1982).
- [2] E. A. Silinsh, *Organic Molecular Crystals: Their Electronic States*, Vol. 16 of Springer Series in Solid-State Sciences (Springer-Verlag, New York, 1980).
- [3] C. W. Tang and S. A. VanSlyke, "Organic electroluminescent diodes," *Applied Physics Letters* **51**, 913–15 (1987).
- [4] G. Horowitz, "Organic thin film transistors: From theory to real devices," *Journal of Materials Research* **19**, 1946–1962 (2004).
- [5] G. Horowitz, F. Garnier, A. Yassar, R. Hajlaoui, and F. Kouki, "Field-effect transistor made with a sexithiophene single crystals," *Advanced Materials* **8**, 52–4 (1996).
- [6] G. Horowitz, "Organic semiconductors for new electronic devices," *Advanced Materials* **2**, 287–92 (1990).
- [7] D. Sweatman, "Organic Devices: A Review," in *Microelectronic Engineering Research Conference (MERC)* pp. 1–4 (2001).
- [8] H. Inokuchi, "Organic semiconductors, past and present," *Molecular Crystals and Liquid Crystals* **125**, 51–8 (1985).
- [9] S. Matsumoto, "Organic semiconductors and their applications," *Journal of the Institute of Electronics and Communication Engineers of Japan* **55**, 397–408 (1972).
- [10] V. Podzorov, V. M. Pudalov, and M. E. Gershenson, "Field-effect transistors on rubrene single crystals with parylene gate insulator," *Applied Physics Letters* **82**, 1739–41 (2003).
- [11] A. R. Brown, C. P. Jarrett, D. M. de Leeuw, and M. Matters, "Field-effect transistors made from solution-processed organic semiconductors," *Synthetic Metals* **88**, 37–55 (1997).
- [12] H. Akimichi, K. Waragai, S. Hotta, H. Kano, and H. Sakaki, "Field-effect transistors using alkyl substituted oligothiophenes," *Applied Physics Letters* **58**, 1500–2 (1991).

- [13] D. Fichou, P. Demanze, G. Horowitz, R. Hajlaoui, M. Constant, and F. Garnier, "Structural, spectroscopic and device characteristics of octithiophene," *Synthetic Metals* **85**, 1309–12 (1997).
- [14] G. Horowitz, D. Fichou, X. Peng, Z. Xu, and F. Garnier, "A field-effect transistor based on conjugated alpha-sexithienyl," *Solid State Communications* **72**, 381–4 (1989).
- [15] G. Horowitz, X. Peng, D. Fichou, and F. Garnier, "The oligothiophene-based field-effect transistor: how it works and how to improve it," *Journal of Applied Physics* **67**, 528–32 (1990).
- [16] G. Horowitz, "Organic field-effect transistors," *Advanced Materials* **10**, 365–77 (1998).
- [17] H. Koezuka, A. Tsumura, and T. Ando, "Field-effect transistor with polythiophene thin film," *Synthetic Metals* **18**, 699–704 (1987).
- [18] M. Matters, D. M. De Leeuw, M. J. C. M. Vissenberg, C. M. Hart, P. T. Herwig, T. Geuns, C. M. J. Mutsaers, and C. J. Drury, "Organic field-effect transistors and all-polymer integrated circuits," *Optical Materials* **12**, 189–97 (1999).
- [19] F. Garnier, "Thin film transistors based on organic conjugated semiconductors," *Current Opinion in Solid State & Materials Science* **2**, 455–61 (1997).
- [20] H. E. Katz, "Organic molecular solids as thin film transistor semiconductors," *Journal of Materials Chemistry* **7**, 369–376 (1997).
- [21] D. J. Gundlach, Y. Y. Lin, T. N. Jackson, S. F. Nelson, and D. G. Schlom, "Pentacene organic thin-film transistors - Molecular ordering and mobility," *IEEE Electron Device Letters* **18**, 87–89 (1997).
- [22] D. J. Gundlach, J. A. Nichols, L. Zhou, and T. N. Jackson, "Thin-film transistors based on well-ordered thermally evaporated naphthalene films," *Applied Physics Letters* **80**, 2925–2927 (2002).
- [23] M. Matsumura and T. Furukawa, "Properties of organic light-emitting devices with a rubrene sub-monolayer inserted between electron- and hole-transport layers," *Japanese Journal of Applied Physics, Part 1 (Regular Papers, Short Notes & Review Papers)* **41**, 2742–5 (2002).
- [24] J. R. Sheats, H. Antoniadis, M. Hueschen, W. Leonard, J. Miller, R. Moon, D. Roitman, and A. Stocking, "Organic electroluminescent devices," *Science* **273**, 884–8 (1996).

- [25] H. J. Bolink, M. Buechel, B. Jacobs, M. M. de Kok, M. Ligter, E. A. Meulenkaamp, S. Vulto, and P. van de Weijer, "Status of red, green and blue light emitting polymers for passive matrix displays," *Proceedings of the SPIE - The International Society for Optical Engineering* **4800**, 1–15 (2003).
- [26] Y. Taniguchi, "Organic light-emitting diodes and organic semiconductor lasers," *Oyo Buturi* **70**, 1294–8 (2001).
- [27] F. Cacialli, R. N. Marks, R. H. Friend, R. Zamboni, C. Taliani, S. C. Moratti, and A. B. Holmes, "Electrical and luminescent properties of double-layer oligomeric/polymeric light-emitting diodes," *Synthetic Metals* **76**, 145–8 (1996).
- [28] J. Poortmans, W. Geens, S. C. Jain, J. Nijs, and R. Mertens, "The opportunities and challenges of organic solar cells," *Proceedings of the SPIE - The International Society for Optical Engineering* **3975**, 1206–13 (2000).
- [29] J. Ackermann, C. Videlot, and A. El Kassmi, "Growth of organic semiconductors for hybrid solar cell application," *Thin Solid Films* **403-404**, 157–61 (2002).
- [30] L. Sicot, C. Fiorini, A. Lorin, P. Raimond, C. Sentein, and J. M. Nunzi, "Improvement of the photovoltaic properties of polythiophene-based cells," *Solar Energy Materials and Solar Cells* **63**, 49–60 (2000).
- [31] T. Fromherz, F. Padinger, D. Gebeyehu, C. Brabec, J. C. Hummelen, and N. S. Sariciftci, "Comparison of photovoltaic devices containing various blends of polymer and fullerene derivatives," *Solar Energy Materials and Solar Cells* **63**, 61–8 (2000).
- [32] A. S. Arutyunov, "Rubrene-based film actinometer for ultraviolet radiation," *Pribory i Tekhnika Eksperimenta* **25**, 224–5 (1982).
- [33] Y. Ohmori, H. Kajii, T. Tsukagawa, T. Taneda, M. Yamazaki, M. Hikita, S. Tomaru, and H. Takenaka, "Integration of organic electroluminescent diodes and polymeric waveguide devices: Characterization of light source for optical integrated circuit," *Proceedings of the SPIE - The International Society for Optical Engineering* **4439**, 95–102 (2001).
- [34] H. Kajii, T. Taneda, T. Tsukagawa, M. Kaneko, and Y. Ohmori, "Application of organic electroluminescence device to the electro-optical conversion device for optical link," *Transactions of the Institute of Electronics, Information and Communication Engineers C* **J85-C**, 1097–102 (2002).

- [35] B. Crone, A. Dodabalapur, A. Gelperin, L. Torsi, H. E. Katz, A. J. Lovinger, and Z. Bao, "Electronic sensing of vapors with organic transistors," *Applied Physics Letters* **78**, 2229–31 (2001).
- [36] L. Wang, D. Fine, and A. Dodabalapur, "Nanoscale chemical sensor based on organic thin-film transistors," *Applied Physics Letters* **85**, 6386–8 (2004).
- [37] M. Zavelani-Rossi, G. Lanzani, S. De Silvestri, M. Anni, G. Gigli, R. Cingolani, G. Barbarella, and L. Favaretto, "Single-mode tunable organic laser based on an electroluminescent oligothiophene," *Applied Physics Letters* **79**, 4082–4 (2001).
- [38] M. J. Frisch, G. W. Trucks, H. B. Schlegel, G. E. Scuseria, M. A. Robb, J. R. Cheeseman, J. J. A. Montgomery, T. Vreven, K. N. Kudin, J. C. Burant, J. M. Millam, S. S. Iyengar, J. Tomasi, V. Barone, B. Mennucci, M. Cossi, G. Scalmani, N. Rega, G. A. Petersson, H. Nakatsuji, M. Hada, M. Ehara, K. Toyota, R. Fukuda, J. Hasegawa, M. Ishida, T. Nakajima, Y. Honda, O. Kitao, H. Nakai, M. Klene, X. Li, J. E. Knox, H. P. Hratchian, J. B. Cross, V. Bakken, C. Adamo, J. Jaramillo, R. Gomperts, R. E. Stratmann, O. Yazyev, A. J. Austin, R. Cammi, C. Pomelli, J. W. Ochterski, P. Y. Ayala, K. Morokuma, G. A. Voth, P. Salvador, J. J. Dannenberg, V. G. Zakrzewski, S. Dapprich, A. D. Daniels, M. C. Strain, O. Farkas, D. K. Malick, A. D. Rabuck, K. Raghavachari, J. B. Foresman, J. V. Ortiz, Q. Cui, A. G. Baboul, S. Clifford, J. Cioslowski, B. B. Stefanov, G. Liu, A. Liashenko, P. Piskorz, I. Komaromi, R. L. Martin, D. J. Fox, T. Keith, M. A. Al-Laham, C. Y. Peng, A. Nanayakkara, M. Challacombe, P. M. W. Gill, B. Johnson, W. Chen, M. W. Wong, C. Gonzalez, , and J. A. Pople, "Gaussian 03, Revision C.02," (2004).
- [39] D. Beljonne, Z. Shuai, and J. L. Bredas, "Theoretical study of thiophene oligomers: electronic excitations, relaxation energies, and nonlinear optical properties," *Journal of Chemical Physics* **98**, 8819–28 (1993).
- [40] M. Bennati, K. Nemeth, P. R. Surjan, and M. Mehring, "Zero-field-splitting and π -electron spin densities in the lowest excited triplet state of oligothiophenes," *Journal of Chemical Physics* **105**, 4441–7 (1996).
- [41] M. Belletete, N. DiCesare, M. Leclerc, and G. Durocher, "Conformational analysis and electronic properties of bithiophene and terthiophene in their ground state as well as in their first excited singlet and triplet states," *Chemical Physics Letters* **250**, 31–39 (1996).
- [42] F. Garnier, G. Horowitz, X. Z. Peng, and D. Fichou, "Structural basis

- for high carrier mobility in conjugated oligomers,” *Synthetic Metals* **45**, 163–171 (1991).
- [43] G. Horowitz, R. Hajlaoui, and F. Kouki, “An analytical model for the organic field-effect transistor in the depletion mode. Application to sexithiophene films and single crystals,” *European Physical Journal, Applied Physics* **1**, 361–7 (1998).
 - [44] G. Horowitz and M. E. Hajlaoui, “Mobility in polycrystalline oligothiophene field-effect transistors dependent on grain size,” *Advanced Materials* **12**, 1046–50 (2000).
 - [45] M. Muccini, E. Lunedei, C. Taliani, D. Beljonne, J. Cornil, and J. L. Bredas, “Interchain interaction in a prototypical conjugated oligomer from polarized absorption at 4.2 K: alpha -sexithienyl single crystal,” *Journal of Chemical Physics* **109**, 10 513–20 (1998).
 - [46] S. V. Frolov, C. Kloc, B. Batlogg, M. Wohlgenannt, X. Jiang, and Z. V. Vardeny, “Excitation dynamics in single molecular crystals of alpha -hexathiophene from femtoseconds to milliseconds,” *Physical Review B (Condensed Matter and Materials Physics)* **63**, 205 203/1–12 (2001).
 - [47] D. M. Shin, S. T. Lim, J. S. Choi, and J. S. Kim, “Influence of oligothiophene layer on the light emitting efficiency,” *Thin Solid Films* **363**, 268–70 (2000).
 - [48] F. Kouki, P. Spearman, G. Horowitz, P. Delannoy, P. Valat, V. Wintgens, and F. Garnier, “Improved electroluminescence from oligothiophenes,” *Synthetic Metals* **102**, 1071–2 (1999).
 - [49] D. Fichou, V. Dumarcher, and J. M. Nunzi, “One- and two-photon stimulated emission in oligothiophenes single crystals,” *Synthetic Metals* **101**, 610–13 (1999).
 - [50] G. Horowitz, F. Kouki, A. El Kassmi, P. Valat, V. Wintgens, and F. Garnier, “Structure-dependent fluorescence in sexithiophene single crystals,” *Advanced Materials* **11**, 234–8 (1999).
 - [51] M. Cerminara, A. Borghesi, F. Meinardi, A. Sassella, R. Tubino, and A. Pappagni, “Temperature activated de-trapping processes in vacuum deposited sexithiophene thin films,” *Synthetic Metals* **128**, 63–6 (2002).
 - [52] R. N. Marks, R. H. Michel, W. Gebauer, R. Zamboni, C. Taliani, R. F. Mahrt, and M. Hopmeier, “The origin of photoluminescence from alpha

- sexithienyl thin films,” *Journal of Physical Chemistry B* **102**, 7563–7 (1998).
- [53] X. Cheng, K. Ichimura, D. Fichou, and T. Kobayashi, *Chemical Physics Letters* **185**, 286–291 (1991).
 - [54] J. Cornil, J. P. Calbert, D. Beljonne, R. Silbey, and J. L. Bredas, “Interchain interactions in π -conjugated oligomers and polymers: a primer,” *Synthetic Metals* **119**, 1–6 (2001).
 - [55] A. D. Esposti, O. Moze, C. Taliani, J. T. Tomkinson, R. Zamboni, and F. Zerbetto, “The intramolecular vibrations of prototypical polythiophenes,” *Journal of Chemical Physics* **104**, 9704–18 (1996).
 - [56] A. D. Esposti and F. Zerbetto, “A density functional study of the vibrations of three oligomers of thiophene,” *Journal of Physical Chemistry A* **101**, 7283–91 (1997).
 - [57] A. Esposti, E. Fanti, M. Muccini, C. Taliani, and G. Ruani, “The polarized infrared and Raman spectra of alpha -T6 single crystal: An experimental and theoretical study,” *Journal of Chemical Physics* **112**, 5957–69 (2000).
 - [58] J. T. Lopez Navarrete and G. Zerbi, “Lattice dynamics and vibrational spectra of polythiophene. I. Oligomers and polymer,” *Journal of Chemical Physics* **94**, 957–64 (1991).
 - [59] G. Zerbi, B. Chierichetti, and O. Inganäs, “Vibrational spectra of oligothiophenes as model of polythiophenes,” *Journal of Chemical Physics* **94**, 4637–45 (1991).
 - [60] G. Horowitz, B. Bachet, A. Yassar, P. Lang, F. Demanze, J. L. Fave, and F. Garnier, “Growth and Characterisation of Sexithiophene Single Crystals,” *Chemical Materials* **7**, 1337–1341 (1995).
 - [61] C. Botta, S. Destri, W. Porzio, G. Bongiovanni, M. A. Loi, A. Mura, and R. Tubino, “Optical properties and photoluminescence of tetrahexyl-sexithiophene allotropes,” *Synthetic Metals* **122**, 395–9 (2001).
 - [62] J. Casado, L. L. Miller, K. R. Mann, T. M. Pappenfus, Y. Kanemitsu, E. Orti, P. M. Viruela, R. Pou-Amerigo, V. Hernandez, and J. T. Lopez Navarrete, “Combined spectroelectrochemical and theoretical study of a vinylene-bridged sexithiophene cooligomer: analysis of the π -electron delocalization and of the electronic defects generated upon doping,” *Journal of Physical Chemistry B* **106**, 3872–81 (2002).

- [63] J. Casado, V. Hernandez, F. J. Ramirez, and J. T. Lopez Navarrete, "A theoretical investigation of α , α' -dimethyl end-capped oligothiophenes: structures, vibrational spectra and conjugation defects," *Synthetic Metals* **89**, 159–60 (1997).
- [64] J. Casado, V. Hernandez, F. J. Ramirez, and J. T. Lopez Navarrete, "A theoretical investigation of α , α' -dimethyl end-capped oligothiophenes: structures, vibrational spectra and conjugational defects," *Synthetic Metals* **85**, 1157–8 (1997).
- [65] J. Casado, F. J. Ramirez, H. Shu, J. T. Lopez Navarrete, and V. Hernandez, "Vibrational spectroscopy study of doping induced charged defects in a series of α , α' -dimethyl end-capped oligothiophenes," *Synthetic Metals* **84**, 571–2 (1997).
- [66] J. Casado, V. Hernandez, S. Hotta, and J. T. Lopez Navarrete, "FT-Raman studies of charged defects created on methyl end-capped oligothiophenes by doping with NOBF_4 ," *Advanced Materials* **10**, 1458–61 (1998).
- [67] J. Casado, V. Hernandez, S. Hotta, and J. T. Lopez Navarrete, "Vibrational spectra of charged defects in a series of α , α' -dimethyl end-capped oligothiophenes induced by chemical doping with iodine," *Journal of Chemical Physics* **109**, 10 419–29 (1998).
- [68] J. Casado, T. F. Otero, S. Hotta, V. Hernandez, F. J. Ramirez, and J. T. Lopez Navarrete, "Electrochemical doping in a series of α , α' -dimethyl end-capped oligothiophenyls: an FT-Raman confirmation of a radical cation generation," *Optical Materials* **9**, 82–7 (1998).
- [69] J. Casado, L. L. Miller, K. R. Mann, T. M. Pappenfus, V. Hernandez, and J. T. Lopez Navarrete, "Experimental and theoretical study of the infrared and Raman spectra of a substituted sexithiophene in five oxidation states," *Journal of Physical Chemistry B* **106**, 3597–605 (2002).
- [70] V. Hernandez, J. Casado, F. J. Ramirez, G. Zotti, S. Hotta, and J. T. Lopez Navarrete, "Delocalization length, electronic properties and vibrational spectra of neutral α , α' -dimethyl end-capped oligothiophenes," *Synthetic Metals* **76**, 277–80 (1996).
- [71] J. Casado, S. Hotta, V. Hernandez, and J. T. Lopez-Navarrete, "FT-IR and FT-Raman spectra of a series of oxidized α , α' -diethyl end-capped oligothiophenyls: a spectroscopic study of conjugational model defects," *Optical Materials* **12**, 321–5 (1999).
- [72] J. R. Weinberg-Wolf and L. E. McNeil, "Resonant Raman spectroscopy on

- alpha-hexathiophene single crystals,” *Physical Review B* **69**, 125 202/1–4 (2004).
- [73] M. Beasley, H. Kroemer, H. Kogelnik, D. Monroe, and S. Datta, “Report of the Investigation Committee on the Possibility of Scientific Misconduct in the Work of Hendrik Schon and Coauthors,” Tech. rep., Bell Laboratories, Lucent Technologies (2002).
 - [74] D. Knipp, R. Carius, J. Klomfass, and R. A. Street, “Study of the electronic transport of pentacene films by photoconductivity and photothermal deflection spectroscopy,” in *Organic and Polymeric Materials and Devices - Optical, Electrical and Optoelectronic Properties. Symposium*, G. E. Jabbour, S. A. Carter, J. Kido, S. T. Lee, and N. S. Sariciftci, eds., pp. 119–24 (2002).
 - [75] V. A. Lisovenko, G. A. Sandul, and M. T. Shpak, “Raman spectra background in anthracene single crystals,” *Optika i Spektroskopiya* **64**, 360–5 (1988).
 - [76] V. L. Broude, A. A. Maksimov, and I. I. Tartakovskii, “Resonance Raman scattering of light in anthracene crystals,” *Pis'ma v Zhurnal Eksperimental'noi i Teoreticheskoi Fiziki* **27**, 424–6 (1978).
 - [77] V. L. Broude, A. A. Maksimov, and I. I. Tartakovskii, “Pre-resonant Raman scattering in anthracene crystals,” *Journal of Luminescence* **21**, 183–6 (1980).
 - [78] A. A. Maksimov and I. I. Tartakovskii, “Stimulated Resonant Raman-Scattering of Light in Anthracene-Crystals,” *Physica Status Solidi B-Basic Research* **107**, 55–60 (1981).
 - [79] J. Rasanen, F. Stenman, and Penttine.E, “Raman-Scattering from Molecular-Crystals 2. Anthracene,” *Spectrochimica Acta Part A (Molecular and Biomolecular Spectroscopy)* **29a**, 395–403 (1973).
 - [80] A. Bree and R. Zwarich, “Raman scattering tensor elements for some a_g modes of anthracene,” *Journal of Raman Spectroscopy* **18**, 37–45 (1987).
 - [81] J. Brandmuller and R. Claus, “Measurements of the intensity of crystal lattice vibrations in anthracene and naphthalene,” *Spectrochimica Acta, Part A (Molecular Spectroscopy)* **25a**, 103–10 (1969).
 - [82] F. Z. Khelladi, “Davydov splitting in Raman spectra of anthracene $C_{14}H_{10}$ and $C_{14}D_{10}$ single crystals,” *Chemical Physics Letters* **34**, 490–6 (1975).

- [83] D. A. Dows, L. Hsu, S. S. Mitra, O. Brafman, M. Hayek, W. B. Daniels, and R. K. Crawford, "Pressure dependence of the lattice frequencies of anthracene and naphthalene," *Chemical Physics Letters* **22**, 595–9 (1973).
- [84] M. Nicol, M. Vernon, and J. T. Woo, "Raman spectra and defect fluorescence of anthracene and naphthalene crystals at high pressures and low temperatures," *Journal of Chemical Physics* **63**, 1992–9 (1975).
- [85] H. Shinohara, Y. Yamakita, and K. Ohno, "Raman spectra of polycyclic aromatic hydrocarbons. Comparison of calculated Raman intensity distributions with observed spectra for naphthalene, anthracene, pyrene, and perylene," *Journal of Molecular Structure* **442**, 221–34 (1998).
- [86] K. Hummer, P. Puschnig, and C. Ambrosch-Draxl, "Ab initio study of anthracene under high pressure," *Physical Review B (Condensed Matter and Materials Physics)* **67**, 184 105/1–7 (2003).
- [87] R. C. Dye and C. J. Eckhardt, "A complete set of elastic constants of crystalline anthracene by Brillouin scattering," *Journal of Chemical Physics* **90**, 2090–6 (1989).
- [88] S. Elnahwy, M. El Hamamsy, A. C. Damask, D. E. Cox, and W. B. Daniels, "Pressure dependence of the lattice parameters of anthracene up to 5.4 kbar and a re-evaluation of the elastic constants," *Journal of Chemical Physics* **68**, 1161–3 (1978).
- [89] Y. Ishihara and I. Nakada, "Energy gap of the crystalline anthracene," *Journal of the Physical Society of Japan* **28**, 667–74 (1970).
- [90] J. Sworakowski, "On the energy gap anthracene (comment on the paper of Y. Ishihara and I. Nakada)," *Journal of the Physical Society of Japan* **29**, 1390 (1970).
- [91] H. Baessler and H. Killesreiter, "Bandgap-determination from autoionization data in molecular crystals," *Molecular Crystals and Liquid Crystals* **24**, 21–31 (1973).
- [92] E. Glockner and H. C. Wolf, "The fluorescence spectrum of anthracene crystals," *Zeitschrift fur Naturforschung A (Astrophysik, Physik und Physikalische Chemie)* **24**, 943–951 (1969).
- [93] J. Aaviksoo, G. Liidja, and P. Saari, "Luminescence Spectra of Anthracene-Crystals at 0.4 K," *Physica Status Solidi B-Basic Research* **110**, 69–73 (1982).

- [94] S. Arnold and N. Hassan, "Triplet exciton lifetime under pressure in 'pure anthracene'," *Journal of Chemical Physics* **78**, 5606–11 (1983).
- [95] L. R. Painter, T. S. Riedinger, R. D. Birkhoff, and J. M. Heller, "Optical-Properties of Polycrystalline Anthracene in the 3.2-9.3 eV Spectral Region," *Journal of Applied Physics* **51**, 1747–50 (1980).
- [96] V. I. Ponomarev and G. V. Shilov, "The Crystal-Structure of Anthracene in 300-100 K Range," *Kristallografiya* **28**, 674–7 (1983).
- [97] P. Schlotter, J. Kalinowski, and H. Bassler, "Photoionization of triplet excitons in tetracene crystals," *Physica Status Solidi B* **81**, 521–6 (1977).
- [98] P. Petelenz and M. Slawik, "Band structure of charge transfer excitons in crystalline tetracene," *Chemical Physics Letters* **178**, 337–40 (1991).
- [99] M. V. Kurik and Y. P. Piryatinskii, "Luminescence of tetracene crystals," *Journal of Luminescence* **31-32**, 619–21 (1984).
- [100] G. Vaubel and H. Baessler, "Temperature dependence of width and position of the lowest singlet- singlet transition in crystalline tetracene," *Molecular Crystals and Liquid Crystals* **12**, 39–45 (1970).
- [101] K. Mizuno, A. Matsui, and G. J. Sloan, "Intermediate exciton-phonon coupling in tetracene," *Journal of the Physical Society of Japan* **53**, 2799–806 (1984).
- [102] K. Mizuno, A. Matsui, and G. J. Sloan, "Exciton-phonon interaction in tetracene single crystals under pressure," *Chemical Physics* **131**, 423–33 (1989).
- [103] C. Goldmann, S. Haas, C. Krellner, K. P. Pernstich, D. J. Gundlach, and B. Batlogg, "Hole mobility in organic single crystals measured by a "flip-crystal" field-effect technique," *Journal of Applied Physics* **96**, 2080–6 (2004).
- [104] A. M. Griffiths and P. A. Freedman, "Out-of-plane vibrations of isolated tetracene and pentacene molecules," *Journal of the Chemical Society Faraday Transactions II* **78**, 391–8 (1982).
- [105] G. Filippini and C. M. Gramaccioli, "Lattice-dynamical calculations for tetracene and pentacene," *Chemical Physics Letters* **104**, 50–3 (1984).
- [106] W. F. Maddams and I. A. M. Royaud, "The characterization of polycyclic aromatic hydrocarbons by Raman spectroscopy," *Spectrochimica Acta, Part A: Molecular and Biomolecular Spectroscopy* **46A**, 309–14 (1990).

- [107] Y. Tomkiewicz, R. P. Groff, and P. Avakian, “Spectroscopic Approach to Energetics of Exciton Fission and Fusion in Tetracene Crystals,” *Journal of Chemical Physics* **54**, 4504–7 (1971).
- [108] R. Jankowiak, J. Kalinowski, M. Konys, and J. Buchert, “Solid-state transitions in crystalline tetracene,” *Chemical Physics Letters* **65**, 549–53 (1979).
- [109] M. Rumi, G. Zerbi, K. Mullen, G. Muller, and M. Rehahn, “Nonlinear optical and vibrational properties of conjugated polyaromatic molecules,” *Journal of Chemical Physics* **106**, 24–34 (1997).
- [110] E. Venuti, R. G. Della Valle, L. Farina, A. Brillante, M. Masino, and A. Girlando, “Phonons and structures of tetracene polymorphs at low temperature and high pressure,” *Physical Review B (Condensed Matter and Materials Physics)* **70**, 104 106/1–8 (2004).
- [111] K. Kim, Y. K. Yoon, M. O. Mun, S. P. Park, S. S. Kim, S. Im, and J. H. Kim, “Optical properties of solid pentacene,” *Journal of Superconductivity* **15**, 595–8 (2002).
- [112] S. P. Park, S. S. Kim, J. H. Kim, C. N. Whang, and S. Im, “Optical and luminescence characteristics of thermally evaporated pentacene films on Si,” *Applied Physics Letters* **80**, 2872–4 (2002).
- [113] C. C. Mattheus, A. B. Dros, J. Baas, A. Meetsma, J. L. de Boer, and T. T. M. Palstra, “Polymorphism in pentacene,” *Acta Crystallographica, Section C (Crystal Structure Communications)* **C57**, 939–41 (2001).
- [114] V. Y. Budko, X. Chi, D. V. Lang, and A. P. Ramirez, “Field-effect transistors on pentacene single crystals,” *Applied Physics Letters* **83**, 4773–6 (2004).
- [115] K. O. Lee and T. T. Gan, “Space-charge-limited currents in evaporated films of pentacene,” *Physica Status Solidi A* **43**, 565–71 (1977).
- [116] C. Pannemann, T. Diekmann, and U. Hilleringmann, “Degradation of organic field-effect transistors made of pentacene,” *Journal of Materials Research* **19**, 1999–2002 (2004).
- [117] V. D. Zhukov, M. V. Kurik, Y. P. Piryatinskii, and L. I. Tsikora, “Peculiarities of the exciton reflection spectra of pentacene single crystals at low temperatures,” *Fizika Tverdogo Tela* **26**, 601–3 (1984).
- [118] T. Aoki-Matsumoto, K. Furuta, T. Yamada, H. Moriya, and K. Mizuno, “Excitonic photoluminescence in pentacene single crystal,” *International Journal of Modern Physics B* **15**, 3753–6 (2001).

- [119] A. Brillante, R. G. Della Valle, L. Farina, A. Girlando, M. Masino, and E. Venuti, “Raman phonon spectra of pentacene polymorphs,” *Chemical Physics Letters* **357**, 32–6 (2002).
- [120] R. He, I. Dujovne, L. Chen, Q. Miao, C. F. Hirjibehedin, A. Pinczuk, C. Nuckolls, C. Kloc, and A. Ron, “Resonant Raman scattering in nanoscale pentacene films,” *Applied Physics Letters* **84**, 987–9 (2004).
- [121] F. Li, J. Lin, J. Feng, G. Cheng, H. Liu, S. Liu, L. Zhang, X. Zhang, and S. T. Lee, “Electrical and optical characteristics of red organic light-emitting diodes doped with two guest dyes,” *Synthetic Metals* **139**, 341–6 (2003).
- [122] X. Wang, Y. Sakuratani, H. Sone, K. Tanaka, S. Miyata, and H. Usui, “A diaminomaleonitrile derivative as a new dopant for red-light-emitting electroluminescent device,” *Journal of Physics D (Applied Physics)* **36**, 1789–93 (2003).
- [123] D. E. Henn, W. G. Williams, and D. J. Gibbons, “Crystallographic data for an orthorhombic form of rubrene,” *Journal of Applied Crystallography* **4**, 256 (1971).
- [124] A. I. Lesin, A. I. Pristupa, and E. L. Frankevich, “Magnetic-resonance spectrum of triplet exciton pairs in polycrystalline layers of rubrene with nonequivalent locations of the molecules in the unit cells, as detected from the fluorescence yield,” *Optika i Spektroskopiya* **51**, 861–5 (1981).
- [125] M. Saleh, “Transit time measurements of photogenerated charge carriers in orthorhombic rubrene crystals,” *Physica Scripta* **21**, 220–2 (1980).
- [126] M. Uchida, C. Adachi, T. Koyama, and Y. Taniguchi, “Charge carrier trapping effect by luminescent dopant molecules in single-layer organic light emitting diodes,” *Journal of Applied Physics* **86**, 1680–7 (1999).
- [127] G. Sakamoto, C. Adachi, T. Koyama, Y. Taniguchi, C. D. Merritt, H. Murata, and Z. H. Kafafi, “Significant improvement of device durability in organic light-emitting diodes by doping both hole transport and emitter layers with rubrene molecules,” *Applied Physics Letters* **75**, 766–8 (1999).
- [128] H. Aziz and Z. D. Popovic, “Study of organic light emitting devices with a 5,6,11,12-tetraphenyl naphthacene (rubrene)-doped hole transport layer,” *Applied Physics Letters* **80**, 2180–2 (2002).
- [129] Z. Zhilin, J. Xueyin, and X. Shaohong, “Energy transfer and white emitting organic thin film electroluminescence,” *Thin Solid Films* **363**, 61–3 (2000).

- [130] Y. Hamada, H. Kanno, T. Sano, H. Fujii, Y. Nishio, H. Takahashi, T. Usuki, and K. Shibata, "Organic light-emitting diodes using a gallium complex," *Applied Physics Letters* **72**, 1939–41 (1998).
- [131] E. Botzung-Appert, V. Monnier, T. H. Duong, R. Pansu, and A. Ibanez, "Polyaromatic Luminescent Nanocrystals for Chemical and Biological Sensors," *Chemistry of Materials* **16**, 1609–11 (2004).
- [132] Y. Hamada, H. Kanno, T. Tsujioka, T. Hisakazu, and T. Usuki, "Red organic light-emitting diodes using an emitting assist dopant," *Applied Physics Letters* **75**, 1682–4 (1999).
- [133] V. Podzorov, S. E. Sysoev, E. Loginova, V. M. Pudalov, and M. E. Gershenson, "Single-crystal organic field effect transistors with the hole mobility approximately $8 \text{ cm}^2/\text{V s}$," *Applied Physics Letters* **83**, 3504–6 (2003).
- [134] V. Podzorov, E. Menard, A. Borissov, V. Kiryukhin, J. A. Rogers, and M. E. Gershenson, "Intrinsic charge transport on the surface of organic semiconductors," *Physical Review Letters* **93**, 086 602/1–4 (2004).
- [135] W. G. Williams, "Hole mobility in rubrene," *Discussions of the Faraday Society* **51**, 61–6 (1971).
- [136] K. Ohno, H. Mutoh, and Y. Harada, "Application of Penning ionisation electron spectroscopy to the study of chemical reactions on the solid surface; photooxidation of naphthalene and rubrene," *Surface Science* **115**, L128–32 (1982).
- [137] V. Ramamurthy and K. Venkatesan, "Photochemical-Reactions of Organic-Crystals," *Chemical Reviews* **87**, 433–81 (1987).
- [138] M. Kaschke, N. P. Ernsting, and F. P. Schafer, "Rubrene, a saturable absorber for 308 nm," *Optics Communications* **66**, 211–15 (1988).
- [139] W. Xie, Y. Zhao, J. Hou, and S. Liu, "Spectroscopic ellipsometry studies of CuPc and other materials for organic light-emitting devices," *Japanese Journal of Applied Physics, Part 1 (Regular Papers, Short Notes & Review Papers)* **42**, 1466–9 (2003).
- [140] K. H. Choi, D. H. Hwang, H. M. Lee, L. M. Do, and T. Zyung, "Electroluminescent behaviours of polymer/organic heterostructure devices," *Synthetic Metals* **96**, 123–6 (1998).
- [141] Z. Zhi-Lin, J. Xue-Yin, X. Shao-Hong, T. Nagatomo, and O. Omoto, "The effect of rubrene as a dopant on the efficiency and stability of organic thin

- film electroluminescent devices,” *Journal of Physics D (Applied Physics)* **31**, 32–5 (1998).
- [142] H. Najafov, I. Biaggio, V. Podzorov, M. F. Calhoun, and M. E. Gershenson, “Primary Photoexcitations and the Origin of the Photocurrent in Rubrene Single Crystals,” *Physical Review Letters* **96**, 056 604/1–4 (2006).
 - [143] T. L. Gustafson and F. E. Lytle, “Time-resolved rejection of fluorescence from Raman spectra via high repetition rate gated photon counting,” *Analytical Chemistry* **54**, 634–7 (1982).
 - [144] J. M. Harris, R. W. Chrisman, F. E. Lytle, and R. S. Tobias, “Sub-nanosecond time-resolved rejection of fluorescence from Raman spectra,” *Analytical Chemistry* **48**, 1937–43 (1976).
 - [145] S. F. Parker, K. P. J. Williams, P. J. Hendra, and A. J. Turner, “Fourier transform Raman spectroscopy using a bench-top FT-IR spectrometer,” *Applied Spectroscopy* **42**, 796–800 (1988).
 - [146] C. Kloc, P. G. Simpkins, T. Siegrist, and R. A. Laudise, “Physical vapor growth of centimeter-sized crystals of α -hexathiophene,” *Journal of Crystal Growth* **182**, 416–27 (1997).
 - [147] R. A. Laudise, C. Kloc, P. G. Simpkins, and T. Siegrist, “Physical vapor growth of organic semiconductors,” *Journal of Crystal Growth* **187**, 449–54 (1998).
 - [148] R. Zeis, C. Besnard, T. Siegrist, C. Schlockermann, X. Chi, and C. Kloc, “Field-effect studies on rubrene and impurities of rubrene,” *Chemistry of Materials* **18**, 244–8 (2006).
 - [149] P. Y. Yu and M. Cardona, *Fundamentals of Semiconductors: Physics and Materials Properties* (Springer, New York, 2003), third edn.
 - [150] “CERIUS²,” (1997).
 - [151] I. Bulgarovskaya, V. Vozzhennikov, S. Aleksandrov, and V. Belsky, “QQQ-CIG01,” *Zinat. Akad. Vestis, Khim. Ser* **missing**, 53 (1983), data as cited in the Cambridge Structural Database run by the Cambridge Crystallographic Data Centre.
 - [152] D. Holmes, S. Kumaraswamy, A. Matzger, and K. Vollhardt, “TET-CEN01,” *European Journal of Organic Chemistry* **5**, 3399 (1999), data as cited in the Cambridge Structural Database run by the Cambridge Crystallographic Data Centre.

- [153] P. Sinha, S. E. Boesch, C. M. Gu, R. A. Wheeler, and A. K. Wilson, “Harmonic vibrational frequencies: Scaling factors for HF, B3LYP, and MP2 methods in combination with correlation consistent basis sets,” *Journal of Physical Chemistry A* **108**, 9213–7 (2004).
- [154] L. Brandus, “Calculation of Raman scattering cross sections in benzene,” *Revue Roumaine de Physique* **23**, 463–7 (1978).
- [155] E. B. Wilson, “The normal modes and frequencies of vibration of the regular plane hexagon model of the benzene molecule,” *Physical Review* **45**, 706–14 (1934).
- [156] E. B. Wilson, J. Decius, and P. Cross, *Molecular Vibrations: The Theory of Infrared and Raman Vibrational Spectra* (Dover Publications, Inc., New York, NY, 1955).
- [157] Personal communication with Bertram Batlogg, March 2006.